

Thermally-Activated Delayed Fluorescence in a Spiro-Acridine Derivative : Application for Efficient Organic Light-Emitting Diodes

メーヘシュ, ガーボル

<https://doi.org/10.15017/1470576>

出版情報 : 九州大学, 2014, 博士 (工学), 課程博士
バージョン :
権利関係 : 全文ファイル公表済

2014

Doctoral Thesis

**Thermally-Activated Delayed Fluorescence in a
Spiro-Acridine Derivative: Application for
Efficient Organic Light-Emitting Diodes**

Gábor Méhes

Department of Chemistry and Biochemistry

Graduate School of Engineering

Kyushu University

Table of Contents

Table of Contents	1
Chapter 1: General Introduction	5
1.1 A Brief Introduction to Organic Light-Emitting Diodes	6
1.1.1 Potential and Main Applications.....	6
1.1.2 Short Overview of Operation and Structure.....	7
1.1.3 Radiative Exciton Generation Efficiency.....	9
1.1.4 Early Development of Fluorescent OLEDs.....	10
1.1.5 Harvesting Triplet Excitons in Phosphorescent OLEDs via the Heavy Metal Effect.....	12
1.2 Exciton Harvesting via Thermally-Activated Delayed Fluorescence.....	14
1.2.1 Reverse Intersystem Crossing and Singlet-Triplet Energy Gap.....	14
1.2.2 RISC with Low Efficiencies in Early TADF Emitters.....	15
1.2.3 Charge Transfer to Achieve Small Singlet-Triplet Energy Gap in Metal-Free Emitters.....	17
1.2.4 Spiro-Junction to Enhance the Spatial Separation between a Donor and Acceptor.....	19
1.3 How to Utilize a Large Singlet-Triplet Energy Gap in TADF Emitters.....	20
1.3.1 Long Triplet Lifetime and its Quenching by Dioxygen.....	20
1.3.2 The Various Physical Methods to Obtain Long Triplet Lifetime in Molecular Oxygen Sensors.....	22

1.4 The Role of Host Matrices in TADF Emitters.....	23
1.5 Goals and Motivation - Outline of the Experimental Part.....	24
1.6 References.....	25
Chapter 2: Materials and Methods.....	30
2.1 Synthesis of 10-phenyl-10H-spiro[acridine-9,9'-fluorene]-2',7'-dicyanitrile (ACRF).....	31
2.1.1 Synthesis of 2',7'-dibromo-10-phenyl-10H-spiro[acridine-9,9'-fluorene] (2).....	31
2.1.2 Synthesis of 10-phenyl-10H-spiro[acridine-9,9'-fluorene]-2',7'-dicyanitrile (ACRF) using Row IIa.....	32
2.1.3 Synthesis of 10-phenyl-4a,9a-dihydro-10H-spiro[acridine-9,9'-fluorene]-2',7'- dicyanaldehyde (3).....	32
2.1.4 Synthesis of 10-phenyl-10H-spiro[acridine-9,9'-fluorene]-2',7'-dicyanitrile (ACRF) using Row IIb.....	33
2.2 Organic Compounds used in OLED Fabrication.....	33
2.3 Photoluminescence Study.....	34
2.4 Electroluminescence Study.....	36
2.5 Calculations based on Density Functional Theory (DFT).....	36
2.6 Preparation Method of 2wt% ACRF:PS Films and Determination of Oxygen Quenching Ratio.....	37
2.7 Reference.....	37
Chapter 3: Enhanced Electroluminescence Efficiency in a Spiro-Acridine Derivative through Thermally-Activated Delayed Fluorescence.....	38

3.1 Introduction to ACRF.....	39
3.2 Photoluminescent Properties.....	40
3.3 Electroluminescent Performance.....	46
3.4 Conclusions.....	48
3.5 References.....	49

Chapter 4: Influence of Host Matrix on Thermally-Activated Delayed Fluorescence: Effects on Emission Lifetime, Photoluminescence Quantum Yield, and Device Performance.....

Performance.....	51
4.1 Introduction.....	52
4.2 Results and Discussion.....	53
4.2.1 Photoluminescence Lifetime of ACRF:Host Layers.....	53
4.2.2 Photoluminescence Quantum Yield and Quenching by Host Matrix.....	61
4.2.3 Mechanism for Host Dependence of Delayed Fluorescence Lifetime	66
4.2.3.1 Dynamic Change in ΔE_{ST} during Emission Decay.....	66
4.2.3.2 Mechanism of the Dynamic Change in ΔE_{ST}	75
4.2.4 Electroluminescence Characteristics of ACRF:Host Layers.....	79
4.3 Conclusions.....	82
4.4 References.....	83

Chapter 5: Sensing of Dioxygen based on Thermally-Activated Delayed Fluorescence.....

Fluorescence.....	86
5.1 Mechanism of Oxygen Quenching in ACRF.....	87

5.2 Oxygen Quenching in ACRF Doped into Polystyrene	88
5.3 Conclusions.....	90
5.4 References.....	91
Chapter 6: Summary and Conclusions.....	92
Appendix.....	97
A. Methods.....	97
B. Supplementary Data - Elemental Analysis	98
C. Supplementary Figures.....	99
Acknowledgments.....	102
List of Publications related to this Thesis.....	104

Chapter 1

General Introduction

1.1 A Brief Introduction to Organic Light-Emitting Diodes

1.1.1 Potential and Main Applications

Organic light-emitting diodes (OLEDs) are solid-state light-emitting devices that are driven by electrical current and use a thin layer of carbon-based aromatic molecules as the active material. The thickness of the organic layer is typically ~100 nm. Due to the amorphous nature of organic molecules, the emitting layer can be deposited on a wide variety of substrates, including bendable plastic films, with fast and mass-scale fabrication processes such as inkjet printing or dip coating, unlike the substrate-sensitive inorganic crystalline emitters used in inorganic LEDs. The most promising applications for OLEDs so far have been displays and illumination.

The first OLED television was commercialized in 2008 by Sony Corporation (Fig. 1.1a), and small-size displays for mobile phones by Samsung and LG Display have been penetrating the market for several years [1]. In addition, large-size OLED displays from LG Display, price-competitive with high performance LCD displays, are starting to emerge on the market. Therefore, OLED displays are predicted to take a significant market share of the display business after an expected reduction in material and fabrication costs, thanks to the superior color richness, unlimited viewing angle, thin and lightweight form factors, and mechanical flexibility of OLEDs.

For illumination, OLEDs offer wide-area, thin light sources producing diffuse light with wide possibilities for deployment on various surfaces in various shapes. For example, OLEDs integrated together with organic solar cells (OSCs) in windows could be transparent during the daytime while harvesting energy from the sun and emit light at night, as demonstrated by a joint project of BASF and Philips in the automotive field [2]. Moreover, integrating OLED panels with sensors and cameras can give rise to intelligent lighting solutions, such as mimicking the shape and the movement of a human body standing in front of a matrix-array of OLED panels, shown in Fig. 1.1b.

One of the biggest challenges for OLEDs in both display and lighting applications has been to achieve red, green, and blue emitters with high efficiency and long device lifetime that allow the creation of durable white light-emitting OLEDs (WOLEDs) [3-5]. However, luminous efficiencies of recent WOLEDs, based on emitters containing precious

metals, of 90-100 lm/W at 1000 cd/m² are starting to overtake those of fluorescent tubes [6], and there is still much room for future improvement to reach the theoretical maximum efficacy of 249 lm/W [7].

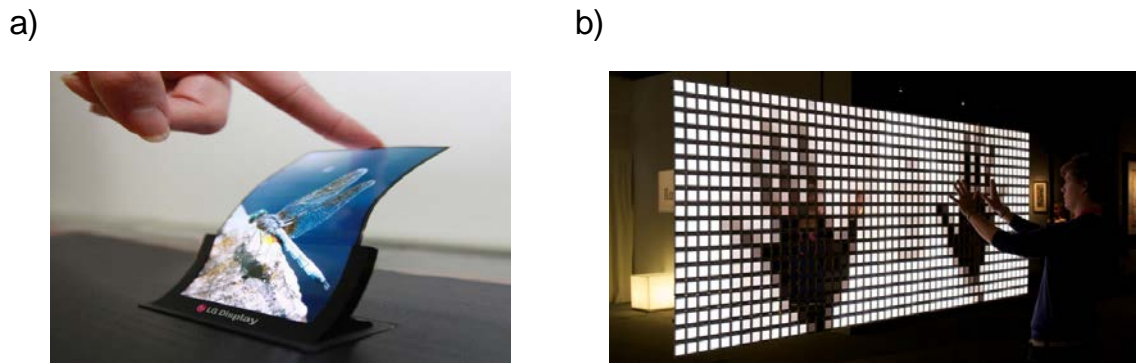


Figure 1.1 a) Prototype of a flexible OLED display by LG [1]; b) Interactive OLED mirror made by integrating Lumiblade OLED panels from Philips with a digital camera.

1.1.2 Short Overview of Operation and Structure

In a typical OLED, a thin organic layer is sandwiched between a cathode and a transparent anode. The basic operation principle of a single-layer OLED is represented in Fig. 1.2. By applying a voltage bias, electrons and holes are injected from the cathode and anode, respectively, into the organic layer (1), where they transport towards each other (2), and generate excitons (3) according to the following formula:



where M^+ and M^- represent molecules carrying a hole or an electron, respectively, and M_0 and M^* are the light-emitting molecules in ground and excited states, respectively. When a hole and an electron recombine, they form an exciton, generating light (4), called electroluminescence (EL).

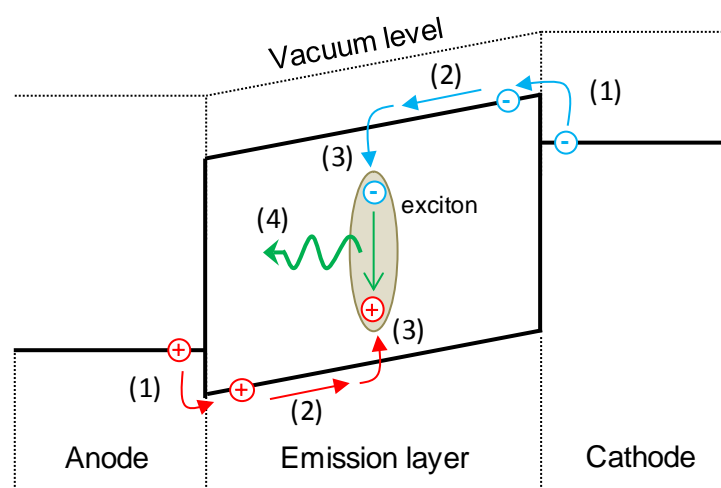


Figure 1.2 Schematic energy diagram of a single-layer OLED illustrating the basic processes of electroluminescence. The diagram is based on Brütting *et al.*, Ref. 8.

The transport of holes and electrons in an organic layer usually cannot be done efficiently using only one kind of organic materials. Therefore, at least two layers are required: a hole transport layer (HTL) and an electron transport layer (ETL) as shown in Fig. 1.3a. The recombination zone is then located at the interface of these two layers. To improve the EL efficiency of OLEDs, three-layer and multilayer device structures have been introduced (Fig. 1.3b and 1.3c, respectively). The three-layer structure introduces an emission layer (EML) between a HTL and an ETL that allows for a wider recombination zone and tuning of various parameters, such as emission color, device stability, *etc* [9-11].

In OLEDs, keeping the operational voltage as low as possible both to save energy and to achieve a longer device lifetime is desirable. The operational voltage strongly depends on the matching between the highest occupied molecular orbitals (HOMO) and lowest unoccupied molecular orbitals (LUMO) of adjacent layers and the thickness of the OLED stack. The HOMO and LUMO levels represent energy levels where the holes and electrons transport in organic molecules, respectively, and are usually the highest π orbital fully occupied by electrons and the lowest unoccupied π^* orbital, respectively. Differences in the HOMO and LUMO levels of the usual HTLs, EMLs, and ETLs lead to voltage drops at the interfaces of these layers. A similar effect at the HTL/anode and ETL/cathode interfaces also leads to a higher applied electric field needed to operate OLEDs. To

circumvent this disadvantage, additional layers that allow for more efficient transport of holes and electrons have been introduced: hole injection layer (HIL), electron injection layer (EIL), hole blocking layer (HBL), and electron blocking layer (EBL) (Fig. 1.3c). Other important requirements for ETLs and HTLs, besides good thermal and operational stabilities, are high electron and hole mobilities, respectively.

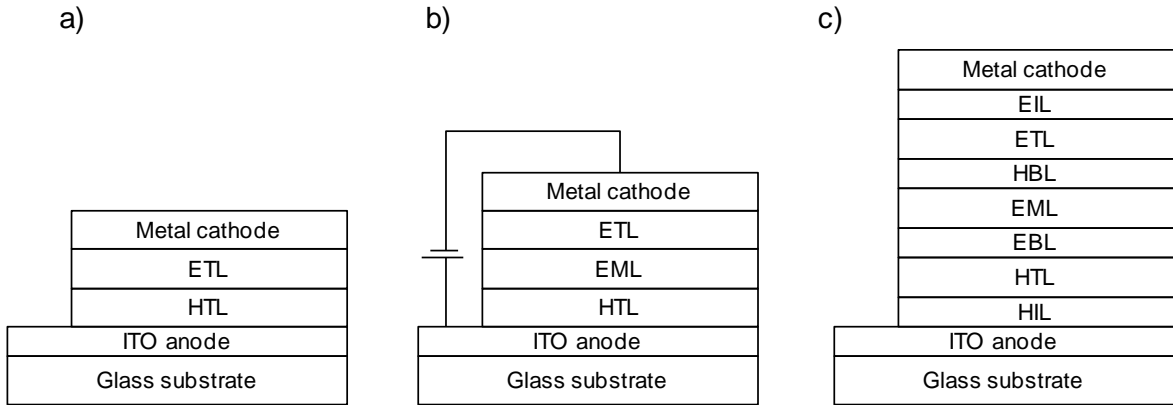


Figure 1.3 Schematic views of typical multilayer OLED structures: a) two-layer, b) three-layer, and c) multilayer, based on Ref. 12.

1.1.3 Radiative Exciton Generation Efficiency

One of the most important measurements of OLED performance is the external EL quantum efficiency (η_{ext}), which is the ratio of the number of injected charge carriers to the number of photons emitted out from the device. The theoretical maximum external quantum efficiency ($\eta_{\text{ext(t)}}$) can be estimated from the photoluminescence (PL) characteristics as follows:

$$\eta_{\text{ext(t)}} = \eta_{\text{int}} \times \eta_{\text{p}} = \Phi_{\text{PL}} \times \eta_{\text{r}} \times \gamma \times \eta_{\text{p}}, \quad (\text{Eq. 1.2})$$

where η_{int} is the internal EL efficiency, η_{p} is the photon outcoupling efficiency, Φ_{PL} is the PL quantum efficiency, η_{r} is the radiative exciton generation efficiency, and γ is the charge balance factor. Among these parameters, Φ_{PL} reaches unity if emitters lacking non-radiative deactivation paths are utilized, while γ can be maximized by using the proper HTL, ETL and other assisting layers in OLEDs that help to achieve a balanced carrier flow

to the emitter. In typical bottom-emitting OLEDs built on flat glass substrates, only $\sim 1/5$ of the generated light can escape to the air through the ITO anode and the glass substrate; thus, η_p has a value of 20% in most cases. Although various outcoupling techniques have been used to improve η_p [8,13-15], these solutions mostly add to the complexity and cost of device fabrication.

Of particular interest to this thesis is the radiative exciton generation efficiency, which is a sum of the radiative singlet-exciton $\eta_r(S_1)$ and the radiative triplet-exciton generation efficiencies $\eta_r(T_1)$; $\eta_r = \eta_r(S_1) + \eta_r(T_1)$. Here, S_1 and T_1 refer to the lowest excited states having singlet and triplet spin multiplicity, respectively. The formation ratio of electrically generated S_1 and T_1 states is 1:3 in small-molecule emitters. This ratio is based on an inherent spin-statistical effect [16]. Since the triplet excited state is usually non-emissive in fluorescent emitters, the first generation of OLEDs that employ these emitters have a maximum η_r of only 25%. The low η_r , in turn, also limits η_{int} to 25%, resulting in devices with $\eta_{ext(t)}$ of 5% when no additional techniques for the improvement of η_p are used. Although $\eta_r(S_1)$ is estimated $\sim 25\%$ in small molecular emitters that we focus on, we also note that $\eta_r(S_1)$ was found to be higher than 25% in polymeric and macromolecular emitters [17,18].

1.1.4 Early Development of Fluorescent OLEDs

The spin-statistical limitation of η_r is a direct result of the injection of charges into organic devices. The origin of injection of electrical current into solid-state organic materials dates back to 1960s when Pope *et al.* and Helfrich *et al.* have demonstrated EL from highly purified anthracene crystal platelets [19,20]. These devices were markedly different from today's OLED structures since the thickness of the crystals were on the micrometer and millimeter order, resulting in driving voltages in the range of 50-2000 V to achieve EL. Although η_{ext} of $\sim 1-5\%$ have been already demonstrated at these historical times of the OLED evolution [21], the necessity for using high operating voltages rendered the first OLED devices unusable for practical applications.

Thus, in the early development of OLEDs, rather than improving the exciton generation efficiency, more fundamental challenges to achieve injection of high current at

much lower driving voltages had to be solved. A significant improvement in current injection was achieved in 1982 by Partridge [22-25], who used 500-nm-thick poly(vinylcarbazole) (PVCz) films as emissive layers with the efficient hole-and electron injecting $\text{SbCl}_5/\text{PVCz}$ anode and cesium cathode, respectively. Partridge demonstrated blue EL and succeeded in injecting 1 A/cm^2 in his device. Further, in 1986, Hayashi *et al.* introduced a new method to reduce the operating voltage by inserting a polythiophene-electropolymerized thin film between an indium-tin-oxide (ITO) anode, and a perylene-deposited film [26].

Although Hayashi *et al.* demonstrated the first double-layer organic EL device, it was the double-layer OLED of Tang and Van Slyke [27] that served as a major driver and inspiration to the research community for putting extensive efforts into developing efficient OLEDs. In Tang's paper, published in 1987, a vacuum-deposited 1,1-bis(4-di-p-tolylaminophenyl)-cyclohexane (TPAC) HTL and tris(8-hydroxyquinolino)aluminum (Alq_3) ETL were sandwiched between an ITO anode and a MgAg electrode. Here, the new metal alloy provided excellent electron injection, while Alq_3 , shown in Fig. 1.4a, served as a combined ETL and EML. Thanks to the extensive efforts of the OLED community triggered by Tang's pioneering work [27], fluorescence-based OLEDs containing dopant materials emitting in the wide variety of spectra including red, green and blue regions (Fig. 1.4b-d) were achieved throughout the 1990s. However, η_{ext} was still limited to 5% for OLEDs without outcoupling techniques because $\eta_i(\text{T}_1) = 0$ in fluorescence-based OLEDs.

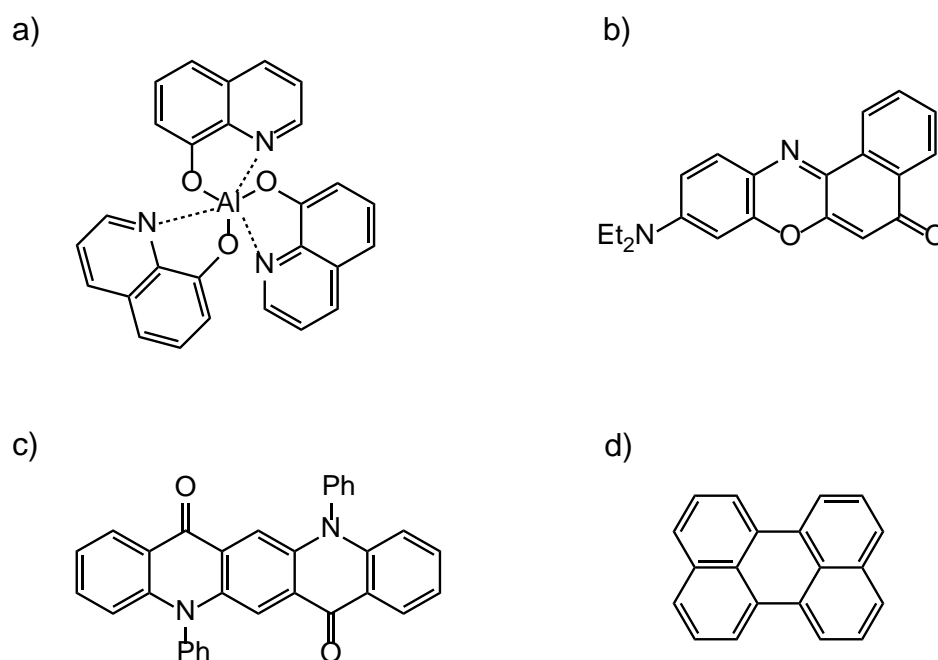


Figure 1.4 a) Molecular structures of Alq₃, and of typical fluorescent dopants b) Nile red - red, c) DPQA - green, and d) Perylene - blue.

1.1.5 Harvesting Triplet Excitons in Phosphorescent OLEDs via the Heavy Metal Effect

A breakthrough in harvesting the triplet excitons in OLEDs was finally made by Baldo *et al.* in 1998 [28]. In their device, doping the phosphorescent dye 2,3,7,8,12,13,17,18-octaethyl-21H,23H-porphine platinum(II) (PtOEP) into Alq₃ host resulted in a light emission from both the singlet and triplet excited states at room temperature. The introduction of the heavy atom Pt lead to an effective spin-orbit coupling for the excitons that mixed the singlet and triplet states. This, in turn, induced a non-radiative intersystem crossing (ISC) from the S₁ to the T₁ states with a subsequent radiative ISC from the T₁ to the S₀ states, called phosphorescence.

Intersystem crossing is a spin-forbidden process from quantum-mechanical point of view, thus it needs the presence of an additional allowing factor, such as spin-orbit or hyperfine coupling. Spin-orbit coupling, which is essential for harvesting the 75% out of all created excitons in an OLED, can be understood by visualizing a crossing point on the

mixed S_1 and T_1 potential curves, as shown in Fig. 1.5. Through this crossing point, the movement of excitons is allowed towards the energy minimum on the T_1 curve.

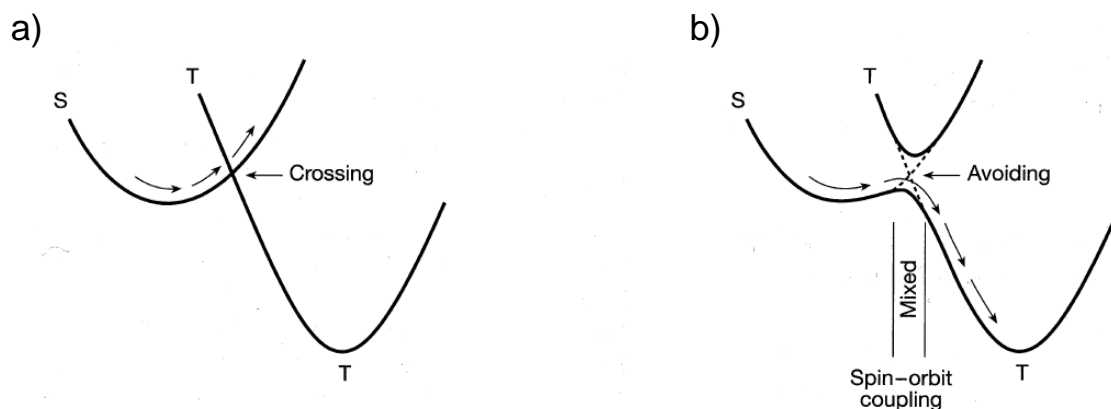


Figure 1.5 Schematic interpretation of a reaction coordinate crossing in terms of energy surfaces with a) no ISC and b) ISC allowed via spin-orbit coupling. Modified from Turro, Ref 29.

Following Baldo *et al.*'s report, the era of highly-efficient phosphorescence-based OLEDs started. Among various heavy metals, including Os, Ru, Pt, Pd, and Eu, iridium (Ir) has been proven to induce the most efficient spin-orbit coupling that allowed for 100% of η_r . In addition, the combined effect of highly phosphorescent Ir-containing aromatic emitters with Φ_{PL} close to 100% and perfect charge balance resulted in an ultimate $\eta_{ext} = 20\%$ in OLEDs [30]. A decade after Baldo *et al.*'s initial contribution, the OLED technology has been gradually penetrating the display and lighting markets. Examples of widely used red, green, and blue phosphorescent dopants necessary for full-color displays are shown in Fig. 1.6.

Despite of the high quantum efficiency of organometallic emitters, their structure incorporates precious metals that are present in the Earth's crust in limited amounts, leading to higher prices. This disadvantage also results in a limitation in molecular design and makes the large-scale production of OLEDs based on organometallic phosphorescent emitters less sustainable.

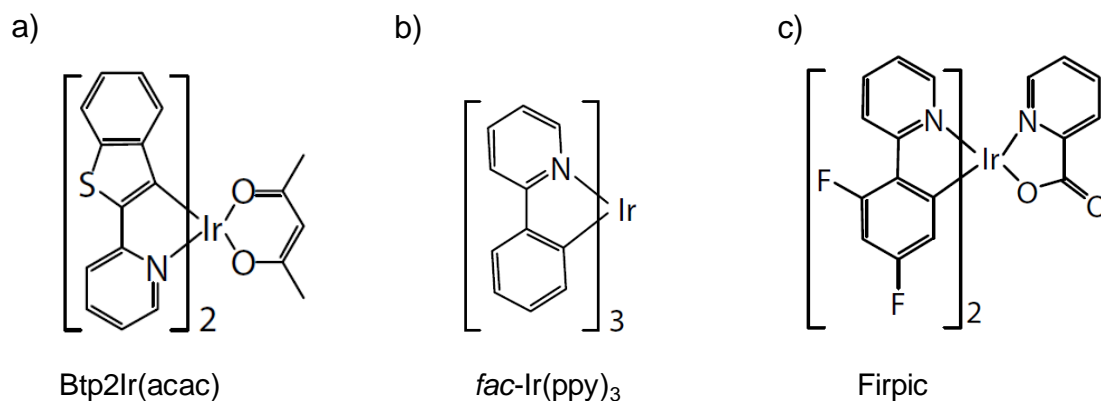


Figure 1.6 Typical phosphorescent dopants as OLED emitters: a) red, b) green, and c) blue.

1.2 Exciton Harvesting via Thermally-Activated Delayed Fluorescence

1.2.1 Reverse Intersystem Crossing and Singlet-Triplet Energy Gap

An alternative way of harvesting the 75% of triplet excitons in fluorescent emitters under electrical injection is called thermally-activated delayed fluorescence (TADF; or E-type delayed fluorescence), illustrated in Fig. 1.7a. In TADF emitters, part of the excited singlet excitons first decays via a prompt fluorescence, while simultaneously another part of the singlet excitons undergoes an $S_1 \rightarrow T_1$ ISC process. After the ISC or from excitons generated directly in the T_1 state, $T_1 \rightarrow S_1$ endothermic reverse intersystem crossing (RISC) takes place, leading to a delayed TADF emission. The mechanism of RISC-upconversion is driven by thermal vibronic energy. Although RISC can also occur as a result of other mechanisms, such as triplet-triplet annihilation (TTA), producing p-type delayed fluorescence [31], or from a higher triplet T_n state to the S_1 state in certain molecules and under certain circumstances [32,33], these processes are limited in efficiency [34, 32] and do not require thermal energy for the reverse ISC process. Hence, our focus will be solely on endothermic RISC, which we refer to as 'RISC' throughout this thesis.

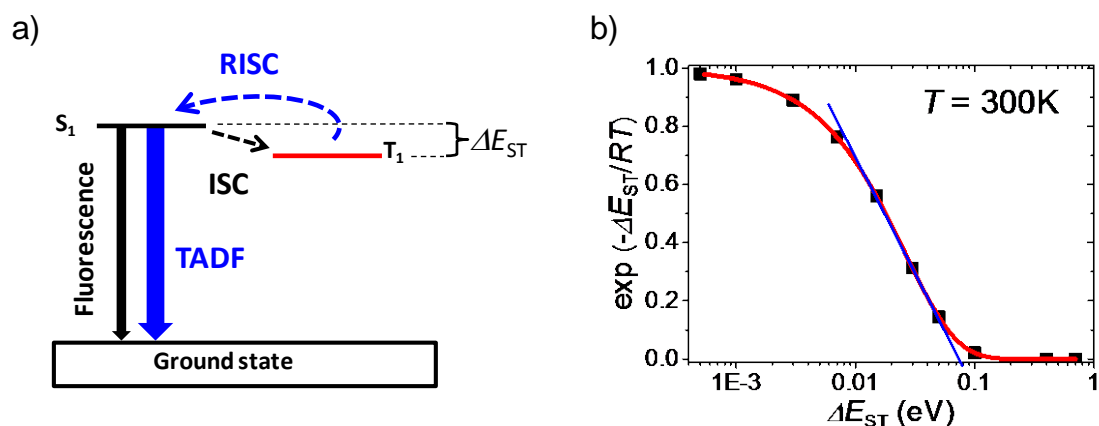


Figure 1.7 a) Energy diagram explaining the mechanism of TADF. b) Results of calculation based on Eq. 1.3 at $T = 300$ K.

The main criteria for TADF emission are a small energy difference between the lowest singlet and triplet excited states (ΔE_{ST}) and high yield of triplet-to-upconverted-singlet formation [35,36]. The decay of TADF is orders of magnitude slower compared to that of fluorescence due to the long time required for thermal recycling of excitons from the T_1 to the S_1 states, typically on the order of $10^{-6} - 10^{-2}$ s. According to the Boltzmann equation, a smaller ΔE_{ST} yields a higher rate of RISC (k_{RISC}) at a given temperature T [37,38]:

$$k_{RISC} = \bar{k}_{RISC} \exp\left(-\frac{\Delta E_{ST}}{RT}\right), \quad (\text{Eq. 1.3})$$

where \bar{k}_{RISC} is the rate of temperature-independent adiabatic RISC and R is the gas constant [35]. Most organic light-emitting molecules do not possess a small enough ΔE_{ST} to allow for efficient TADF. Calculation using the Boltzmann equation at 300 K indicates that $\Delta E_{ST} < \sim 80$ meV are required for a rapid enhancement in k_{RISC} (Fig. 1.7b).

1.2.2 RISC with Low Efficiencies in Early TADF Emitters

One of the earliest attempts to explain TADF was made by J. Perrin, whose energy histogram, known as a Perrin diagram (1925, Fig. 1.8a), is based on the first observation of α -phosphorescence (E-type delayed fluorescence) in eosin (Fig. 1.8b) by his son F. Perrin

in 1924 [39,36]. The horizontal axis of a Perrin diagram represents time. Going from left to right, the diagram illustrates a transition from the ground state A_G to the stable excited state a , which is followed by a longer time spent in the metastable state α . From state α , deexcitation to A_G can only occur through an upconversion from α to a , assisted by thermal energy or collision with other molecules. J. Perrin, although describing the principle of TADF in a correct way, believed this mechanism was one of the ways phosphorescence occurs, because he assumed that an $\alpha \rightarrow A_G$ (or $T_1 \rightarrow S_0$) transition is strictly spin-forbidden.

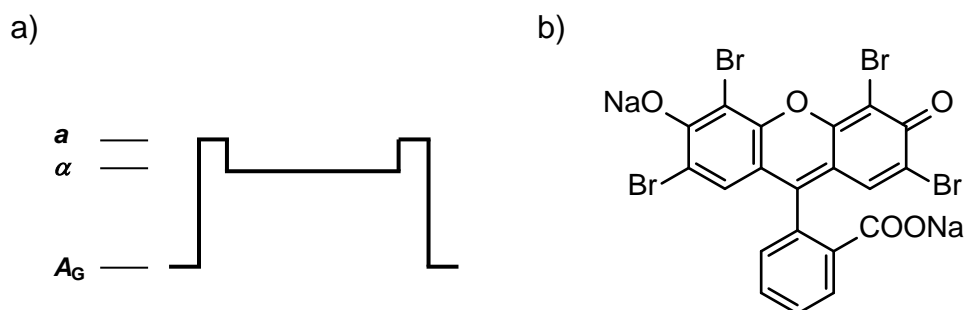


Figure 1.8 a) Perrin diagram. Modified from Ref. 39. b) Molecular structure of eosin.

TADF was observed in several fluorescent molecules besides eosin in the past, including in proflavine hydrochloride, fluorescein, acridine orange, *etc.* [40], mostly in deoxygenated solutions, and in porphyrins, metalloporphyrins and chlorophyll *c* adsorbed on a filter paper [41,42]. On the other hand, the first report about a successful TADF-emitter-based OLED was not until 2009 by Endo *et al.* [43] due to the low efficiencies observed in TADF emitters. Endo *et al.* observed a temperature-dependent enhancement in the emission of a tin(IV) fluoride–octaethylporphine ($\text{SnF}_2\text{-OEP}$) material doped into a PVCz film and found that the enhancement originated from a TADF emission. Although the PL and EL quantum efficiencies using this emitter were low, the increase in both the PL and EL intensities with temperature in the range from 300 K to 400 K showed the promise for utilizing TADF in OLEDs.

1.2.3 Charge Transfer to Achieve Small Singlet-Triplet Energy Gap in Metal-Free Emitters

The efficiency of TADF in SnF₂-OEP is limited by its rather large $\Delta E_{ST} \sim 0.24$ eV. To improve k_{RISC} , new materials with smaller ΔE_{ST} are needed. A method to achieve small ΔE_{ST} was proposed by the same author in 2011 [44] by using the effect of intramolecular charge-transfer (CT) to lower the S₁-T₁ energy gap. A small ΔE_{ST} results when the overlap between the wave functions of electrons located in the HOMO and LUMO orbitals of a luminescent molecule is small, which minimizes the electron-electron repulsion in the triplet state [43]. The small overlap between the wave functions leads to a small exchange energy K , described in the theory of quantum chemistry by the following integral:

$$K = \iint dr_1 dr_2 \psi_a^*(r_1) \psi_b(r_1) r_{12}^{-1} \psi_b^*(r_2) \psi_a(r_2), \quad (Eq. 1.4)$$

where ψ_a and ψ_b are the antibonding and bonding spatial molecular orbitals defined by the electron wave functions, respectively, and r_1 and r_2 are position vectors.

The HOMO and LUMO states can be spatially separated using CT emitters to achieve a small K , as Endo *et al.* demonstrated by quantum-chemical calculations [44]. This spatial separation can be elegantly realized by chemically bonding a donor moiety, containing an electron donating group (EDG), and an acceptor moiety, containing an electron withdrawing group (EWG), to each other. The EWG and the EDG in Endo *et al.*'s compound, 2-biphenyl-4,6-bis(12-phenylindolo[2,3-a]carbazole-11-yl)-1,3,5-triazine (PIC-TRZ, Fig. 1.9a), were a triazine, and two indolocarbazole units, respectively. This molecular CT system resulted in a $\Delta E_{ST} = 0.11$ eV [43], which is a substantial improvement compared to $\Delta E_{ST} \sim 0.24$ eV of SnF₂-OEP. Therefore, thanks to the TADF emission in PIC-TRZ, EL with $\eta_{ext} = 5.3\%$ was achieved, which was significantly higher than the maximum theoretical limit in this molecule estimated based on a Φ_{PL} of 39% without harvesting the triplet excitons through RISC ($\eta_{ext(t)} = 2\%$ without TADF).

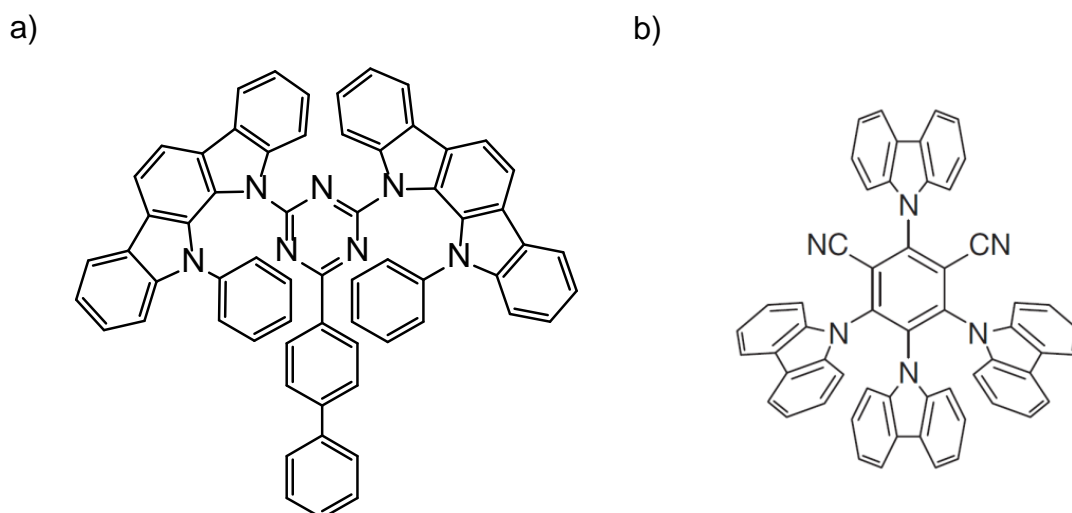


Figure 1.9 Molecular structure of TADF emitters a) PIC-TRZ and b) 4CzIPN.

Since the above donor-acceptor CT principle is a very effective way to design molecules, several new metal-free TADF compounds have been presented recently as efficient emitter materials in OLEDs based on this principle [45-51]. Some of these promising emitters, such as 1,2,3,5-tetrakis(carbazol-9-yl)-4,6-dicyanobenzene (4CzIPN), shown in Fig. 1.9b [52], and others [53,54], have realized ultimate $\eta_{\text{ext}} \sim 20\%$ based on both Φ_{PL} and η_{r} close to unity.

Along with the appearance of a new class of TADF emitters for use in OLEDs, the explanation of the TADF-mechanism has also been extended. Recent attempts to describe in more detail the process of RISC in donor-acceptor type aromatic molecules with a small ΔE_{ST} have been made by Zhang *et al.* [47] and Dias *et al.* [55]. Zhang *et al.* have shown blue-emitting TADF molecules with high η_{ext} in OLEDs. Supported by PL spectral data measured at different temperatures in solvents with various polarities, the authors stated that two excited triplet states, ${}^3\pi\text{-}\pi^*$ and ${}^3\text{CT}^*$, exist in CT type TADF aromatic molecules (Fig. 1.10a). An efficient RISC must occur via an initial reverse internal conversion (RIC) between the ${}^3\text{CT}^*$ state and the ${}^3\pi\text{-}\pi^*$ state, the latter being close to or higher than the former in energy. Then, RIC is followed by RISC between the higher lying triplet state and ${}^1\text{CT}^*$ [47]. In addition, Dias *et al.* suggested the presence of a third triplet state, ${}^3\text{n-}\pi^*$, that is supposed to play a key role in TADF. In the model of Dias *et al.*, while RISC should happen from the ${}^3\text{CT}^*$ state to an energetically equal ${}^1\text{CT}^*$ state, this process is preceded by RIC from ${}^3\text{n-}\pi^*$ to the ${}^3\text{CT}^*$ state, as illustrated in Fig. 1.10b [55]. The continuous work on

these and similar models can give us further clues and possibilities for molecular design of highly efficient TADF emitters.

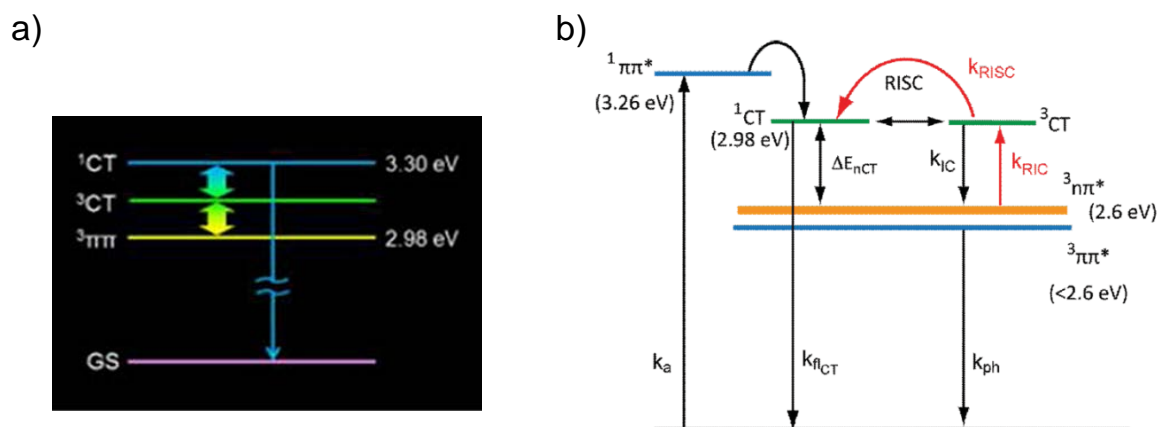


Figure 1.10 Energy level systems explaining TADF proposed a) in Ref. 47 and b) in Ref. 55.

1.2.4 Spiro-Junction to Enhance the Spatial Separation between a Donor and Acceptor

To achieve the lowest possible ΔE_{ST} in CT emitters, it is necessary to completely separate the donor (*D*) and acceptor (*A*) in space. This can be done by forcing the *D* and *A* moieties to stabilize in different planes compared to each other. To achieve this, a spiro-linkage that provides an orthogonally connected π -conjugation between two parts of a molecule can be used (Fig. 1.11). This principle has been successfully utilized by Nakagawa *et al.* [56], who achieved a small ΔE_{ST} of 57 meV with a spirobifluorene derivative. Employing this emitter having Φ_{PL} of 27% in OLEDs resulted in an improved $\eta_{\text{ext}} = 4.4\%$. Additional benefits of a spiro-junction are prevention of crystallization, improvement of processability and morphological stability along with thermal [57-59] and color stabilities [58], and high color purity [60]. For these reasons, a spiro-connection has been used in emitters, host and transport layers in OLEDs [59-61], as well as in molecules displaying amplified spontaneous emission (ASE) [57,62]. Therefore, the spiro-junction is a promising technique to use in TADF emitters.

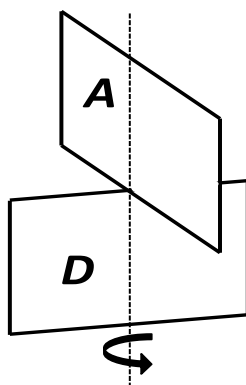


Figure 1.11 Principle of twisting a donor (*D*) and an acceptor (*A*) moiety by inserting a spiro-junction between them.

1.3 How to Utilize a Large Singlet-Triplet Energy Gap in TADF Emitters

1.3.1 Long Triplet Lifetime and its Quenching by Dioxygen

Although the basic principles for designing TADF emitters have been already revealed, these guidelines often do not straightforwardly result in viable TADF materials with a small ΔE_{ST} . This is due to the complex molecular structure and environmental conditions that affect the electronic and spin transitions in these molecules and cannot be accurately and completely modeled at present. Therefore, many of the new materials designed for TADF do not exhibit efficient RISC or have a rather large ΔE_{ST} that leads to a rather long repopulation of the S_1 state from the T_1 state on the order of milliseconds. Even though a long TADF emission may allow for upconversion with high quantum yields in OLEDs at low current densities, the efficiency generally steeply decreases in the high current density region due to TTA [63]. However, operation under high current is necessary for commercial applications such as displays or illumination modules.

An alternative way to utilize TADF emitters with long decay time is in oxygen sensing. The mechanism leading to oxygen sensing in emitters possessing long triplet excited states is depicted in Fig. 1.12. In this process, upon a collision between a fluorophore in the excited state and dioxygen molecule in the ground state condition, the energy transfer from the T_1 level of the fluorophore to the triplet ground state of dioxygen denoted as $O_2(X^3\Sigma_g^-)$ proceeds with high efficiency [64]. In addition, this process results in

the production of singlet oxygen, the lowest singlet excited state of dioxygen, denoted as $O_2(a^1\Delta_g)$. $O_2(a^1\Delta_g)$ reacts with the fluorophore quickly to form peroxides, which easily dissociate and form a wide range of reactive oxygen species (ROS), detrimental to organic compounds. To avoid the degradation of oxygen sensors based on organic emitters, singlet oxygen quenchers need to be used.

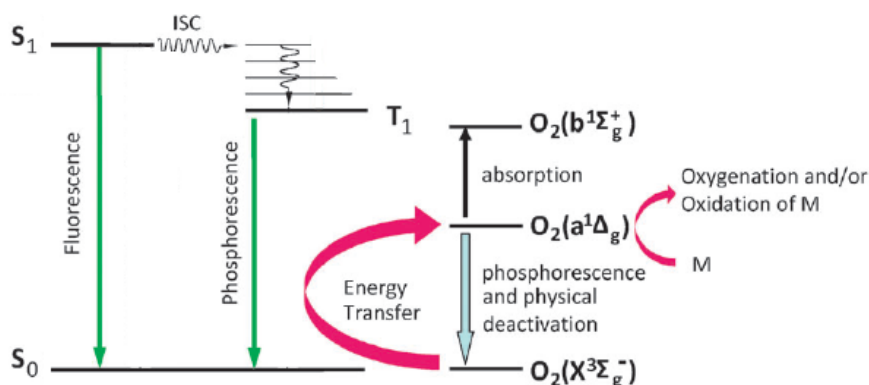


Figure 1.12 Energy level diagram illustrating the production of singlet oxygen. $O_2(b^1\Sigma_g^+)$ is an upper, non-reactive singlet state of O_2 . M means organic molecule. Modified from Ref. 64.

Sensing the concentration of molecular dioxygen is important in various fields of industry and life sciences, and applications include monitoring oxygen levels in exhaust gases from cars, during beer and wine production in the beverage industry, or in food packaging [63]. In a specialized application of pressure sensitive paints (PSP) [65,66], a miniaturized model of an airplane or car is covered by a layer of luminescent paint, and the luminescence intensity of the paint changes depending on oxygen pressure when tested in a specialized wind tunnel (Fig. 1.13a) [65]. Noninvasive monitoring of tumors located several millimeters under the skin or during a surgery is another important application and is possible because tumors tend to induce a hypoxic (oxygen-poor) environment in the tissue where they grow (Fig. 1.13b) [67]. Organic luminescent sensors provide significant improvements, such as faster response and low reactivity with analytes [68], compared to other methods of oxygen detection, *e.g.*, Clark electrodes.

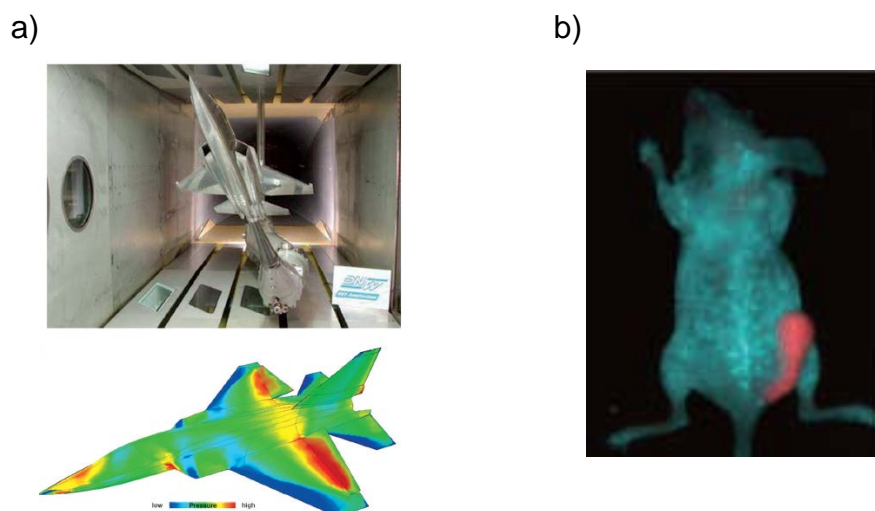


Figure 1.13 a) Oxygen sensing using PSP, from Ref. 66; b) imaging cancer in a mouse from Ref. 67.

1.3.2 The Various Physical Methods to Obtain Long Triplet Lifetime in Molecular Oxygen Sensors

Luminescence-based molecular oxygen sensors have been receiving considerable attention both from academia and industry [69]. Most of the present sensors are based on platinum or palladium porphyrins or on ruthenium- or iridium-containing transition metal complexes [69,68]. These sensors are in fact very similar to the emitters used in OLEDs, and the quenching of their luminance is based on the same principle as shown in Fig. 1.12. The typical parameters of detection, such as sensitivity, dynamic range, and limit of detection, are determined by intrinsic and extrinsic factors. For the extrinsic factors, the host material greatly influences the diffusion time of dioxygen and collision with the light emitting molecule [69]. The intrinsic factors, however, are related to the population and the length of the triplet excited state. In this sense, the triplet excited state of precious metal-containing phosphorescent emitters is mainly influenced by the heavy metal-effect. However, the use of precious metals would make the large-scale production of these sensors expensive compared to metal-free molecules, and, in addition, the strong spin-orbit coupling results in a rather short triplet excited state that limits the sensitivity of O₂ detection.

On the other hand, in TADF emitters, ΔE_{ST} and the ambient temperature are the most important intrinsic factors. Therefore, with a rather large ΔE_{ST} and at a constant temperature, the triplet excited state can be maintained for a long time, leading to high O₂ sensitivities. Indeed, the most sensitive molecular oxygen sensor reported so far was achieved in ¹³C₇₀ with sensitivity on the order of ppm-ppb based on a quenching of the lifetime of its TADF [70]. Long triplet lifetimes based on different physical mechanisms were shown, for example, in metal-free emitters displaying extra-long room temperature phosphorescence [71] and in systems capable of ‘ping-pong-like’ energy transfer between a metal-center and an aromatic ligand [72].

1.4 The Role of Host Matrices in TADF Emitters

Finally, when using a TADF emitter, negative effects resulting from the close contact between single TADF molecules must be avoided. For example, concentration quenching often leads to a large decrease in the Φ_{PL} and lifetime of the delayed component through enhanced non-radiative losses. Another effect, excimer formation, leads to a shift in the emission spectrum and to a decrease in Φ_{PL} . To avoid these detrimental effects, doping into a host material is necessary. One of the most important points to consider when host environment is used is to achieve a good confinement of excitons into the guest molecules. For this, the T₁ level of the host must be higher than that of the guest. Otherwise, unwanted back-energy transfer from the guest to the host would happen [73].

Another negative effect is exciplex formation between a guest *D* or *A* and a host *A* or *D* molecules, one of the *A* or *D* being in the excited state [74]:



Exciplexes can result in non-radiative dissociation, or in charge transfer (CT), yielding unstructured spectral emission profiles, typically red-shifted and lower in quantum efficiency compared to that of the interacting molecules. The decrease in quantum yield is due to an increase in intermolecular phonon interactions, and an overall reduction in the oscillator strength of the dimeric species [74].

1.5 Goals and Motivation - Outline of the Experimental Part

Despite of the extensive efforts to develop high performance OLEDs by both academia and industry, there is still a need for introducing new, highly-efficient organic light-emitters for OLEDs and luminescent oxygen sensors. For example, the heavy metal-based phosphorescent emitters, although allowing for the preparation of high performance OLEDs, have prices tied to the availability of precious metals. Given the advantages of TADF emitters over phosphorescent and fluorescent molecules, as discussed in the previous sections, this thesis introduces a new type of metal-free TADF compound. We show that the new spiro-acridine derivative, ACRF, can be successfully utilized in OLEDs and has strong potential for application in molecular oxygen sensors. Moreover, we demonstrate that the most important PL and EL parameters of this compound, such as quantum yields and decay lifetimes, can be influenced, and therefore tuned for specific application, by using various small molecular host layers.

Chapter 2 contains the details of the experimental methods used throughout the thesis. We present two synthetic routes to obtain ACRF. Besides the fabrication methods of thin films and OLEDs and preparation way of solution samples, the methods used for obtaining the PL and EL results are described. Computation methods are also disclosed.

In **Chapter 3** we introduce ACRF. To achieve CT emission, following the guidelines from the previous sections of this chapter, we construct a *D-A* structure. Furthermore, the spatial separation of the HOMO and LUMO levels is addressed by twisting the conjugation between the *D* and the *A* moieties by a spiro-junction. We characterize the PL properties of ACRF in a neat film and doped into a small molecule host layer. Upon confirmation of an efficient TADF emission in ACRF, we investigate the EL performance of ACRF as an OLED-emitter, thereby mainly focusing on its ability to harvest both singlet and triplet excitons.

Realizing the importance of the host layer for ACRF, we devote **Chapter 4** to study the effects of various small-molecule host layers on the PL and EL performance of ACRF. Among the phenomena considered are energy transfer between the host and the guest molecules, and exciplex formation. Furthermore, since CT emitters have a significantly enhanced dipole moment in the excited state, we study how the PL properties in ACRF can be correlated with dipole field interactions between ACRF and the host molecules. Based

on these effects, by choosing various host materials, we succeed in significant variation in the PL and EL quantum efficiencies and PL transient lifetimes of ACRF.

Chapter 5 demonstrates the quenching of the triplet excited state of ACRF doped into a host film by O₂. We explain the underlying mechanism of this effect, and show the potential of ACRF as an oxygen sensor doped into a polystyrene film, based on the quenching of its PL intensity and transient lifetime.

In **Chapter 6** we summarize and conclude the presented research.

1.6 References

- [1] www.oled-info.com (accessed September 2013: <http://www.oled-info.com/lg-5-flexible-oled-prototype-photo>).
- [2] www.newscenter.philips.com (accessed May 2014: <http://www.newscenter.philips.com/main/standard/news/press/2012/20120119-oled-lighting-for-transparent-car-roof.wpd#.U3geZNKs8E>).
- [3] G. M. Farinola, R. Ragni, *Chem. Soc. Rev.* **40** (2011) 3467.
- [4] G. Schwartz, S. Reineke, T. C. Rosenow, K. Walzer, K. Leo, *Adv. Funct. Mater.* **19** (2009) 1319.
- [5] M. C. Gather, A. Köhnen, K. Meerholz, *Adv. Mater.* **23** (2011) 233.
- [6] H. Sasabe, H. Nakanishi, Y. Watanabe, S. Yano, M. Hirasawa, Y.-J. Pu, J. Kido, *Adv. Funct. Mater.* **23** (2013) 5550.
- [7] Y.-S. Tyan, *J. Photonics Energy* **1** (2011) 011009.
- [8] W. Brütting, J. Frischeisen, T. D. Schmidt, B. J. Scholz, C. Mayr, *Phys. Status Solidi A* **210** (2013) 44.
- [9] C. Adachi, S. Tokito, T. Tsutsui, S. Saito, *Jpn. J. Appl. Phys.* **27** (1988) L269.
- [10] C. Adachi, S. Tokito, T. Tsutsui, S. Saito, *Jpn. J. Appl. Phys.* **27** (1988) L713.
- [11] C. Adachi, T. Tsutsui, S. Saito, *Appl. Phys. Lett.* **56** (1990) 799.

- [12] T. K. Hatwar, M. E. Kondakova, D. J. Giesen, J. P. Spindler in *Organic Electronics: Materials, Processing, Devices and Applications*, ed. by F. So, CRC Press (2010).
- [13] K. Saxena, V. K. Jain, D. S. Mehta, *Opt. Mater.* **32** (2009) 221.
- [14] Z. B. Wang, M. G. Helander, J. Qiu, D. P. Puzzo, M. T. Greiner, Z. M. Hudson, S. Wang, Z. W. Liu, Z. H. Lu, *Nat. Photon.* **5** (2011) 753.
- [15] A. Bay, P. Cloetens, H. Suhonen, J. P. Vigneron, *Opt. Express* **21** (2013) 764.
- [16] M. A. Baldo, D. F. O'Brian, M. E. Thompson, S. R. Forrest, *Phys. Rev. B* **60** (1999) 14422.
- [17] Z. Shuai, D. Beljonne, R. J. Silbey, J. L. Bredas, *Phys. Rev. Lett.* **84** (2000) 131.
- [18] M. Wohlgenannt, K. Tandon, S. Mazumdar, S. Ramasesha, Z. V. Vardeny, *Nature* **409** (2001) 494.
- [19] M. Pope, H. P. Kallmann, P. Magnante, *J. Chem. Phys.* **38** (1963) 2042.
- [20] W. Helfrich, W. G. Schneider, *Phys. Rev. Lett.* **14** (1965) 229.
- [21] W. G. Williams, P. L. Spong, D. J. Gibbons, *J. Phys. Chem. Solids* **33** (1972) 1879.
- [22] P. H. Partridge, *Polymer* **24** (1983) 733.
- [23] P. H. Partridge, *Polymer* **24** (1983) 739.
- [24] P. H. Partridge, *Polymer* **24** (1983) 748.
- [25] P. H. Partridge, *Polymer* **24** (1983) 755.
- [26] S. Hayashi, H. Etoh, S. Saito, *Jpn. J. Appl. Phys.* **25** (1986) L773.
- [27] C. W. Tang, S. A. Van Slyke, *Appl. Phys. Lett.* **51** (1987) 913.
- [28] M. A. Baldo, D. F. O'Brien, Y. You, A. Shoustikov, S. Sibley, M. E. Thompson, S. R. Forrest, *Nature* **395** (1998) 151.

- [29] N. J. Turro, V. Ramamurthy, J. C. Scaiano, *Modern Molecular Photochemistry of Organic Molecules*, University Science Books, Sausalito, California (2009).
- [30] C. Adachi, M. A. Baldo, M. E. Thompson, S. R. Forrest, *J. Appl. Phys.* **90** (2001) 5048.
- [31] C. Adachi, M. A. Baldo, S. R. Forrest, *J. Appl. Phys.* **87** (2000) 8049.
- [32] J. M. Larkin, W. R. Donaldson, T. H. Foster, R. S. Knox, *Chem. Phys.* **244** (1999) 319.
- [33] J. M. Larkin, W. R. Donaldson, R. S. Knox, T. H. Foster, *Photochem. Photobiol.* **75** (2002) 221.
- [34] D. Y. Kondakov, T. D. Pawlik, T. K. Hatwar, J. P. Spindler, *J. Appl. Phys.* **106** (2009) 124510.
- [35] C. Baleizão, S. Nagl, S. M. Borisov, M. Schäferling, O. S. Wolfbeis, M. N. Berberan-Santos, *Chem. Eur. J.* **13** (2007) 3643.
- [36] B. Valeur, *Molecular Fluorescence: Principles and Applications*, Wiley-VCH, Weinheim (2002).
- [37] F. A. Salazar, A. Fedorov, M. N. Berberan-Santos, *Chem. Phys. Lett.* **271** (1997) 361.
- [38] J. C. Fister III, D. Rank, J. M. Harris, *Anal. Chem.* **67** (1995) 4269.
- [39] B. Nickel, *EPA Newsletter* **58** (1996) 9.
- [40] C. A. Parker, *Advances Photochem.* **2** (1964) 305.
- [41] Y. Nishikawa, K. Hiraki, Y. Onoue, K. Nishikawa, Y. Yoshitake, T. Shigematsu, *Bunseki Kagaku* **32** (1983) E115.
- [42] Y. Onoue, K. Hiraki, Y. Nishikawa, *Bull. Chem. Soc. Jpn.* **54** (1981) 2633.
- [43] A. Endo, M. Ogasawara, A. Takahashi, D. Yokoyama, Y. Kato, C. Adachi, *Adv. Mater.* **21** (2009) 4802.

- [44] A. Endo, K. Sato, K. Yoshimura, T. Kai, A. Kawada, H. Miyazaki, C. Adachi, *Appl. Phys. Lett.* **98** (2011) 083302.
- [45] S. Y. Lee, T. Yasuda, H. Nomura, C. Adachi, *Appl. Phys. Lett.* **101** (2012) 093306.
- [46] H. Tanaka, K. Shizu, H. Miyazaki, C. Adachi, *Chem. Commun.* **48** (2012) 11392.
- [47] Q. Zhang, J. Li, K. Shizu, S. Huang, S. Hirata, H. Miyazaki, C. Adachi, *J. Am. Chem. Soc.* **134** (2012) 14706.
- [48] J. Lee, K. Shizu, H. Tanaka, H. Nomura, T. Yasuda, C. Adachi, *J. Mater. Chem. C* **1** (2013) 4599.
- [49] K. Sato, K. Shizu, K. Yoshimura, A. Kawada, H. Miyazaki, C. Adachi, *Phys. Rev. Lett.* **110** (2013) 247401.
- [50] T. Serevičius, T. Nakagawa, M.-C. Kuo, S.-H. Cheng, K.-T. Wong, C.-H. Chang, R. C. Kwong, S. Xiae, C. Adachi, *Phys. Chem. Chem. Phys.* **15** (2013) 15850.
- [51] H. Tanaka, K. Shizu, H. Nakanotani, C. Adachi, *Chem. Mater.* **25** (2013) 3766.
- [52] H. Uoyama, K. Goushi, K. Shizu, H. Nomura, C. Adachi, *Nature* **492** (2012) 234.
- [53] J. Li, T. Nakagawa, Q. Zhang, H. Nomura, H. Miyazaki, C. Adachi, *Adv. Mater.* **25** (2013) 3319.
- [54] Q. Zhang, B. Li, S. Huang, H. Nomura, H. Tanaka, C. Adachi, *Nat. Photon.* **8** (2014) 326.
- [55] F. B. Dias, K. N. Bourdakos, V. Jankus, K. C. Moss, K. T. Kamtekar, V. Bhalla, J. Santos, M. R. Bryce, A. P. Monkman, *Adv. Mater.* **25** (2013) 3707.
- [56] T. Nakagawa, S.-Y. Ku, K.-T. Wong, C. Adachi, *Chem. Commun.* **48** (2012) 9580.
- [57] R. Xia, G. Heliotis, M. Campoy-Quiles, P. N. Stavrinou, D. D. C. Bradley, D. Vak, D.-Y. Kim, *J. Appl. Phys.* **98** (2005) 083101.
- [58] Y. Wu, J. Li, Y. Fu, Z. Bo, *Org. Lett.* **6** (2004) 3485.
- [59] U. Bach, K. D. Cloedt, H. Spreitzer, M. Grätzel, *Adv. Mater.* **12** (2000) 1060.

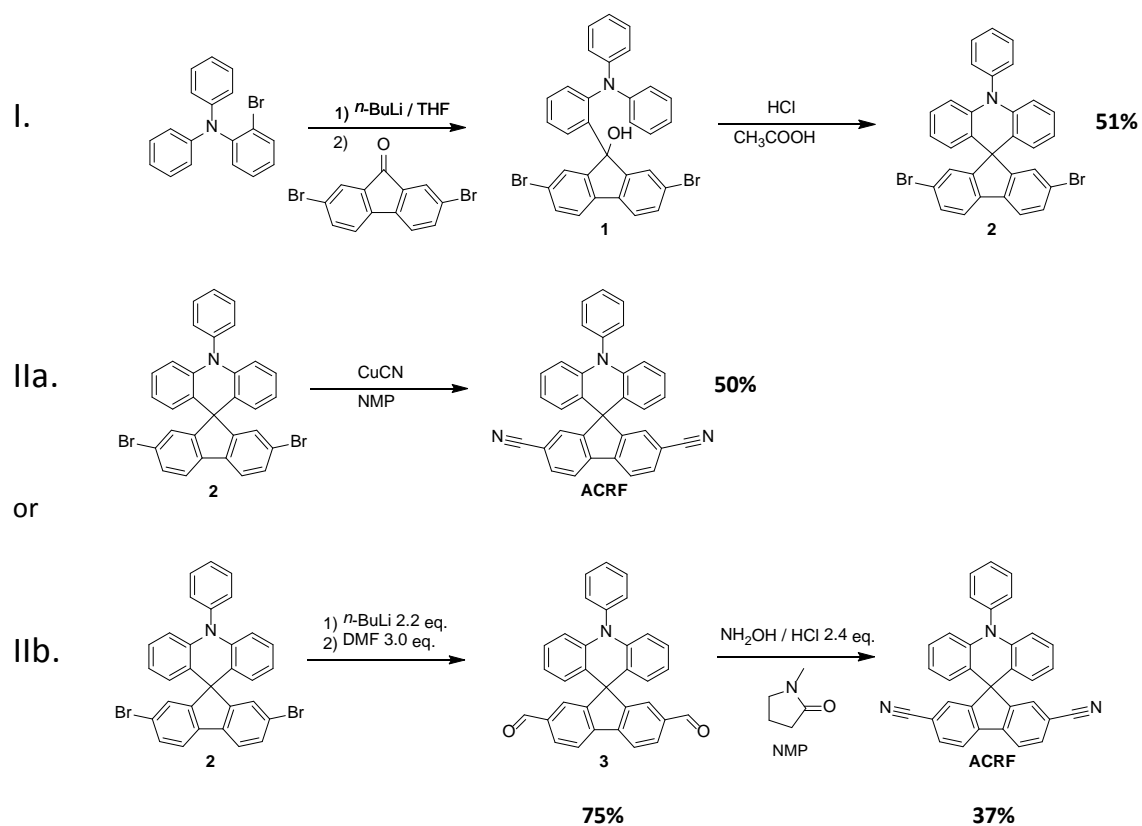
- [60] Y. H. Kim, D. C. Shin, S. H. Kim, C. H. Ko, H. S. Yu, Y. S. Chae, S. K. Kwon, *Adv. Mater.* **13** (2001) 1690.
- [61] W.-Y. Hung, T.-C. Tsai, S.-Y. Ku, L.-C. Chib, K.-T. Wong, *Phys. Chem. Chem. Phys.* **10** (2008) 5822.
- [62] N. Johansson, J. Salbeck, J. Bauer, F. Weissörtel, P. Bröms, A. Andersson, W. R. Salaneck, *Synthetic Metals* **101** (1999) 405.
- [63] C. Adachi, M. A. Baldo, S. R. Forrest, *J. Appl. Phys.* **87** (2000) 8049.
- [64] P. R. Ogilby, *Chem. Soc. Rev.* **39** (2010) 3181.
- [65] J. N. Demas, B. A. DeGraff, P. B. Coleman, *Anal. Chem. News & Features* **71** (1999) 793A.
- [66] M. Schäferling, *Angew. Chem. Int. Ed.* **51** (2012) 3532.
- [67] S. Zhang, M. Hosaka, T. Yoshihara, K. Negishi, Y. Iida, S. Tobita, T. Takeuchi, *Cancer Res.* **70** (2010) 4490.
- [68] R. Ramamoorthy, P. K. Dutta, S. A. Akbar, *J. Mater. Sci.* **38** (2003) 4271.
- [69] Y. Amao, *Microchim. Acta* **143** (2003) 1.
- [70] S. Kochmann, C. Baleizão, M. N. Berberan-Santos, O. S. Wolfbeis, *Anal. Chem.* **85** (2013) 1300.
- [71] S. Hirata, K. Totani, J. Zhang, T. Yamashita, H. Kaji, S. R. Marder, T. Watanabe, C. Adachi, *Adv. Funct. Mater.* **23** (2013) 3386.
- [72] J. E. Yarnell, J. C. Deaton, C. E. McCusker, F. N. Castellán, *Inorg. Chem.* **50** (2011) 7820.
- [73] K. Goushi, R. Kwong, J. J. Brown, H. Sasabe, C. Adachi, *J. Appl. Phys.* **95** (2004) 7798.
- [74] D. Virgili, M. Cocchi, V. Fattori, C. Sabatini, J. Kalinowski, J. A. G. Williams, *Chem. Phys. Lett.* **433** (2006) 145.

Chapter 2

Materials and Methods

2.1 Synthesis of 10-phenyl-10H-spiro[acridine-9,9'-fluorene]-2',7'-dicarbonitrile (ACRF)

The first batches of compound 10-phenyl-10H-spiro[acridine-9,9'-fluorene]-2',7'-dicarbonitrile (ACRF) were synthesized using the procedure outlined in Scheme 1, rows I and IIa. To avoid the dangerous byproduct of CuCN in row IIa, the route in row IIb was used in place of IIa for a later batch of ACRF.



Scheme 1. Synthetic pathway for ACRF.

2.1.1 Synthesis of 2',7'-dibromo-10-phenyl-10H-spiro[acridine-9,9'-fluorene] (2)

First, *n*-BuLi (1.6 M in hexane, 11.2 ml, 18.5 mmol) was added to a solution of 2-bromotriphenylamine (6.0 g, 18.5 mmol) in dry THF (50 ml) at -78 °C, and then the mixture was stirred for 2 h at -78 °C. The reaction solution was added to a solution of 2,7-dibromo-9-fluorenone (5.0 g, 14.8 mmol) in THF (200 ml) and then stirred for 20 h at

room temperature. The reaction mixture was next extracted into ethyl acetate. The organic layer was dried over MgSO₄, filtered, and concentrated *in vacuo*. The resulting product **1** was used in the next reaction without further purification. A mixture of **1** (14.8 mmol), acetic acid (100 ml), and 35-37% HCl (3.0 ml) was stirred for 5 h at 130 °C. The reaction mixture was filtered, and then the residue was washed with methanol and water. The residue was dissolved in THF (1 l) and then filtered through a pad of silica gel. The solution was concentrated *in vacuo*, and then the residue was washed with ethyl acetate/acetone solution to afford a white powder **2** (4.3 g, yield: 51%).

2.1.2 Synthesis of 10-phenyl-10H-spiro[acridine-9,9'-fluorene]-2',7'-dicarbonitrile (ACRF) using Row IIa

A mixture of **2** (2.0 g, 3.5 mmol), CuCN (0.79 g, 8.8 mmol), and *N*-methyl-2-pyrrolidone (50 ml) was heated at 170 °C for 20 h under an N₂ atmosphere. The reaction mixture was added to a solution of NaOH, and then sodium hypochlorite solution was added. The solution was stirred for 30 min, extracted with toluene, and then washed with water. The organic layer was dried over MgSO₄, filtered, and evaporated. The residue was purified by column chromatography (silica, toluene/hexane = 1:2, then toluene/ethyl acetate = 50:1). The residue was further purified by gel permeation chromatography (chloroform), and the resulting yellow needles were recrystallized from acetone/methanol (0.81 g, yield: 50%).

2.1.3 Synthesis of 10-phenyl-4a,9a-dihydro-10H-spiro[acridine-9,9'-fluorene]-2',7'-dicarbaldehyde (**3**)

Drop by drop, *n*-BuLi (1.6 M in hexane, 12.17 ml, 2.2 eq., 19.47 mmol) was added to a solution of compound **2** (4.98 g, 1 eq., 8.81 mmol) and dry THF (200 ml) and stirred for 2-3 h. Next, dimethylformamide (DMF, 2.1 ml, 3.0 eq., 26.6 mmol) was added dropwise, and then the reaction mixture was allowed to warm to room temperature followed by stirring for 3 h. After quenching with a small portion of water, the resulting solution was extracted with CH₂Cl₂, dried over MgSO₄, filtered, and concentrated. The

crude product was purified by column chromatography on silica gel (hexane/CH₂Cl₂ = 1:1 v/v) to afford the desired product **3** as a white solid (3.04 g, yield: 74.5%).

2.1.4 Synthesis of 10-phenyl-10H-spiro[acridine-9,9'-fluorene]-2',7'-dicarbonitrile (ACRF) using Row IIb

The mixture of compound **3** (2.96 g, 1 eq., 6.36 mmol), NH₂OH/HCl (1.06 g, 2.4 eq., 15.31 mmol), and *N*-methylpyrrolidone (NMP, 10 ml) was heated at 120 °C for 2 h. After addition of 35-37% HCl aq. (0.2 ml), the mixture was heated at 120 °C for 4 h. The addition of HCl aq. and heating was continued until conversion is complete, with the progress of conversion monitored by thin-layer chromatography (TLC). After cooling to room temperature, the resulting solution was neutralized by NaHCO₃, extracted with toluene, dried over MgSO₄, filtered, and concentrated. The crude product was purified by column chromatography on silica gel (CHCl₃) and recrystallized from the mixture of toluene and acetonitrile to afford the desired product as a yellow solid. The solid was further purified by vacuum train sublimation (1.10 g, yield: 37.7%).

2.2 Organic Compounds used in OLED Fabrication

Molecular structures of compounds used in OLEDs except for the hosts are shown in Fig. 2.1. We used 1,1-bis[(di-4-tolylamino)phenyl]cyclohexane (TAPC), 1,3-bis(9-carbazolyl)benzene (mCP), and *N,N'*-bis(naphthalen-1-yl)-*N,N'*-bis(phenyl)-2,2'-dimethylbenzidine (α -NPD) as HTLs, and 1,3,5-tri(*m*-pyrid-3-ylphenyl)benzene (TmPyPB) as ETL. Host materials are introduced in Chapters 3 and 4.

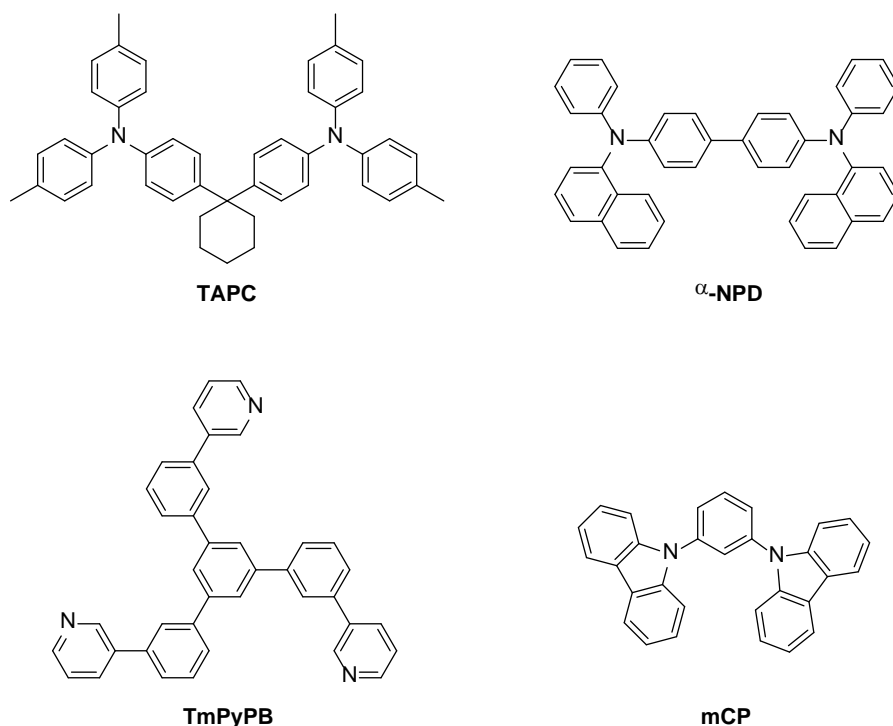


Figure 2.1 Molecular structures used in OLED fabrication.

2.3 Photoluminescence Study

Neat and codeposited films were fabricated on 1-mm-thick quartz and 0.4-mm-thick silicon as substrates *via* high vacuum vapor deposition. Before deposition, the substrates were cleaned with chloroform and acetone in an ultrasonic bath. During fabrication, the vacuum pressure was maintained below 4.0×10^{-4} Pa. The thickness of the organic films was 60-100 nm. All hosts, except for bis(2-(diphenylphosphino)phenyl)ether oxide (DPEPO) and 2,4,6-tris(biphenyl-3-yl)-1,3,5-triazine (T2T) were purchased from Luminescence Technology Corporation with high purities >99%. High purity DPEPO and T2T were prepared in-house.

Absorption spectra were measured with a UV-visible spectrophotometer (UV-2550, Shimadzu). Emission (PL) spectra were recorded using a spectrofluorometer (FP-6500-A-ST, Jasco). Photoluminescent quantum yields were measured with an absolute PL quantum yield spectrometer (C11347 Quantaury QY, Hamamatsu Photonics), incorporating an integrating sphere and a xenon lamp for excitation through a monochromator. To remove oxygen, nitrogen gas was supplied into the spectrometer through a tube that formed a good

seal with the entrance originally intended as a holder for liquid samples. After filling the integrating sphere with nitrogen gas under a constant flow for approximately 5 min, different flow speeds were used to determine the best efficiency. The waiting time between setting a new flow speed and carrying out a measurement was about 2 min.

Transient PL characteristics were measured using a streak camera (C4334, Hamamatsu Photonics) coupled to a monochromator and either a nitrogen gas laser ($\lambda = 337.1$ nm, pulse width ~ 700 ps, repetition rate ≤ 20 Hz; KEN-X, Usho Optical Systems) or an Nd:YAG laser ($\lambda = 266$ nm, pulse width < 15 ns, repetition rate ≤ 10 Hz) as the excitation source. Transient measurements were obtained under atmospheric conditions and low pressure ($10^{-1} \sim 3$ Pa). Low temperature was achieved using a cryostat, which was monitored and controlled by a temperature controller (9700, Scientific Instruments). The principle of light detection by a streak camera is based on time-resolved spectroscopy, illustrated in Fig. 2.2a. The experimental setup used in this study is shown in Fig. 2.2b. Lifetimes τ_p and τ_{del} were determined using the software U8167-01, Version 1.3.0d (Hamamatsu Photonics), and OriginPro ver. 9.0.0, OriginLab Corporation, respectively. The HOMO levels of the neat films deposited on bare silicon wafers were measured using a photoelectron yield spectroscopy (PYS; AC-3E, Riken Keiki).

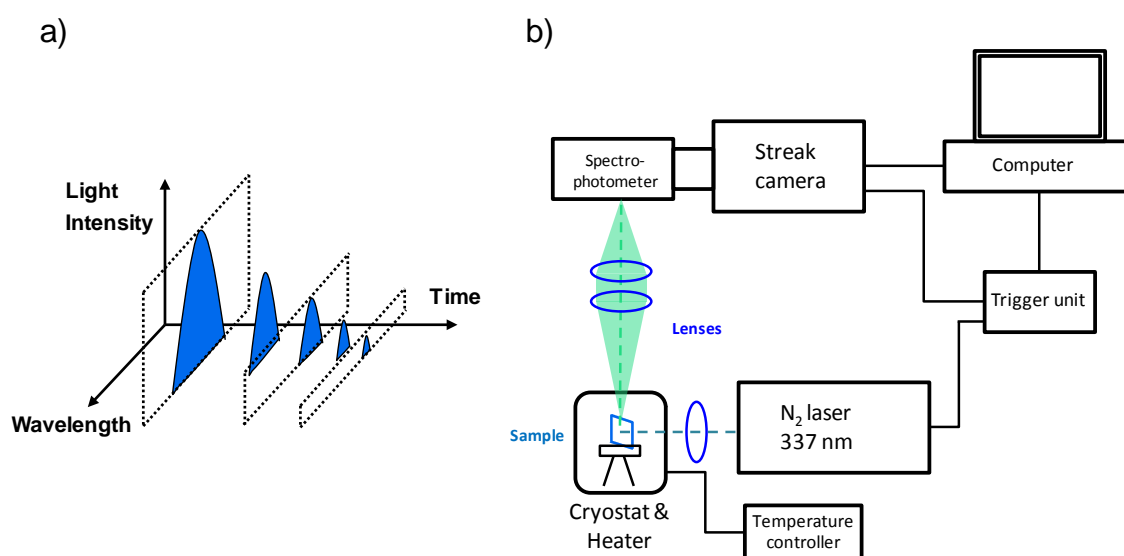


Figure 2.2 a) Principle of time-resolved spectroscopy: the spectral intensity pattern of incident light (blue areas) is recorded at certain time intervals and visualized according to the elapsed time; b) Scheme of the experimental setup of the streak camera system used in this study.

Solutions with various dielectric constants were prepared as a mixture of toluene and acetonitrile. The dielectric constants of the binary solvents were calculated based on Ref. 1. All of the solutions for the PL experiments were degassed by N₂ bubbling for $t > 20$ min.

2.4 Electroluminescence Study

High purity organic materials used for the EL study other than those mentioned previously were purchased from Luminescence Technology Corporation, except for α -NPD, which was prepared in-house. Lithium fluoride was purchased from Wako and aluminum from The Nilaco Corporation. Organic light-emitting diodes were fabricated on the top of glass substrates pre-coated with patterned indium tin oxide (ITO, 110 nm). Prior to device fabrication, the substrates were cleaned by washing with different organic solvents under ultrasonic treatment, heating in excess of isopropanol at 235 °C, and then treating with UV-O₃. The film fabrication method was the same as for the thin films for the PL study with shadow masks used to define the device structure. Substrates were unloaded into a N₂-filled glovebox and the shadow mask changed before reloading and depositing the cathode. The current density-voltage-luminance (J - V - L) characteristics of the OLEDs were measured using a semiconductor parameter analyzer (E5270, Agilent) with an optical power meter (1930, Newport). Electroluminescence spectra were obtained using a spectrometer (USB2000, Ocean Optics).

2.5 Calculations based on Density Functional Theory (DFT)

The following procedure was carried out to calculate the energy properties of ACRF. First, the 2D molecular structure was drawn using the software ChemBioDraw Ultra, and the 3D structure was optimized using ChemBio3D Ultra by minimizing the energy of the molecule with *MM2* mode. The resulting structure was further optimized in Gaussian 09 by performing a density functional theory calculation in B3LYP mode with a 6-31G(d) basis set in the ground state. Using the output of this calculation, the energy properties of ACRF in the excited state (singlet and triplet energy levels, HOMO and LUMO levels, and the distribution of electron density in these levels) were determined using Gaussian 09 with the

same basis set but in time dependent mode. To obtain singlet and triplet energy levels with higher precision, the number of states was set to 10. The ground state dipole moments were part of the log-file of the aforementioned ground state DFT calculation. The excited state dipole moment of ACRF was obtained in TD-DFT mode using the additional command “density=current pop=chelpg”.

2.6 Preparation Method of 2wt% ACRF:PS Films and Determination of Oxygen Quenching Ratio

Mixing of PS (50.6 mg) and ACRF (1 mg) in THF (2 ml) was followed by stirring for >20 min at 60 °C. The solution was allowed to cool to room temperature and spin-coated on quartz substrates (6000 rpm, 30 sec) in air to yield thin films with thicknesses of ~240 nm. The decrease in intensity by O₂-quenching was determined by measuring the PL quantum yield using Quantaaurus QY: the sample was placed in a quartz cuvette, sealed with a rubber septum and bubbled with either N₂ or O₂ gas for >20 min or filled with air to give concentrations of 0, 100, and 21% of O₂. The quenching of the delayed lifetime was determined using the streak camera setup in vacuum and air conditions. The PL experiments were performed at ~25 °C.

2.7 Reference

- [1] A. Jouyban, S. Soltanpour, H.-K. Chan, *Int. J. Pharm.* **269** (2004) 353.

Chapter 3

Enhanced Electroluminescence Efficiency in a Spiro-Acridine Derivative through Thermally-Activated Delayed Fluorescence

3.1 Introduction to ACRF

Organic light-emitting diodes (OLEDs) are expected to find use in large-scale consumer electronics applications including general illumination and displays because of their advantages over current technologies in terms of luminescent properties, power consumption, and shape and size variability [1]. The quantum-statistical branching ratio of the electron-hole pairs under electrical excitation means that the internal quantum efficiency (η_{int}) of fluorescent OLEDs is limited to 25%, whereas phosphorescent OLEDs can achieve η_{int} of 100% because both singlet and triplet excitons can be harvested [2]. Although phosphorescent OLEDs have reached their η_{int} limit [3], they have some disadvantages, including lower electroluminescence efficiency under high current densities [4] and rather low reliability in the blue region for practical applications.

To overcome these problems, alternative radiative exciton formation processes have been explored. Thermally-activated delayed fluorescence (TADF, E-type delayed fluorescence) is a promising way to obtain high radiative exciton formation efficiency (η_r) by converting spin-forbidden triplet excitons up to the singlet level, *i.e.*, by promoting reverse intersystem crossing (RISC). One useful strategy to minimize the overlap between the wave functions is to localize the electron densities of the HOMO and LUMO on donor and acceptor moieties, respectively [6]. Additional steric separation that is achieved by introducing a spiro-junction or bulky substituents between the acceptor and donor units also helps this effect [6]. Based on the former idea, we recently demonstrated TADF in a spirobifluorene derivative to produce an OLED with $\eta_{\text{ext}} = 4.4\%$, despite its rather low Φ_{PL} value of 27% [12]. We followed the design considerations outlined above and synthesized a donor-acceptor structure consisting of an acridine donor that is spiro-conjugated in the C-9 position of a fluorene unit. Two CN groups were attached to the fluorene moiety to enhance its electron-accepting ability. The structure of the resulting molecule, 10-phenyl-10H-spiro[acridine-9,9'-fluorene]-2',7'-dicyanide (ACRF), is shown in Fig. 3.1a. The electron density of the LUMO state is localized on the nitrile-functionalized fluorene acceptor, while that of the HOMO state is localized on the acridine donor, as predicted by time-dependent density functional theory (TD-DFT) calculations in Gaussian 09 (Fig. 3.1b). The value of ΔE_{ST} was calculated to be just 0.0083 eV, thus suggesting potentially high RISC.

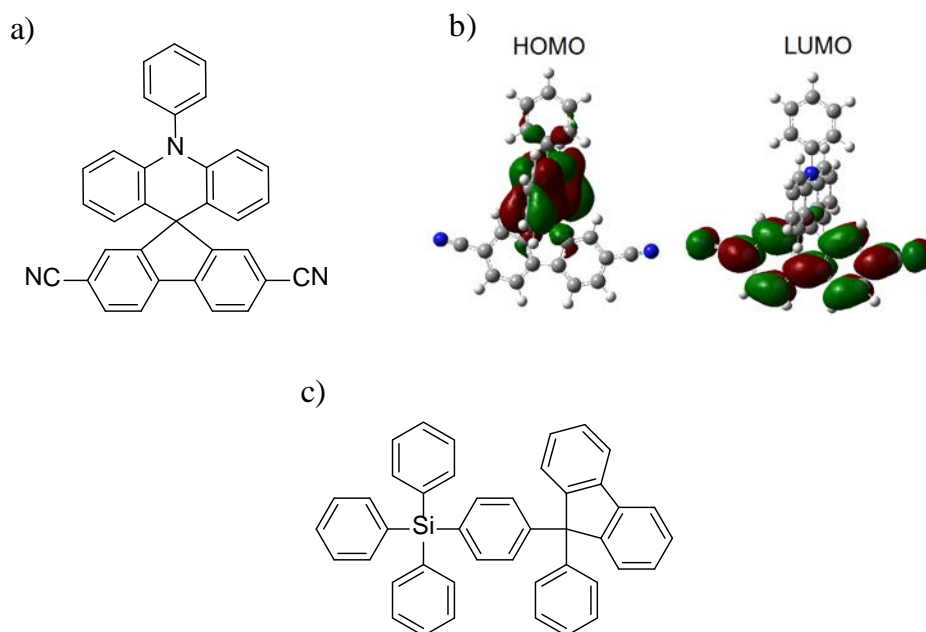


Figure 3.1 a) Molecular structure of ACRF. b) Electron density distributions in the HOMO and LUMO states calculated by TD-DFT in Gaussian 09 at the B3LYP/6-31G(d) level. c) Molecular structure of TPSi-F host.

3.2 Photoluminescent Properties

Upon UV excitation, a pure ACRF film exhibited a broad greenish-yellow emission centered around 530 nm with a large Stokes shift of approximately 100 nm (Fig. 3.2; all experiments presented herein were carried out at room temperature, unless otherwise stated). The characteristic unstructured band with a full width at half maximum (FWHM) of almost 100 nm is assumed to be the result of charge transfer (CT) between the donor and acceptor units. Bearing in mind that this material is intended for use as an emitter in OLEDs, its absolute Φ_{PL} value of 5.5% in a neat film is considered to be low. To avoid self-quenching, ACRF was doped into a triphenyl-[4-(9-phenyl-9H-fluoren-9-yl)phenyl]silane (TPSi-F; Fig. 3.1c) [13] host layer, which has a wide energy gap. Host molecules must possess a higher T_1 energy than the guest to prevent backward energy transfer from the guest to the host layer. All further analyses were performed using a codeposited film containing 6wt% ACRF in TPSi-F. The values of the T_1 levels were derived from the phosphorescence peaks of a pure TPSi-F film (2.74 eV) and an ACRF film (2.50 eV) at low temperatures (36 K and 11.5 K, respectively).

The PL emission spectrum of the codeposited film showed a CT emission peak at 485 nm, which was blue-shifted compared to the peak of pure ACRF, and another low intensity peak around 315 nm originating from the host molecules; this peak was not observed in the spectrum of ACRF (Fig. 3.2). The Φ_{PL} value of the codeposited film measured in air at atmospheric pressure (10.7%) was almost twice as high as that of the neat film (5.5%). In contrast, a relatively high Φ_{PL} value of approximately 67% was observed for a 6wt% ACRF:TPSi-F codeposited film in a nitrogen rich environment.

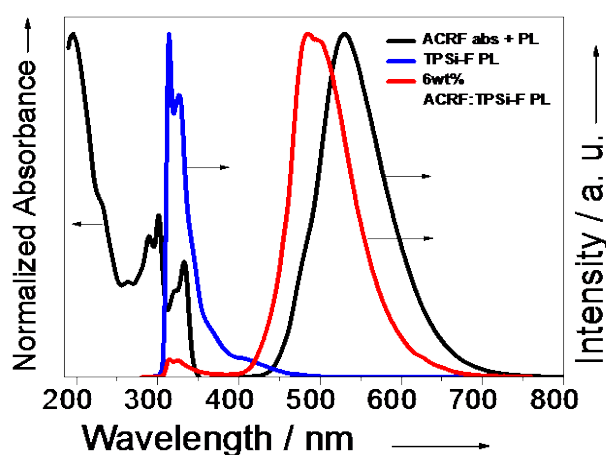


Figure 3.2 Absorption and fluorescence spectra of a neat ACRF film (black); fluorescence spectra of a TPSi-F neat film (blue) and a co-deposited film containing 6wt% ACRF in TPSi-F (red).

To gain better insight into the photophysical processes leading to the highly efficient PL of the 6wt% doped film, we measured the transient PL using a streak camera both in air and under vacuum (ca. 3 Pa). As shown in Fig. 3.3, the PL exhibits second-order exponential decay in air, where the delayed component (assigned to weak TADF) decays completely within approximately 4 ms (the lifetime of the delayed component is $\tau_{\text{del}} \approx 0.41$ ms, listed in Table 3.1). In contrast, under vacuum, the delayed component's contribution increased significantly (the emission spectrum is embedded in Fig. 3.3). In fact, even after around 40 ms, a low-intensity peak corresponding to the main peak of the guest could still be resolved ($\tau_{\text{del}} = 3.9$ ms). The sensitivity of the emission to oxygen and the presence of the delayed component with the long emission decay time in the fluorescence spectral region are typical of TADF. In the latter case, the best fitting was

achieved by using a third-order exponential decay model. The relative and absolute contributions of the efficiencies of prompt and delayed (TADF) fluorescence to that of the overall luminescence are listed in Table 3.2 and were calculated according to the integrated photon counts for fluorescence (Int_F) and delayed fluorescence (Int_{TADF}) listed in Table 3.1. In air, the TADF component makes a larger contribution than the fluorescence (Φ_{rel_F} and Φ_{rel_TADF} , the relative efficiencies of the fluorescence and the TADF to Φ_{PL} , respectively, have a ratio of 0.36:0.64), thus giving Φ_{PL} values of fluorescence (Φ_F) and TADF (Φ_{TADF}) of 3.86% and 6.84%, respectively. Under vacuum, while the Φ_{PL} value of the prompt component had a somewhat higher value of 4.87%, the delayed emission had a very high efficiency of $\Phi_{TADF} = 62.43\%$, thus meaning that $\Phi_{rel_F} / \Phi_{rel_TADF} = 0.07:0.93$.

The experimental value for ΔE_{ST} , which could explain the high efficiency of TADF, was estimated from the fluorescence and phosphorescence spectra of the codeposited film (Fig. 3.4). The streak data measured at room temperature over time spans of 200 ns and 10 ms, respectively, showed that the prompt spectrum was slightly blue-shifted compared to the delayed spectrum, and the low-temperature phosphorescence spectrum was slightly red-shifted in comparison to the delayed spectrum at room temperature. From the spectra shown in Fig. 3.4, the value of ΔE_{ST} was experimentally determined to be 0.10 eV. Because of the difficulty in determining the S_1 level exactly from the PL spectrum, we also calculated ΔE_{ST} using the Berberan–Santos method (shown in Fig. 3.5) [19], and obtained a value of 0.028 eV, which is much closer to that of the theoretical prediction of 0.0083 eV. From the same analysis, we determined the ISC yield (Φ_{ISC}) to be a very high value of 96.4%. In accordance with the Φ_{ISC} value, the ISC rate constant (k_{isc}) was found to be $7.4 \times 10^7 \text{ s}^{-1}$. The method of determination of k_{isc} can be found in the Appendix.

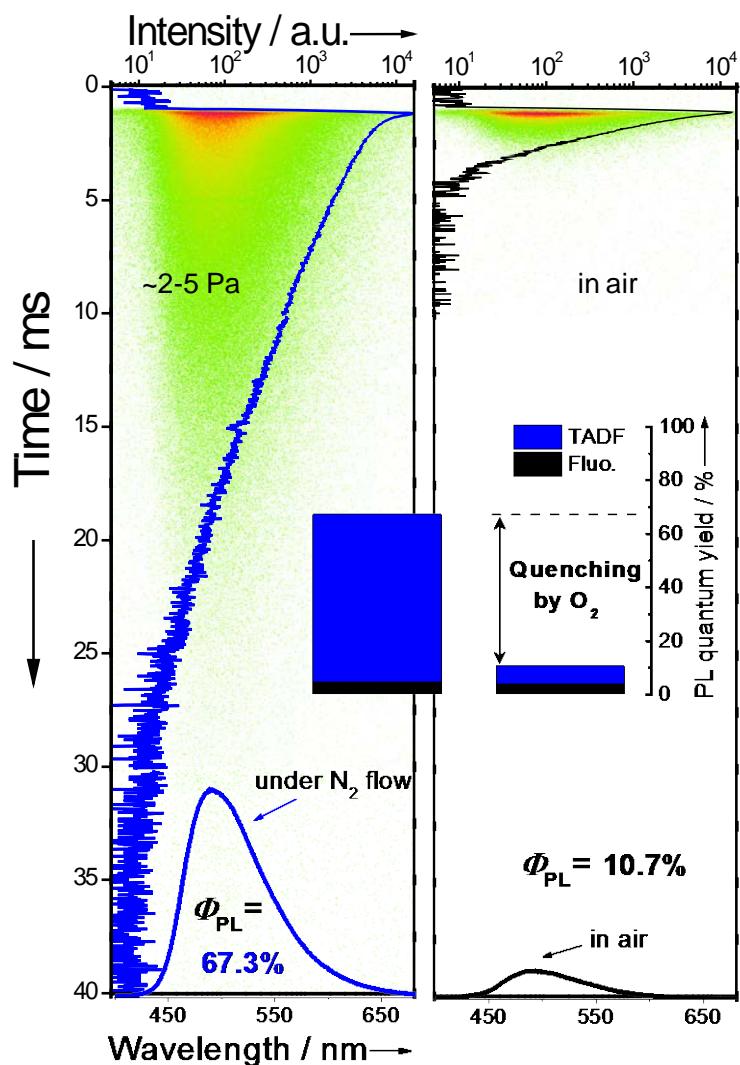


Figure 3.3 Transient PL decay curves for a co-deposited film of 6wt% ACRF:TPSi-F measured using a streak camera under atmospheric conditions (black) and a vacuum of ~ 3 Pa (blue), which are integrated into the streak images by matching the time and spectral axes (the number of green dots is proportional to the photon count; coloring towards red indicates higher photon counts). Embedded at the bottom are the PL spectra measured by a spectrometer with an integrating sphere at constant absorption before (black) and after (blue) the elimination of oxygen from the equipment by nitrogen gas saturation. The percentages indicate Φ_{PL} for corresponding events. The embedded rectangular diagrams represent combined results from transient decays and Φ_{PL} showing the relative contributions from fluorescence and TADF to the overall emission.

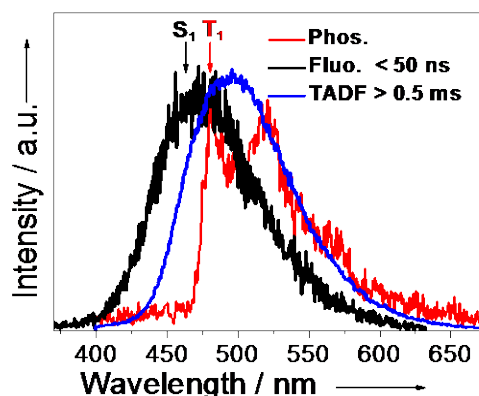


Figure 3.4 PL emission spectra of a co-deposited film of 6wt% ACRF:TPSi-F recorded with a streak camera. Fluorescence (black) and TADF (blue) spectra were recorded at room temperature using <50 ns and >0.5 ms time windows of a 200 ns and a 10 ms time ranges, respectively. The phosphorescence (red) spectrum was measured at 10 K, using a time range of 10 ms, and omitting the prompt fluorescence.

Table 3.1 Data extracted from the transient characterization of a 6wt% ACRF:TPSi-F film

Conditions	τ_1^a [ms]	τ_2^a [ms]	τ_3^a [ms]	A1 ^a	A2 ^a	A3 ^a	τ_p^b [ns]	Int _F ^c	Int _{TADF} ^d	Int ₅₀ ^e
Atmospheric	0.13	0.41	–	0.76	0.37	–	12.9	73691	130731	46119
Oxygen-free	0.16	0.94	3.90	0.55	0.22	0.32	13.0	77887	998985	45746

^a) Obtained from the multiexponential fitting of the transient decay curves on 10 ms scale. ^b) Obtained from the second order exponential fitting of the transient decay curves on 200 ns scale. ^c) Integrated photon count for the first 0.27 ms of the PL for a 10 ms range. ^d) Integrated photon count from 0.27 to 4.36 ms (atmospheric) or 39 ms (oxygen-free) of the PL for a 10 ms range (in the case of 39 ms, we used multiple delays in 10 ms time windows). ^e) Integrated photon count for the first 50 ns of the decay for a 200 ns range.

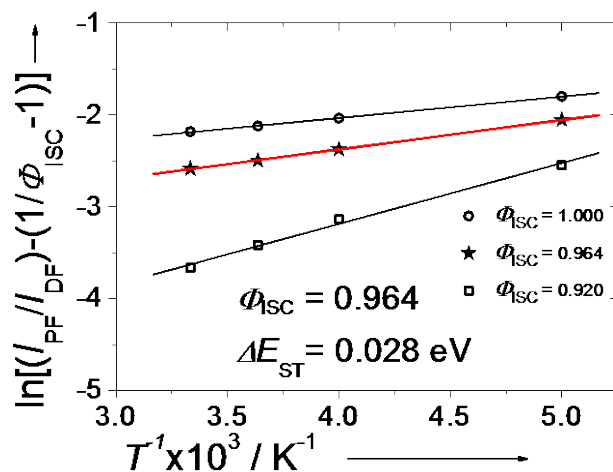


Figure 3.5 Berberan-Santos plot [19,12] in the temperature range from 200 K to 300 K. I_{PF} and I_{DF} are the quantum efficiencies of the prompt and delayed components, respectively, taken from the data plotted in Fig. 3.6. The red line shows the best linear fit achieved by using $\Phi_{ISC} = 0.964$.

Finally, to prove the thermal activation of TADF, we monitored the PL emission in a temperature range from 5 K to 325 K and estimated the temperature-dependent values for Φ_{PL} and for the prompt and delayed emissions. The upconversion through TADF starts around 100 K, and a complete spectral transformation from the characteristic $\pi-\pi^*$ shape of phosphorescence to the CT^* shape of delayed fluorescence occurs around 200 K, as shown in Fig. 3.6.

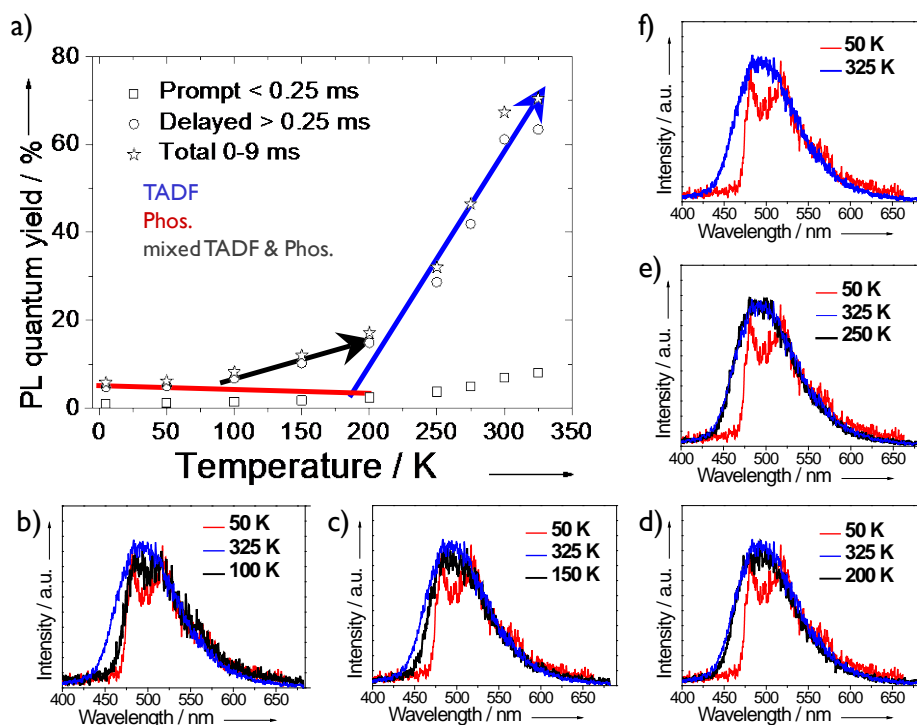


Figure 3.6 a) Temperature dependence of quantum efficiencies of 6wt% ACRF:TPSi-F film, measured by streak camera under vacuum conditions. b-e) PL emission spectra of delayed components from a) at selected temperatures.

3.3 Electroluminescent Performance

An emissive molecule with a high Φ_{PL} value of approximately 67% with a large TADF component enables excitons to be generated with high efficiency in OLEDs. A multilayer OLED that was designed to exceed the limitations of the fluorescence-based OLEDs was fabricated. Figure 3.7a shows the HOMO and LUMO levels of the molecules used in this device. The OLED structure was: indium tin oxide (ITO; 110 nm)/1,1-bis[(di-4-tolylamino)phenyl]cyclohexane (TAPC; 40 nm)/1,3-bis(9-carbazolyl)benzene (mCP; 5 nm)/6wt% ACRF:TPSi-F (20 nm)/1,3,5-tri(*m*-pyrid-3-ylphenyl)benzene (TmPyPB; 35 nm)/lithium-fluoride (LiF; 1 nm)/aluminum (Al; 62 nm). We used 6wt% ACRF:TPSi-F as the emitting layer. TAPC and TmPyPB (T_1 levels of 2.87 eV [14] and 2.78 eV, [15] respectively) served as the hole and electron transport layers, respectively. The thin mCP layer was used as a hole transport layer with a high T_1 level for better carrier balance and to reduce the potential barrier for holes travelling from the TAPC layer into the emitting

layer. The EL spectrum of this device recorded at 10 mAcm^{-2} and assigned to the TADF emitter is almost identical to the PL spectrum of the codeposited film (Fig. 3.7b). The dependence of η_{ext} on the device current density is presented in Fig. 3.7c (black line). The OLED achieved a high η_{ext} of 10.1% at a low current density of $3.3 \times 10^{-4} \text{ mAcm}^{-2}$. This value of η_{ext} approaches the theoretical maximum ($\eta_{\text{ext(t)}}$), which was calculated to be 12.7% by a method that we previously reported [12]. Because our device structure was not fully optimized, we expect the value of η_{ext} to increase upon careful device optimization. The value of η_{ext} decreased rapidly with increasing current densities above $10^{-3} \text{ mAcm}^{-2}$; this effect can be ascribed to triplet-triplet annihilation (TTA). The experimental results fitted the theoretical curve for the TTA model well (red line in Fig. 3.7c) [16]. The current density-and brightness dependence from operating voltage is shown in Fig. 3.7d.

For TADF-based OLEDs, the larger the contribution from delayed emission, the more the radiative exciton formation is enhanced. In the case of ACRF, the relatively high η_{ext} value at low current densities is clearly a result of thermally-harvested triplet excitons, with a high η_r of 75.0-94.3% [17]. This high radiative exciton-formation yield is far superior to that of conventional fluorescence-based OLEDs (25%) and approaches that of the best phosphorescence-based OLEDs (100%).

Table 3.2 PL efficiencies of a 6wt% ACRF:TPSi-F film and EL efficiencies of the OLED device.

Conditions	Φ_{PL} [%]	$\Phi_{\text{F}}^{\text{a)}$ [%]	$\Phi_{\text{TADF}}^{\text{a)}$ [%]	$\Phi_{\text{rel}_F}^{\text{a)}$	$\Phi_{\text{rel}_\text{TADF}}^{\text{a)}$	$\eta_{\text{ext(t)}}$ [%]	η_{ext} [%]
Atmospheric	10.7	3.9	6.8	0.36	0.64	0.25	–
Oxygen-free	67.3	4.9	62.4	0.07	0.93	12.7	10.1

^{a)} Method of determination is described in the appendix.

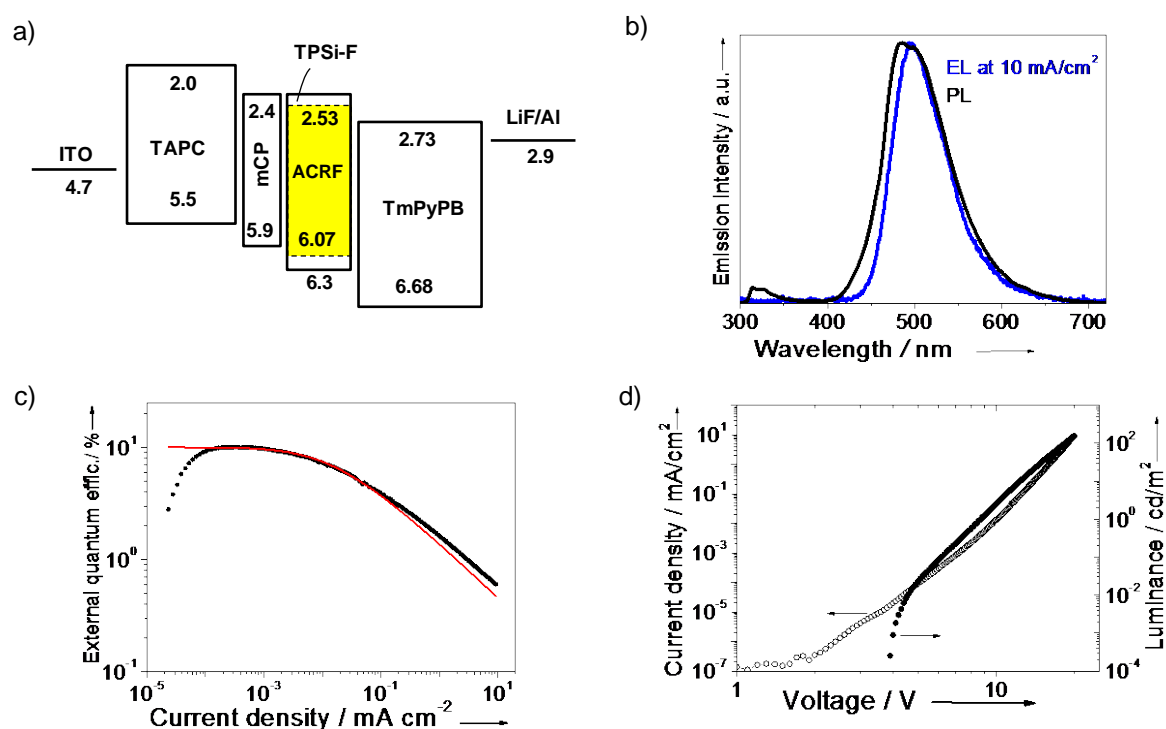


Figure 3.7 a) Energy diagram of organic materials used in the prototype OLED. b) PL (black) and EL (blue) spectra measured from this OLED. c) External quantum efficiency (η_{ext}) determined from the current density characteristics of this device. The red line in c) represents the fitting of the TTA model [16]. d) Current density and brightness characteristics of the OLED from a).

3.4 Conclusions

We have demonstrated highly efficient TADF from a spiro-acridine derivative with a high Φ_{PL} value (67.3%) in the solid state at room temperature. The contribution of the delayed fluorescence significantly exceeded that of the prompt fluorescence. An OLED using this molecule as an emitter achieved a maximum η_{ext} value of 10.1%, which is twice the theoretical maximum for a conventional fluorescence-based OLED with Φ_{PL} of 100%. Efficient quenching of the delayed fluorescence by atmospheric oxygen was also observed in the solid state. We believe that optimized designs using this molecular backbone will enhance the TADF performance. These inexpensive, organic aromatic compounds with such high PL efficiencies are attractive for applications such as OLEDs and molecular oxygen sensors.

3.5 References

- [1] M. C. Gather, A. Köhnen, K. Meerholz, *Adv. Mater.* **23** (2011) 233.
- [2] M. A. Baldo, D. F. O'Brien, Y. You, A. Shoustikov, S. Sibley, M. E. Thompson, S. R. Forrest, *Nature* **395** (1998) 151.
- [3] C. Adachi, M. A. Baldo, M. E. Thompson, S. R. Forrest, *J. Appl. Phys.* **90** (2001) 5048.
- [4] M. A. Baldo, C. Adachi, S. R. Forrest, *Phys. Rev. B: Condens. Matter Mater. Phys.* **62** (2000) 10967.
- [5] A. Endo, M. Ogasawara, A. Takahashi, D. Yokoyama, Y. Kato, C. Adachi, *Adv. Mater.* **21** (2009) 4802.
- [6] A. Endo, K. Sato, K. Yoshimura, T. Kai, A. Kawada, H. Miyazaki, C. Adachi, *Appl. Phys. Lett.* **89** (2011) 083302.
- [7] J. C. Deaton, S. C. Switalski, D. Y. Kondakov, R. H. Young, T. D. Pawlik, D. J. Giesen, S. B. Harkins, A. J. M. Miller, S. F. Mickenberg, J. C. Peters, *J. Am. Chem. Soc.* **132** (2010) 9499.
- [8] Q. Zhang, T. Komino, S. Huang, S. Matsunami, K. Goushi, C. Adachi, *Adv. Funct. Mater.* **22** (2012) 2327.
- [9] K. Goushi, K. Yoshida, K. Sato, C. Adachi, *Nat. Photon.* **6** (2012) 253.
- [10] a) B. Valeur, *Molecular Fluorescence: Principles and Applications*, Wiley-VCH, Weinheim (2002) p. 41; b) C. Baleizão, S. Nagl, S. M. Borisov, M. Schäferling, O. S. Wolfbeis, M. N. Berberan-Santos, *Chem. Eur. J.* **13** (2007) 3643.
- [11] a) F. A. Salazar, A. Fedorov, M. N. Berberan-Santos, *Chem. Phys. Lett.* **271** (1997) 361; b) J. C. Fister III, D. Rank, J. M. Harris, *Anal. Chem.* **67** (1995) 4269.
- [12] T. Nakagawa, S.-Y. Ku, K.-T. Wong, C. Adachi, *Chem. Commun.* **48** (2012) 9580.
- [13] P.-I. Shih, C.-H. Chien, C.-Y. Chuang, C.-F. Shu, C.-H. Yang, J.-H. Chen, Y. Chi, *J. Mater. Chem.* **17** (2007) 1692.

- [14] T.-Y. Kim, D.-G. Moon, *Trans. Electr. Electron. Mater.* **12** (2011) 84.
- [15] S.-J. Su, T. Chiba, T. Takeda, J. Kido, *Adv. Mater.* **20** (2008) 2125.
- [16] C. Adachi, M. A. Baldo, S. R. Forrest, *J. Appl. Phys.* **87** (2000) 8049.
- [17] Upper and lower limit values of radiative exciton formation efficiency (η_r) are calculated using $\eta_{\text{ext}(t)} = 12.7\%$ and $\eta_{\text{ext}} = 10.1\%$, and $\Phi_{\text{PL}} = 67.3\%$ with assumption of career balance ($\gamma = 100\%$) and light outcoupling efficiency ($\eta_p = 20\%$). $\eta_r = \eta_{\text{ext}} / (\gamma \times \Phi_{\text{PL}} \times \eta_p)$.
- [18] S. Nagl, C. Baleizão, S. M. Borisov, M. Schäferling, M. N. Berberan-Santos, O. S. Wolfbeis, *Angew. Chem. Int. Ed.* **46** (2007) 2317.
- [19] M. N. Berberan-Santos, J. M. M. Garcia, *J. Am. Chem. Soc.* **118** (1996) 9391.

Chapter 4

Influence of Host Matrix on Thermally-Activated Delayed Fluorescence: Effects on Emission Lifetime, Photoluminescence Quantum Yield, and Device Performance

4.1 Introduction

Thermally-activated delayed fluorescence (TADF) occurs in organic aromatic molecules in which the lowest singlet-triplet energy splitting (ΔE_{ST}) is small enough to allow thermal activation from triplet to singlet excited states via reverse intersystem crossing (RISC), resulting in delayed fluorescence [1]. To promote highly efficient RISC, ΔE_{ST} should be less than a hundred meV [2]. However, most conventional molecules possess a large ΔE_{ST} and low RISC efficiency, so the application of TADF to emitter materials saw limited interest. Recently, by tailoring the molecular design to achieve a small ΔE_{ST} , we have demonstrated many classes of highly efficient TADF emitters. These new emitters are a promising cost-effective alternative to the best phosphorescent organometallic emitters that are widely used today in organic light-emitting diodes (OLEDs) for displays and illumination [2,3].

When neat films of the emitter molecules are used as the emitter layer in OLEDs, performance is often poor because of concentration quenching, unwanted excimer emission, aggregation, and other effects [4]. These losses can often be reduced and performance improved by doping the emitter molecules, also called the guest, into a film comprised of appropriate host molecules. The design of host-guest systems demonstrating highly efficient delayed luminescence originating from triplet excitons has been shown to require careful consideration of the intermolecular interactions between host and guest molecules [5]. While the effects of host molecules on the photophysical processes of phosphorescent compounds have been studied thoroughly in the past ten years [6], only a limited number of similar studies concerning TADF emitters exist [7].

The spiro-acridine compound 10-phenyl-10H-spiro[acridine-9,9'-fluorene]-2',7'-dicarbonitrile (ACRF), which we recently reported as a TADF emitter, is an ideal candidate for investigating how the host can affect the TADF behavior of guest molecules because the triplet excitons in ACRF have rather long transient lifetimes [8]. When ACRF is doped into a small-molecule host layer, intense TADF can be observed in an oxygen-free environment, and an external quantum efficiency (η_{ext}) of ~10% was achieved by using the doped films in OLEDs [8]. On the other hand, neat films of ACRF result in a very weak TADF component due to the concentration quenching-effect [8]. Thus, the choice of host can greatly impact the emission properties, and understanding the

interaction between guest and host molecules is important for the further development of devices based on TADF.

In this study, we investigate how the host layer affects the photoluminescence (PL) properties of the TADF emitter ACRF in solid-state films. We carefully analyze the host dependence of the TADF emission in ACRF based on transient radiative decays, absolute PL quantum yields (Φ_{PL}), and changes in PL spectra. We show that the host can impact both Φ_{PL} and the lifetime of the delayed emission, and we discuss the various mechanisms that can account for these changes. We propose a mechanism to explain how some hosts can lead to much longer delayed lifetimes based on shifts in the emission spectra and their temperature dependence. Furthermore, we study the OLED performance of these host-guest films as emitters and the factors affecting η_{ext} . Through these comprehensive PL and electroluminescence (EL) studies, we clarify some of the criteria for the selection of host molecules to enhance and tailor specific properties of TADF.

4.2 Results and Discussion

4.2.1 Photoluminescence Lifetime of ACRF:Host Layers

To explore the host-guest interactions, we used a series of small-molecule host matrices with a variety of chemical structures and energy gaps. Similar to when phosphorescent emitters are used, the T_1 level of the host molecule (T_1^{H}) should be higher than that of the guest (T_1^{G}) to prevent back-energy transfer from the TADF guest to the host [9]. Therefore, hosts with T_1^{H} close to or higher than T_1^{G} were chosen. The host molecules used in this study were triphenyl-(4-(9-phenyl-9H-fluoren-9-yl)phenyl)silane (TPSi-F), which we used as an efficient host in our previous study [8], 1,3,5-tri(*m*-pyrid-3-yl-phenyl)benzene (TmPyPB) [10], 2,4,6-tris(biphenyl-3-yl)-1,3,5-triazine (T2T) [11], 2,6-dicarbazo-1,5-pyridine (PYD2) [12], 9-(4-*tert*-butylphenyl)-3,6-bis(triphenylsilyl)-9H-carbazole (CzSi) [13], and bis(2-(diphenylphosphino)phenyl)ether oxide (DPEPO) [14]. The chemical structures and T_1 levels are shown in Fig. 4.1. The T_1 levels were determined from the onset of the phosphorescence spectra in neat films for the hosts (Fig. 4.2) and in a 2-methyltetrahydrofuran solution for ACRF. The molecules TmPyPB, TPSi-F, and T2T

have very similar T_1^H of 2.80, 2.84, and 2.86 eV, respectively, which are slightly higher than that of ACRF ($T_1^G = 2.62$ eV). The other host molecules possess higher T_1 levels. The T_1^H is 3.03 and 3.09 eV in PYD2 and CzSi, respectively, and DPEPO has the highest T_1^H of 3.38 eV.

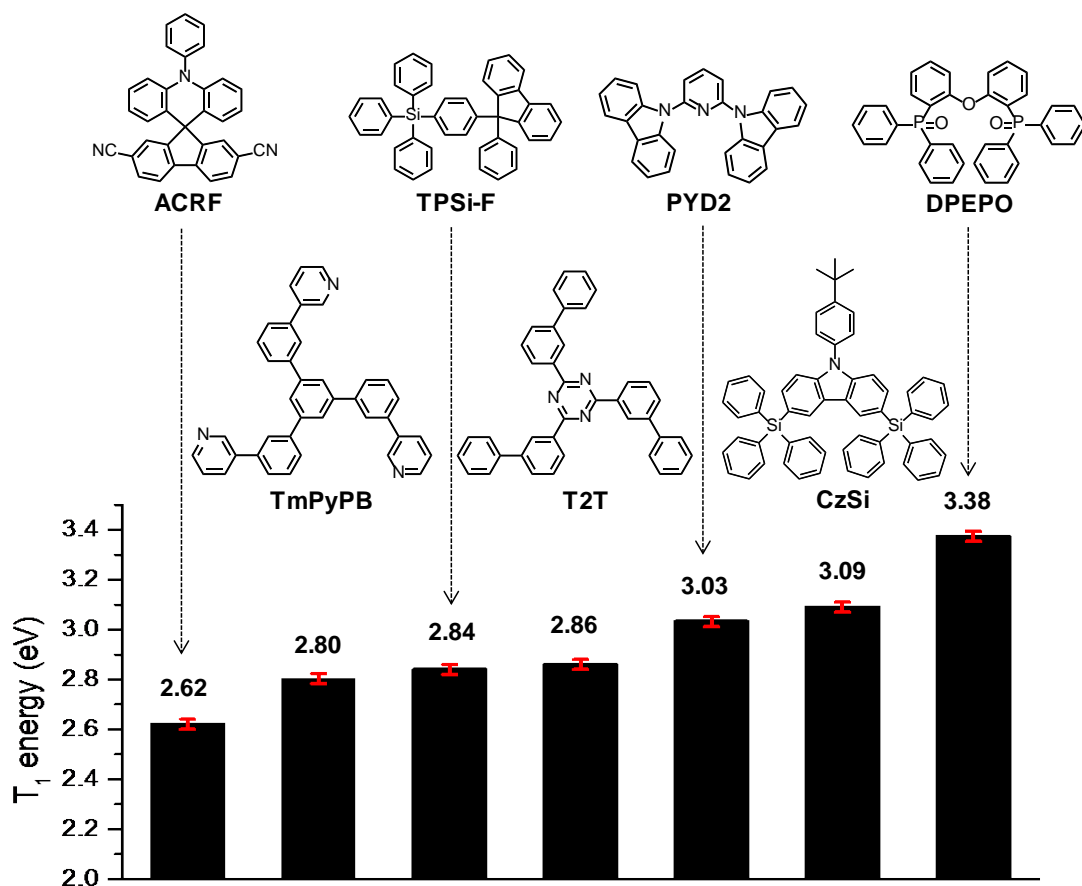


Figure 4.1 The molecular structures and T_1 levels of ACRF and the hosts used in this study. The error bars of ± 0.02 eV represent the uncertainty in determining the onset of the phosphorescence spectra.

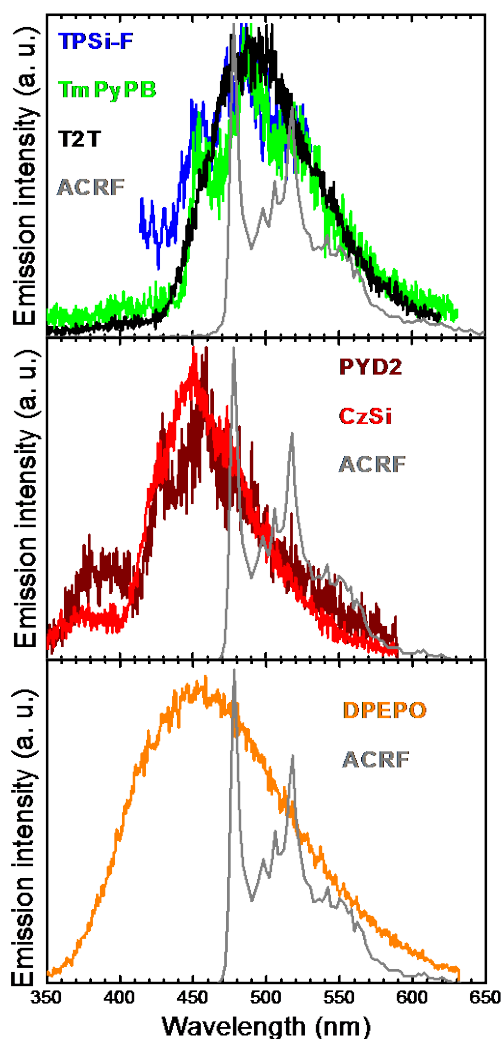


Figure 4.2 Phosphorescence spectra of the host neat films of TPSi-F, TmPyPB, T2T, PYD2, CzSi, and DPEPO taken at low temperatures (<20 K), and ACRF in 2MeTHF taken at 77 K. The shoulder peaks around 370 nm in PYD2 and CzSi correspond to their fluorescence spectra.

Figure 4.3 shows the emission decay profiles of the various host-guest thin films measured under vacuum over a time range of 50 ms. The doping concentrations of the guest molecules in the host layers were 2 or 6 wt% to exclude any effect from concentration quenching between ACRF molecules, as verified by separate Φ_{PL} measurements. Remarkable differences in the length of the decay were observed despite using the same guest in each case. Photoluminescence lasting longer than 50 ms was detected for the hosts of CzSi and DPEPO, and the delayed emission in an ACRF-doped

CzSi film under N₂ flow was visible even after turning off the excitation source. Much shorter emission signals were observed in TPSi-F and PYD2, lasting ca. 25 and 20 ms, respectively. Finally, almost no delayed signal was observed in TmPyPB and T2T films after about 5 ms.

On the other hand, the emission in solution completely differs from that in solid state. While the PL was on the order of milliseconds in all of the guest-host films, a 10⁻⁵ mol/l solution of ACRF in oxygen-free acetonitrile showed only a weak PL that decayed rapidly over a time range of 10 μs, as shown in Fig. 4.4. Weak emission and low Φ_{PL} , as shown in Table 4.1, were also observed in other organic solvents with varying polarities and at different concentrations. The much lower Φ_{PL} in solution compared to solid-state films, listed in Table 4.2 and discussed later, indicate the presence of a strong non-radiative loss channel in the solution state from the collision of ACRF and solvent molecules. Therefore, the behavior of ACRF excitons in the liquid state is very different from that in the solid state. Because our focus is the choice of host in solid-state devices and the situation in solution is significantly different, we leave the detailed investigation of solution-state effects to a future study.

Table 4.1. PL quantum efficiencies of ACRF determined in solvents with various dipole moments and concentrations of emitter.

Solvent	Concentration [mol/l]	Φ_{PL} [%]	$\mu^{\text{a)}}$ [D]
Toluene	2.2×10 ⁻⁴	2.3±0.1	0.36
Toluene	2.2×10 ⁻⁵	2.9±0.1	0.36
Toluene	2.2×10 ⁻⁶	2.6±0.1	0.36
Chloroform	4.2×10 ⁻⁵	16.6±0.1	1.04
Chloroform	4.2×10 ⁻⁶	12.8±0.1	1.04
2Me-THF	2.2×10 ⁻⁵	3.0±0.2	1.38
Acetonitrile	2.2×10 ⁻⁵	4.2±0.1	3.92

^{a)} Dipole moment of solvent.

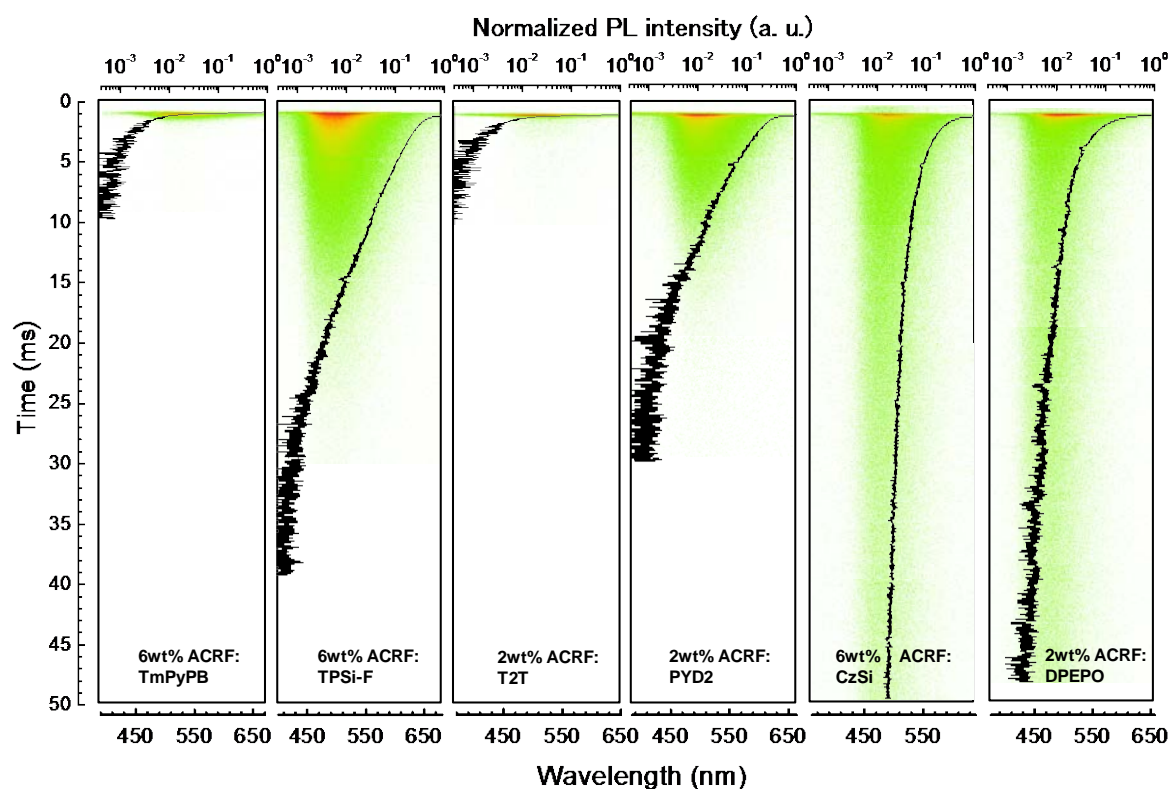


Figure 4.3. Transient PL decay images measured under vacuum at room temperature by a streak camera for ACRF doped into various hosts. Red and yellow color areas correspond to higher photon counts, while green areas correspond to lower photon counts. Black lines indicate the evolution of the total PL intensity over time. The doping concentration was 2 or 6 wt%.

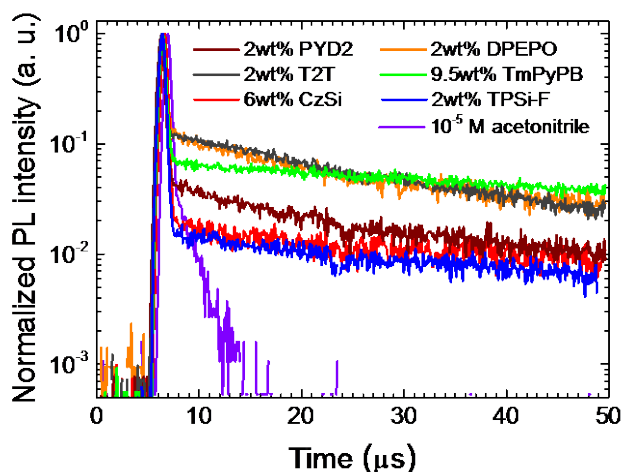


Figure 4.4 Transient PL decay profiles of ACRF doped into various host layers, and diluted in acetonitrile at the concentration of 10^{-5} mol/l. Measured under vacuum (except for acetonitrile, which was degassed by N_2 purge) at room temperature.

Similar to the host-guest films here, a ms-order delayed emission has also been previously reported for organometallic phosphorescent emitters doped into small-molecule hosts [5]. In those cases, the delayed emission originated from a mutual energy transfer between the energetically close triplet states of the guest and the host. However, very long delayed components exceeding 50 ms were observed for ACRF even in hosts with significantly higher T_1 energies than that of ACRF. Thus, such a mutual energy transfer cannot explain the long PL decay in the CzSi and DPEPO host matrices.

In TADF molecules, the prompt component of PL originates from the radiative decay of initially generated singlet excitons. The delayed emission is produced from singlet excitons that have passed through a triplet state via one or more cycles of intersystem crossing (ISC) followed by RISC. As shown by the normalized transient emission characteristics on a 100 ns time scale in Fig. 4.5 [15], the decay time constant of the prompt component (τ_p) is nearly independent of the host matrix. Thus, the differences in the delayed components of the PL decays should be due to processes involving the triplet excitons. The lifetimes of the prompt and delayed (τ_{del}) components for all of the host-guest systems are listed in Table 4.2 with additional time scales shown in Fig. 4.6.

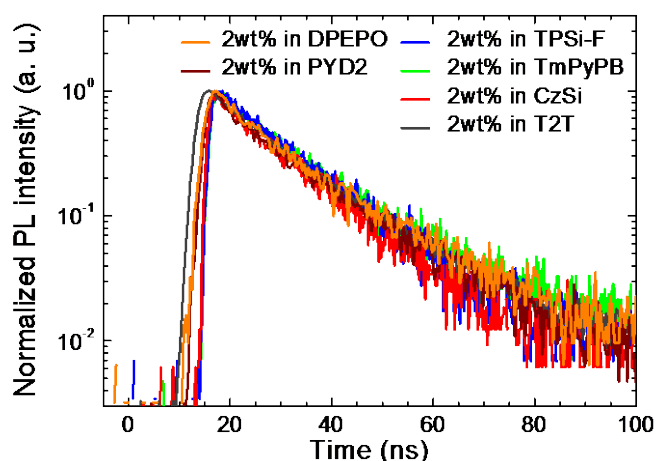


Figure 4.5 Transient PL decay of ACRF doped into various hosts measured under vacuum at room temperature on a time scale of 100 ns.

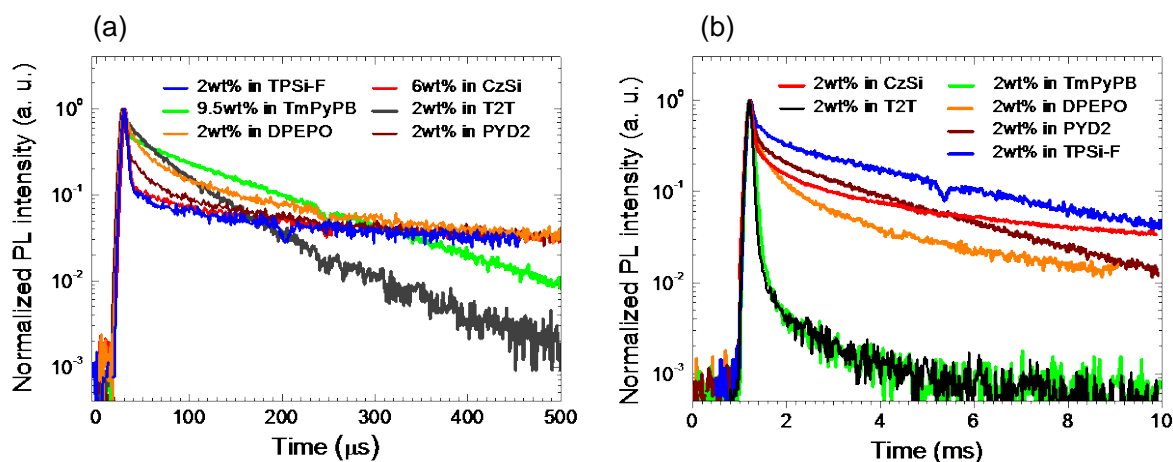


Figure 4.6 Transient PL decay profiles of ACRF doped into various host layers in the time range of (a) 500 μ s and (b) 10 ms. Measured under vacuum at room temperature.

Another possible reason for the long decay curves is if the rate of energy transfer from the host to the guest is somehow reduced. In such cases, the PL decay when the guest is directly excited is expected to be different than when the guest and host are simultaneously excited because energy transfer is not required in the case of direct excitation. Figure 4.7 shows the PL decay dependence on the excitation wavelength (λ_{exc}) and the absorption spectra of neat films of the molecules. The long decay component is present in the DPEPO film regardless of whether only the guest ($\lambda_{exc} = 337$ nm) or both the

host and guest molecules ($\lambda_{\text{exc}} = 266 \text{ nm}$) are excited. Because the absorption spectrum of CzSi completely overlaps with that of ACRF (Fig. 4.7b), excitation of only the guest is not possible. However, the fractions of excitons generated on the host and guest molecules should depend on λ_{exc} because the absorbance of CzSi relative to that of ACRF is significantly higher at $\lambda_{\text{exc}} = 266 \text{ nm}$ than at $\lambda_{\text{exc}} = 337 \text{ nm}$. Since long delayed emission is observed regardless of λ_{exc} , the long delayed emission cannot be attributed to a host-dependent mechanism that slows the energy transfer rate from the host to the guest.

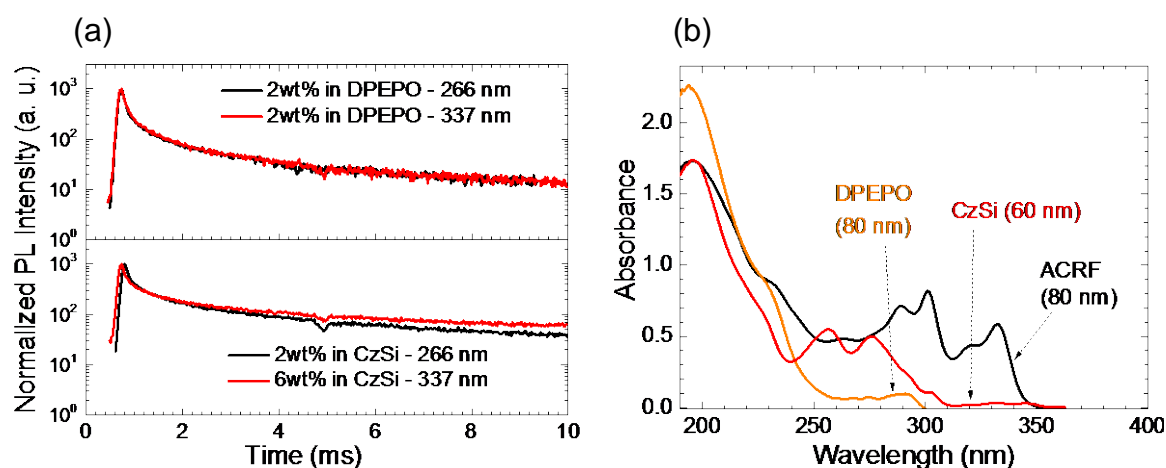


Figure 4.7 (a) Transient PL decay profiles of ACRF doped into DPEPO and CzSi host layers excited at $\lambda_{\text{exc}} = 266$ and 337 nm ; (b) Absorption spectra of ACRF, DPEPO, and CzSi. The numbers in parentheses indicate the thickness of each film.

Table 4.2 Transient decay times and Φ_{PL} of ACRF:host films, and EL quantum efficiencies of corresponding devices.

Hosts	$\tau_p^{\text{a)}$ [ns]	$\tau_{\text{del}}^{\text{b)}$ [ms]	Φ_{PL} [%]	$\lambda_{\text{exc}}^{\text{d)}$ [nm]	η_{int} [%]	η_{ext} [%]	$\eta_{\text{ext(t)}}$ [%]
TmPyPB	14.9±1	2.3±0.1 ^{c)}	47.8±2.0	256	44.8±1.9	9.1±0.3	9.0±0.4
TPSi-F	13.0±1	4.2±0.3	68.5±2.1	276	67.2±1.9	7.2±0.3	13.4±0.4
T2T	15.4±1	4.3±0.1 ^{c)}	14.4±0.9	296	12.4±0.8	2.9±0.3	2.5±0.2
PYD2	15.6±1	3.6±0.3	69.2±0.7	294	67.7±1.3	7.7±0.3	13.5±0.3
CzSi	15.9±1	70.0±5.0	61.3±2.0	276	60.3±5.4	8.4±0.3	12.1±1.1
DPEPO	15.2±1	22.0±2.0	68.8±2.8	290	67.6±7.2	12.2±0.3	13.5±1.4

^{a)} Transient decay time was obtained from first order exponential fitting of transient decay curves measured over 100 or 200 ns scales. ^{b)} Lifetimes of delayed components obtained from multi-exponential fitting of transient decay curves over 50 ms scale and ^{c)} 10 ms scale. ^{d)} λ_{exc} was used to obtain the Φ_{PL} values.

4.2.2 Photoluminescence Quantum Yield and Quenching by Host Matrix

A change in the transient decay is often accompanied with a change in Φ_{PL} . Figure 4.8 shows Φ_{PL} of ACRF-doped films at 2 or 6 wt% concentration as a function of T_1^{H} and the corresponding PL spectra. ACRF shows high Φ_{PL} of 60-70% in PYD2, CzSi, and DPEPO host matrices due to the complete confinement of triplet excitons in the ACRF. On the other hand, the three hosts with similar T_1^{H} show significant variations in Φ_{PL} , with $\Phi_{\text{PL}} = 68.5 \pm 2.1\%$ in TPSi-F, $47.8 \pm 2.0\%$ in TmPyPB, and $14.4 \pm 0.9\%$ in T2T. Thus, the large differences in Φ_{PL} when TmPyPB, TPSi-F, and T2T are used as hosts cannot be well explained by back-energy transfer from T_1^{G} to T_1^{H} . In addition, we can assume that the low Φ_{PL} is not caused by insufficient energy transfer from the S_1 energy level of the host to the S_1 of the guest in TmPyPB and T2T films. This is because films with both high and low Φ_{PL} show a small-intensity host peak at short wavelengths (Fig. 4.8b) [16].

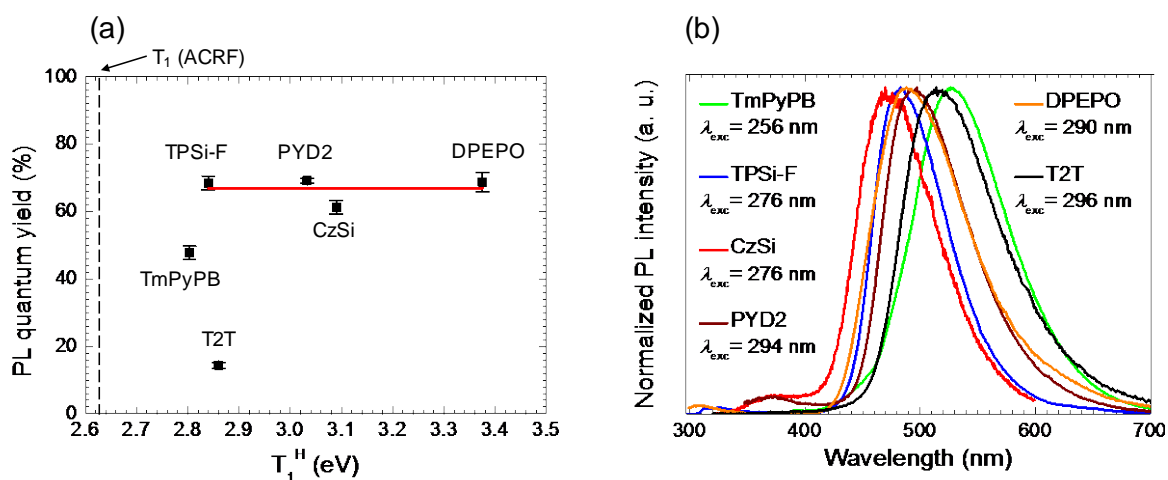


Figure 4.8 (a) The Φ_{PL} of ACRF doped into different hosts plotted according to T_1^H . Measurements were made under the flow of N_2 at room temperature; red line is a linear fit excluding doped TmPyPB and T2T. (b) Emission spectra of the doped films measured under N_2 flow and excited at the same λ_{exc} as (a).

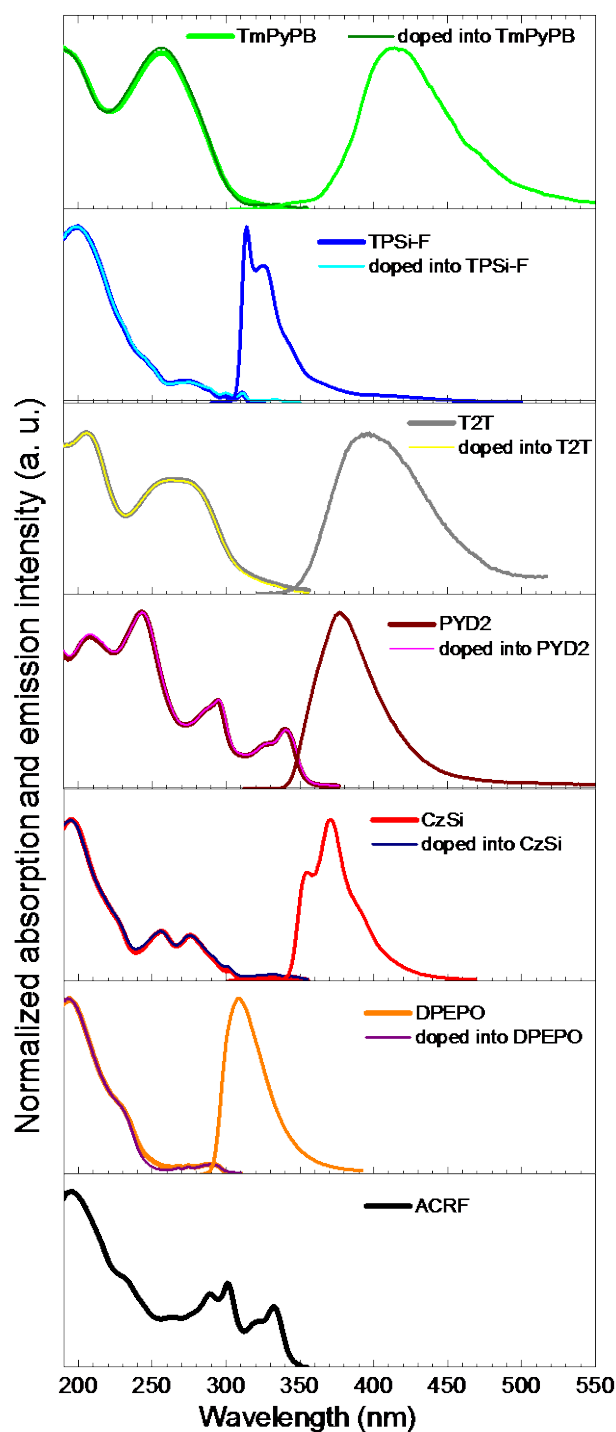


Figure 4.9. Absorption spectra of ACRF and the host neat and doped films, and emission spectra of host layers. All samples were measured at room temperature under atmospheric condition.

One mechanism that can lead to quenching of emission is the formation of exciplexes between a guest and a host molecule. Exciplexes can reduce Φ_{PL} by increasing

the non-radiative decay rate (k_{nr}) of the guest molecule [17]. Exciplex emission usually has a lower Φ_{PL} and a broad, unstructured, and red-shifted emission spectrum compared to those of the isolated molecules [17]. Furthermore, the energy difference between the highest occupied molecular orbital (HOMO) of the molecule acting as the electron acceptor and the lowest unoccupied molecular orbital (LUMO) of the molecule acting as the electron donor (ΔE_{DA}) must be smaller than the energy gap (E_g) of each participating molecule for exciplex formation to occur.

To confirm exciplex formation, we investigated the emission spectra and the relationship between the observed Φ_{PL} and the HOMO/LUMO gaps between ACRF and the host materials (Table 4.3). As shown in Fig. 4.10a, the PL spectra of TmPyPB and T2T films are clearly red-shifted compared to those of the other films, suggesting the possibility of exciplex formation [18]. As ACRF is a CT-complex with both electron-donating (acridine) and electron-accepting (dicyanitrile-fluorene) moieties, we suppose that it may take the role of either the donor or acceptor in an exciplex. The minimum ΔE_{DA} for each combination of ACRF and host was estimated from the energy levels shown in Fig. 4.10c. From this analysis, ACRF is expected to form virtually no exciplexes with DPEPO and TPSi-F with $\Delta E_{DA} = 3.6 \text{ eV} \approx E_g(\text{ACRF})$, and the same behavior is expected in the case of CzSi and PYD2 with $\Delta E_{DA} = 3.5 \text{ eV}$. On the other hand, $\Delta E_{DA} = 3.4 \text{ eV}$ for TmPyPB-ACRF and 3.0 eV for T2T-ACRF clearly suggest the possibility for the formation of exciplexes, as shown in Fig. 4.10b. Exciplex emission with a similarly high ΔE_{DA} has been recently published in the literature [18c]. Thus, the lower Φ_{PL} and shorter delayed lifetime for doped TmPyPB and T2T films can be ascribed to the formation of exciplexes that result in an enhancement of k_{nr} . However, the differences in Φ_{PL} and exciplex formation still cannot explain the approximately one order of magnitude difference in τ_{del} for CzSi and DPEPO compared to TPSi-F and PYD2.

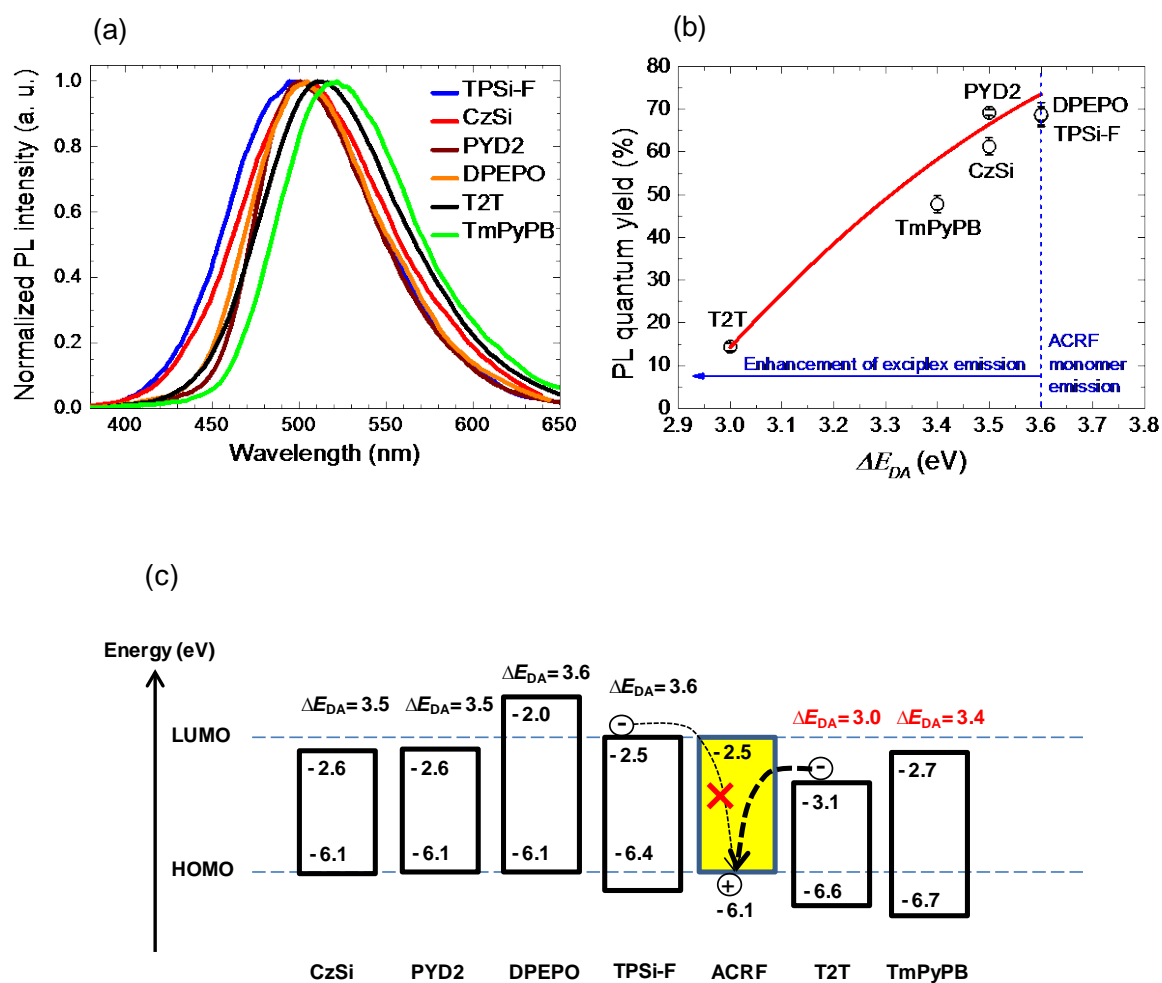


Figure 4.10 (a) PL spectra of 2wt% doped films collected over a 45 μ s integration time measured at room temperature under vacuum via a streak camera. (b) The Φ_{PL} of the doped host-guest films as a function of ΔE_{DA} . (c) HOMO and LUMO energy levels of ACRF and host layers used for determining the lowest ΔE_{DA} .

Table 4.3 Experimentally determined HOMO and LUMO levels of all hosts and ACRF, ΔE_{DA} .

Host or Guest	HOMO ^{a)} [eV]	LUMO ^{b)} [eV]	ΔE_{DA} ^{c)} [eV]	E_g ^{d)} [eV]
TmPyPB	-6.7	-2.7	3.4	4.0
TPSi-F	-6.4	-2.5	3.6	3.9
T2T	-6.6	-3.1	3.0	3.5
PYD2	-6.1	-2.6	3.5	3.5
CzSi	-6.1	-2.6	3.5	3.5
DPEPO	-6.1	-2.0	3.6	4.1
ACRF	-6.1	-2.5	-	3.6

^{a)} Determined by using AC-3 photoelectron yield spectroscopy. ^{b)} LUMO = HOMO - E_g ; E_g is a HOMO-and LUMO gap determined by the absorption edge of each layers. ^{c)} ΔE_{DA} is a gap between the HOMO level of ACRF minus the LUMO levels of hosts. ^{d)} Determined from the onset of absorption spectra of neat films.

In addition, reverse energy transfer from triplet exciplexes to adjacent host molecules during their long triplet lifetime is another mechanism that must be considered for TmPyPB and T2T. If such a reverse energy transfer is occurring, Φ_{PL} should increase with an increasing dopant concentration because of a reduced probability for unwanted triplet exciton transfer from the exciplexes to the host. In fact, TmPyPB host films doped with 2, 6, and 9.5 wt% ACRF resulted in Φ_{PL} of $36.2 \pm 1.5\%$, $47.8 \pm 2.0\%$, and $43.7 \pm 2.0\%$, respectively, while T2T host films at 2 and 6 wt% resulted in Φ_{PL} of $10.6 \pm 0.9\%$, and $14.4 \pm 0.9\%$, respectively. The increasing Φ_{PL} with concentration suggests that reverse energy transfer may occur in addition to exciplex formation, with concentration quenching appearing around 9.5 wt%, but separating the two contributions is difficult.

4.2.3 Mechanism for Host Dependence of Delayed Fluorescence Lifetime

4.2.3.1 Dynamic Change in ΔE_{ST} during Emission Decay

The very long delayed emission in DPEPO and CzSi hosts is expected to be directly related to ΔE_{ST} . This is because the efficiency of RISC (Φ_{RISC}) and the rate of TADF at a given temperature are expected to be determined by ΔE_{ST} , as described by the Boltzmann relationship of $\Phi_{RISC} \sim \exp(-\Delta E_{ST}/kT)$, where k is the Boltzmann constant and T

is temperature. Indeed, previous reports show that TADF emitters with $\Delta E_{ST} < \sim 100$ meV exhibited a rapid RISC with μs -order (10^{-6} - 10^{-4} s) decay of the delayed component [2,3c]. On the other hand, emitters with $\Delta E_{ST} > \sim 100$ meV resulted in a ms-order (10^{-3} - 10^{-2} s) decay [3b] or virtually no occurrence of TADF [3b]. However, the values of $\Delta E_{ST} = S_1^G - T_1^G$ calculated from the onset of the prompt fluorescence (S_1^G) and low temperature phosphorescence spectra (T_1^G) of the ACRF-doped films (Table 4.4) are not well correlated with the PL decay lifetimes. Detailed consideration of the change in the emission spectrum with time can provide additional information for understanding the energetic processes occurring in the films.

In the PL characteristics of the films with long delayed components, we observed an unusual spectral shift: following an immediate red shift after the prompt emission, the PL spectrum gradually blue shifts over time back to the spectrum of the prompt fluorescence, as illustrated with a doped DPEPO film in Fig. 4.11. The red-shifted TADF emission was recorded during the initial several μs after the start of the delayed emission for all of the hosts. The subsequent blue shift was observed hundreds of μs after the red shift.

Figure 4.12a summarizes S_1^G and T_1^G along with the energies of the maximally red-shifted (E_{RED}) and blue-shifted (E_{BLUE}) emission as a function of T_1^H for each film (Table 4.4). Each of the energies was determined from the onset of the appropriate emission spectrum [19]. While the red shift occurred in all of the host-guest systems, the blue shift was only observed in the hosts of DPEPO and CzSi, which also completely confine the triplet excitons in the guest (Fig. 4.13). Although good exciton confinement is also achieved in PYD2, the blue shift was small (Fig. 4.13) and long-lived emission was not observed. Figure 4.14 shows how the onset energies of the emission spectra shift in time for these three hosts.

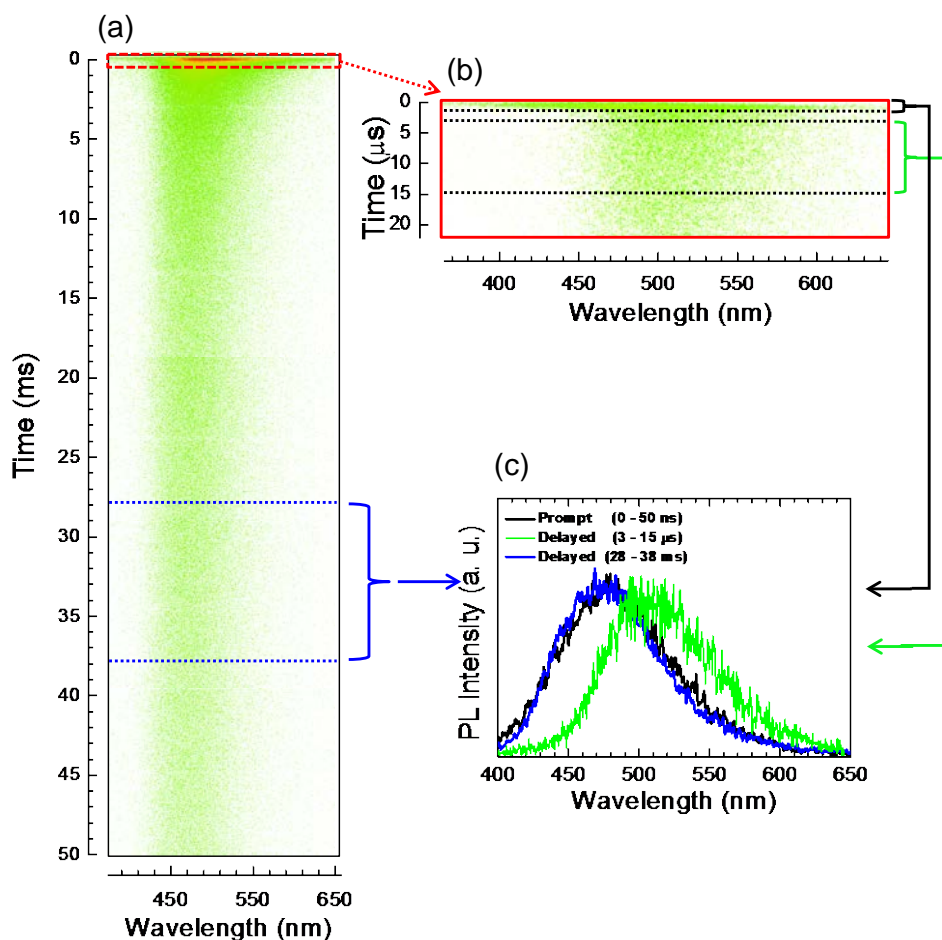


Figure 4.11 (a) Streak image of the decay in 2wt% ACRF doped into a DPEPO host. (b) Streak image of the same film on 20 μs time scale. (c) Red shift (green line) and gradual blue shift (blue line) of the delayed emission compared to its prompt fluorescence spectrum (black line). The data were measured at room temperature (RT) under vacuum.

Table 4.4 Energy levels of host layers and ACRF doped into host layers at a concentration of 2wt%.

Hosts	$S_1^{H(a)}$ [eV]	$T_1^{H(a)}$ [eV]	$S_1^{G(a)}$ [eV]	$T_1^{G(a)}$ [eV]	$E_{RED}^{(a)}$ [eV]	$E_{BLUE}^{(a)}$ [eV]	$\Delta E_{ST}^{(b)}$ [eV]	$\Delta E_{STi}^{(b)}$ [eV]	$\Delta E_{STf}^{(b)}$ [eV]	TADF _e _45 [%]	$\mu_G^{(c)}$ [D]
TmPyPB	3.38	2.80	2.94	2.65	2.70	2.70	0.29	0.05	0.05	n/a ^f	n/a ^f
TPSi-F	4.08	2.84	3.03	2.65	2.92	2.92	0.38	0.27	0.27	37.5	0.11
T2T	3.21	2.86	3.06	2.82 ^d	2.77	2.77	n/a ^d	n/a ^d	n/a ^d	n/a ^f	n/a ^f
PYD2	3.48	3.03	3.03	2.66	2.75	2.79	0.37	0.09	0.13	56.0	2.33
CzSi	3.68	3.09	3.03	2.68	2.89	2.98	0.35	0.21	0.30	43.5	2.75
DPEPO	4.25	3.38	3.04	2.73	2.80	3.0	0.31	0.07	0.27	75.4	8.06

^{a)} Error bar ± 0.02 . ^{b)} Error bar ± 0.04 . ^{c)} Calculated dipole moments in their ground states (Density functional theory (DFT) in Gaussian 09 at the B3LYP/6-31G(d) level). ^{d)} Cannot be determined in a doped T2T film due to the simultaneous phosphorescence of ACRF and T2T molecules at low temperature. ^{e)} Fraction of TADF component within the first 45 μ s. ^{f)} No values considered due to exciplex formation.

To explain this phenomenon, we introduce a time dependence into the singlet-triplet energy gap by defining $\Delta E_{ST}(t) = E(t) - T_1^G$, where $E(t)$ is the onset energy of the emission at time t . The singlet-triplet energy gap after the initial red shift, ΔE_{STi} , is then calculated using $E(t) = E_{RED}$. Similarly, the gap at the time of the final, maximally blue-shifted emission, ΔE_{STf} , is calculated using $E(t) = E_{BLUE}$ (Table 4.4). As shown in Figs. 4.12b and 4.12c for the first 45 μ s of PL, a decrease in ΔE_{STi} is accompanied by an increase in the fraction of TADF emission. From this relationship, we deduce that the initial RISC process is determined by ΔE_{STi} and not by $\Delta E_{ST} = S_1^G - T_1^G$.

In addition to the host-guest films with low ΔE_{STi} values, high Φ_{PL} was also achieved for the doped CzSi and TPSi-F films, despite having $\Delta E_{STi} > 100$ meV. Although the upconversion process is less efficient in these two cases in the initial stage (Figs. 4.12b and 4.12c), their ΔE_{STf} values are lower than their ΔE_{ST} , allowing an overall high Φ_{RISC} over the long ms-order decay. Thus, even though ISC efficiency (Table 4.5) and apparent ΔE_{ST} are large in all of the cases, a high Φ_{PL} of $\sim 70\%$ is achievable due to the presence of a smaller virtual ΔE_{STi} and ΔE_{STf} .

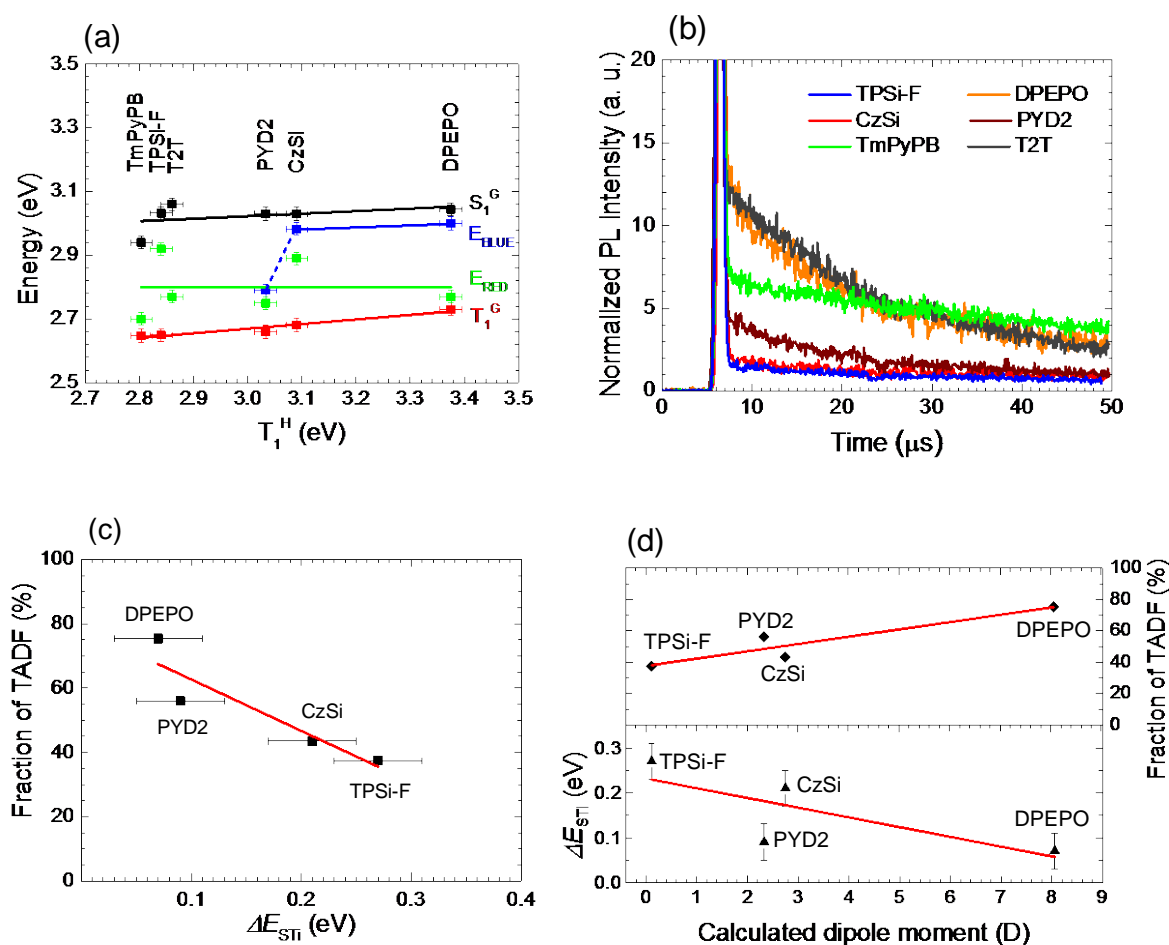
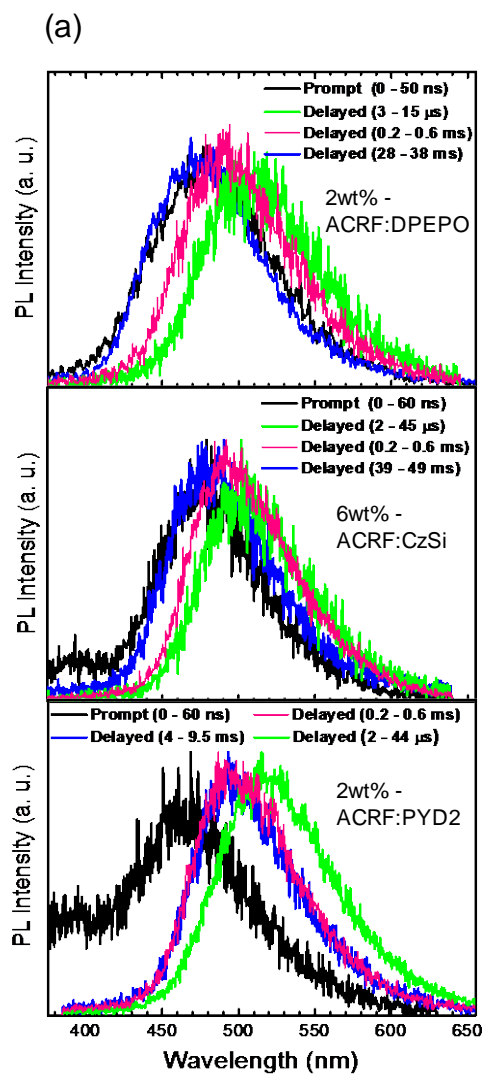


Figure 4.12 (a) Experimentally obtained S_1^G (black symbols), T_1^G (red symbols), and energy levels of red-shifted TADF E_{RED} (green symbols) and blue-shifted TADF E_{BLUE} (blue symbols) for ACRF doped into various hosts at a concentration of 2wt% as a function of T_1^H . Solid lines represent linear fittings. (b) Transient decay curves of ACRF doped into various host layers where the initial prompt emission intensity was normalized to 100. The transients were measured at room temperature under vacuum. (c) Fraction of delayed emission as a function of ΔE_{STI} . (d) ΔE_{STI} and fraction of TADF as a function of the dipole moments of the host layers.

Though initial RISC is controlled by the rather small ΔE_{STI} , the time-dependent $\Delta E_{ST}(t)$ is expected to increase with time because of the blue shift of the PL spectra, as shown in Figs. 4.14 and 4.13a. This increase of ΔE_{ST} could gradually lower the rate of upconversion, potentially leading to very long emission decay. Thus, the concept of time-

dependent $\Delta E_{ST}(t)$ can be used to explain both the large fraction of TADF emission and the long lifetime.



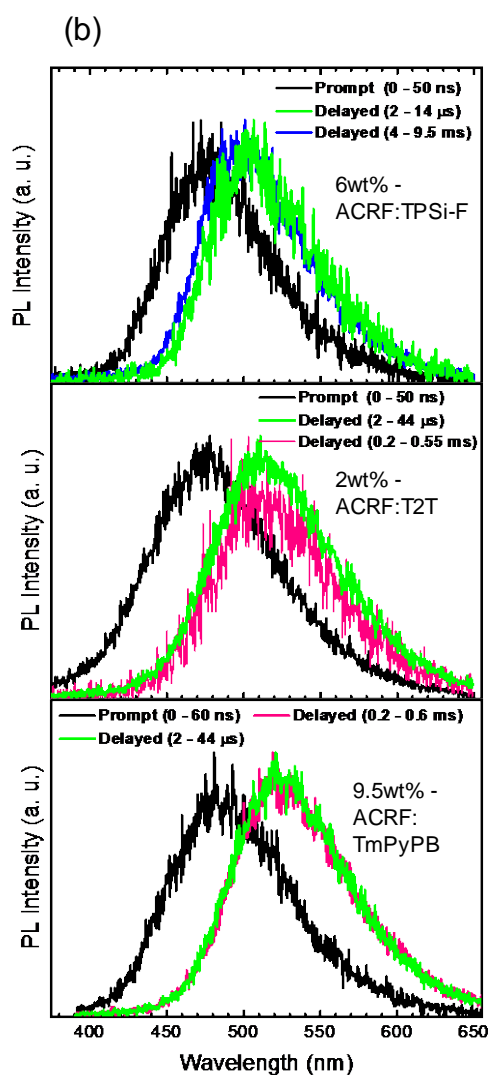


Figure 4.13 (a) Time dependent PL spectra of guest-host films showing strong blue shift and (b) weak blue shift.

Table 4.5 PL and EL characteristics of ACRF.

Hosts	$\Phi_{\text{PL}}^{\text{a)}$ [%]	$\Phi_{\text{F}}^{\text{a)}$ [%]	$\Phi_{\text{TADF}}^{\text{a)}$ [%]	$\Phi_{\text{SC}}^{\text{a)}$ [%]	$\Phi_{\text{RISC}}^{\text{a)}$ [%]	η_{int} [%]
TmPyPB	47.8±2.0	7.2±0.6	40.6±2.3	92.8±0.6	43.8±2.5	44.8±1.9
TPSi-F	68.5±2.1	5.3±1.6	63.2±1.9	94.7±1.6	66.7±2.3	67.2±1.9
T2T	14.4±0.9	3.0±0.3	11.4±1.0	97.0±0.3	11.7±1.0	12.4±0.8
PYD2	69.2±0.7	6.0±1.8	63.2±0.6	94.0±1.8	67.2±1.5	67.7±1.3
CzSi	61.3±2.0	3.2±1.0	58.1±6.6	96.8±1.0	60.0±6.8	60.3±5.4
DPEPO	68.8±2.8	4.9±1.5	63.9±8.6	95.1±1.5	67.2±9.1	67.6±7.2

^{a)} Time ranges used for the PL experiments for each host were: 0.5 ms (TmPyPB, T2T), 40 ms (TPSi-F), 30 ms (PYD2) and 50 ms (CzSi, DPEPO).

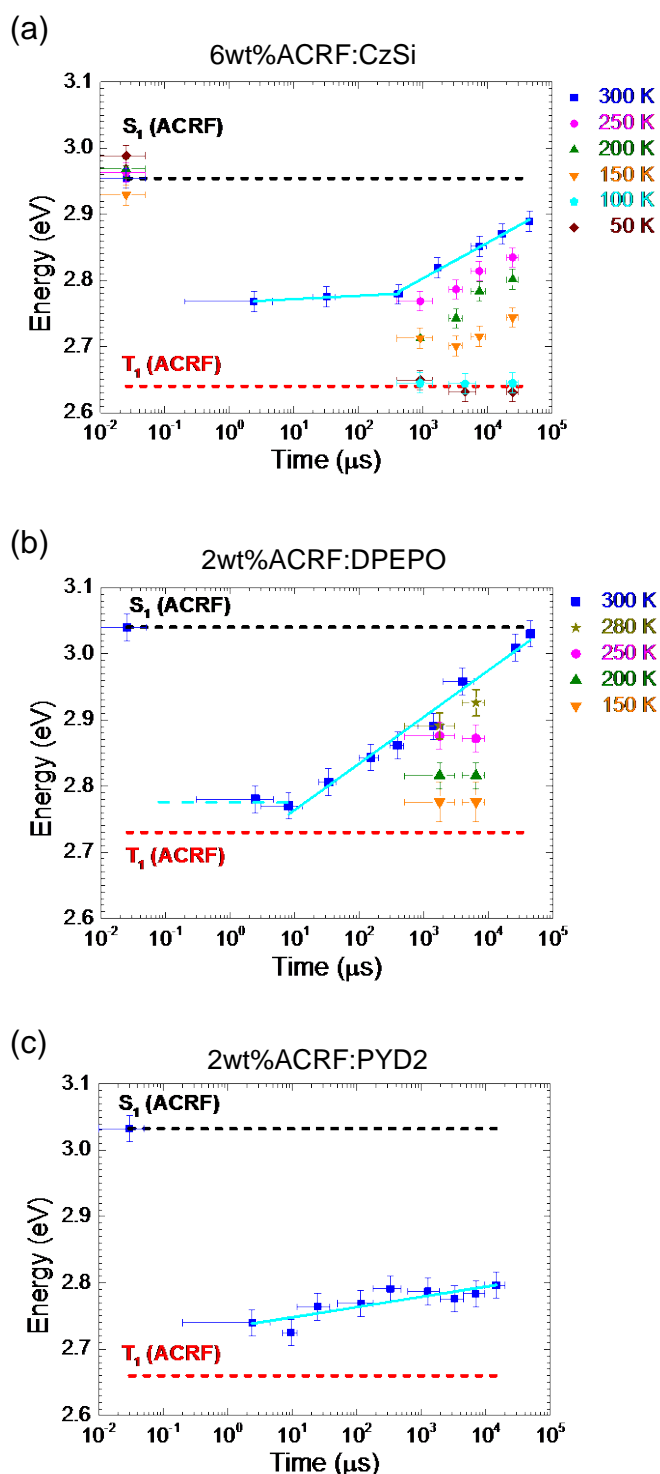


Figure 4.14 Time dependence of the energy level of fluorescence and delayed emission for ACRF doped into a) CzSi, b) DPEPO, and c) PYD2 host layers at various temperatures.

4.2.3.2 Mechanism of the Dynamic Change in ΔE_{ST}

Spectral red shift of charge transfer (CT) emission is a well-known phenomenon observed for emitters dissolved in solvents of high polarity (solvation-effect) and is also seen in TADF molecules [3b], including ACRF (Fig. 4.15). Moreover, solvatochromic shifts in solid-state emitters have also been reported, where the shift is induced by increasing the dipole moment of the host layer [20] or by increasing the concentration of the guest [21]. Similarly, a red shift in emission from TADF molecules in solid-state films has been associated with the polarization of the host medium, which affects the nuclear configurations of the host-guest system during electrical transitions [22,23]. In the case of ACRF:host layers, as shown in Fig. 4.12d and Table 4.4, lower E_{RED} and ΔE_{STi} can be linked to a higher dipole moment for the host. Thus, the change of polarization in various host media should be key to understanding the spectral shifts.

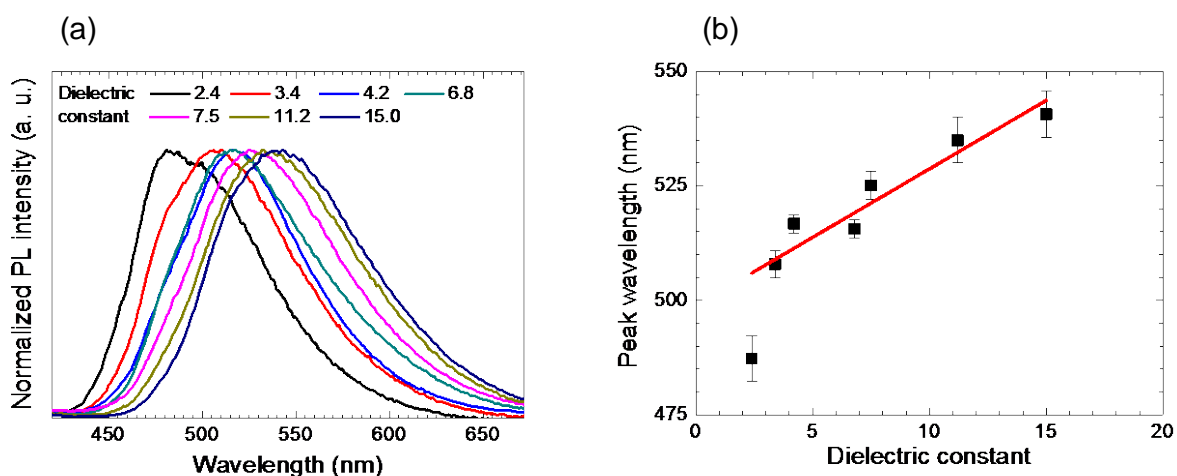


Figure 4.15 (a) PL spectra of ACRF in acetone:acetonitrile binary solutions having different dielectric constants. (b) Dependence of the peak wavelength of the PL spectra on the dielectric constant of the solutions.

The red and blue shifts over time can be explained based on interaction with the dipoles of the host layer using the energy level system proposed by Zhang *et al.*, in which a $^3CT^*$ level that lies close to the lowest $^3\pi-\pi^*$ localized excited (LE) energy level is present

in TADF emitters [3b] (Fig. 4.16). It has been shown that the $^3\text{CT}^*$ state, compared to the $^3\pi\text{-}\pi^*$ state, has strong dipolar interactions with its surrounding. This is because CT-type phosphorescence spectra tend to red shift with an increase in the polarity of solvents, while $\pi\text{-}\pi^*$ -type phosphorescence is independent of the polarity of host solvents [3b]. This is similar to the guest studied here.

Although the lowest lying triplet in ACRF is a $^3\pi\text{-}\pi^*$ state based on the observed $\pi\text{-}\pi^*$ -type phosphorescence spectrum (Fig. 4.2), we assume that a $^3\text{CT}^*$ state is lying between the $^1\text{CT}^*$ and $^3\pi\text{-}\pi^*$ states of ACRF. As shown in Fig. 4.16, to promote TADF emission, $^3\pi\text{-}\pi^*$ triplets in ACRF should first be converted to $^3\text{CT}^*$ triplets through a thermally-assisted reverse internal conversion (RIC) before RISC ($^3\text{CT}^* \rightarrow ^1\text{CT}^*$). Similar processes have been discussed recently in the literature [24]. In the excited state, ACRF has a relatively high dipole moment of $\mu_E = 14.1$ D compared to its ground state dipole moment of $\mu_G = 1.47$ D (computed by Gaussian). A high population of excitons in the $^3\text{CT}^*$ states of ACRF would lead to a strong interaction between the dipole fields of ACRF and the host, causing the alignment of the dipoles of the host molecules and, in turn, resulting in the red-shifted TADF spectrum. Then, as the population of $^3\text{CT}^*$ states decreases through delayed fluorescence, the dipoles of the host molecules gradually randomize, starting the blue shift (Fig. 4.16).

As shown in Fig. 4.14, the blue shift was suppressed at low temperatures in the cases of CzSi and DPEPO. Therefore, we conclude that this phenomenon is associated with a ms-order slow motion of the guest and host molecules. The mobility of the molecules would be suppressed at low temperatures preventing the gradual randomization of the dipoles of host molecules. On the other hand, the rigid structures of TmPyPB, T2T, and PYD2 host molecules [25,26] would provide a tightly-packed molecular environment for ACRF molecules, retarding their motion at room temperature. This tight packing by the host molecules would explain the lack of blue shift in these films as shown in Figs. 4.13b and 4.17. Such a reduced motion preventing the blue shift is consistent with the idea of delayed randomization of the dipoles in these films. Finally, the almost zero dipole moment of TPSi-F molecules (Table 4.4) could explain both the lack of blue shift and the rather small red shift of its delayed emission compared to the other doped films. In addition, we note that while we could find a clear relationship between the dipole moment of the

host and the fraction of TADF on μs time scale (Fig. 4.12d, Table 4.4), a connection between the dipole moment and τ_{del} (Table 4.2) was not evident.

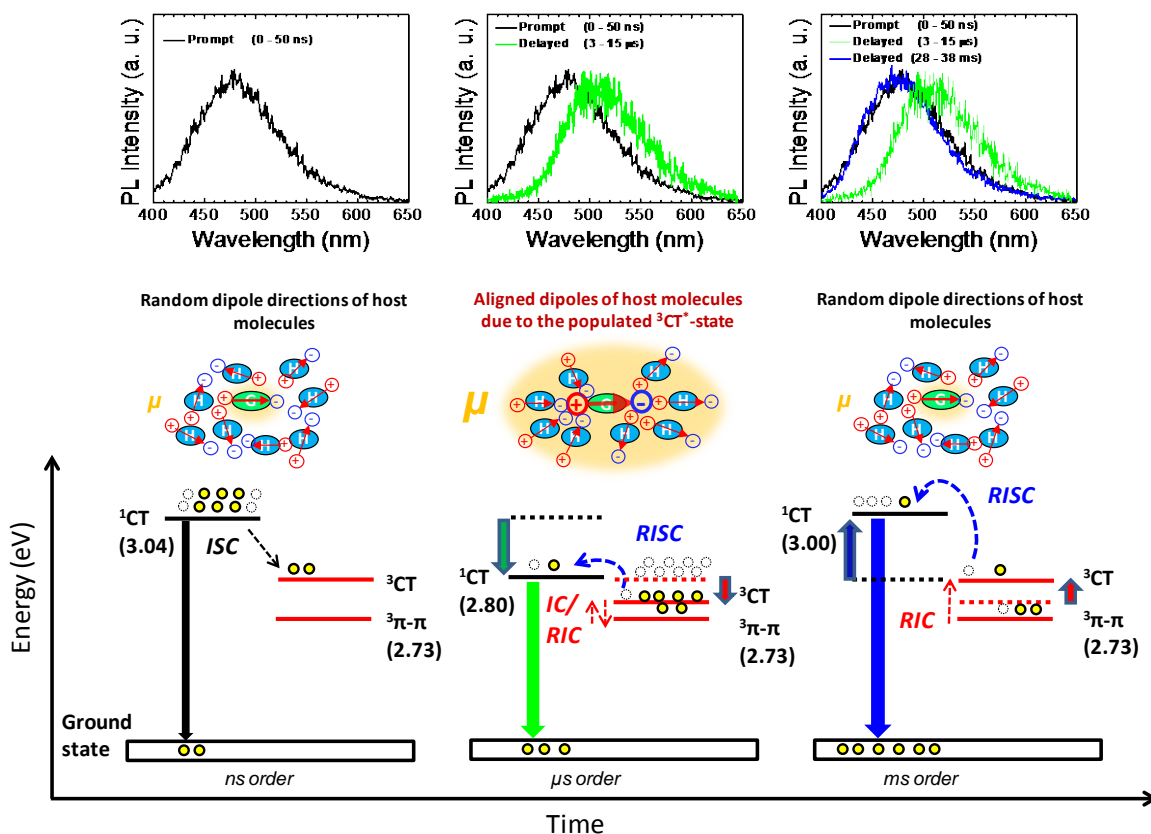


Figure 4.16 Schematic mechanism of the red and blue shifts in PL spectra in a 2wt% ACRF:DPEPO film. H and G refer to host and guest molecules, respectively. The red arrows illustrate permanent dipole vectors, and the orange spheres and μ represent the strength of the dipole field of ACRF. The red, blue, and green arrows represent energy level shifts, and IC and RIC stand for internal and reverse internal conversion, respectively, between the triplet levels.

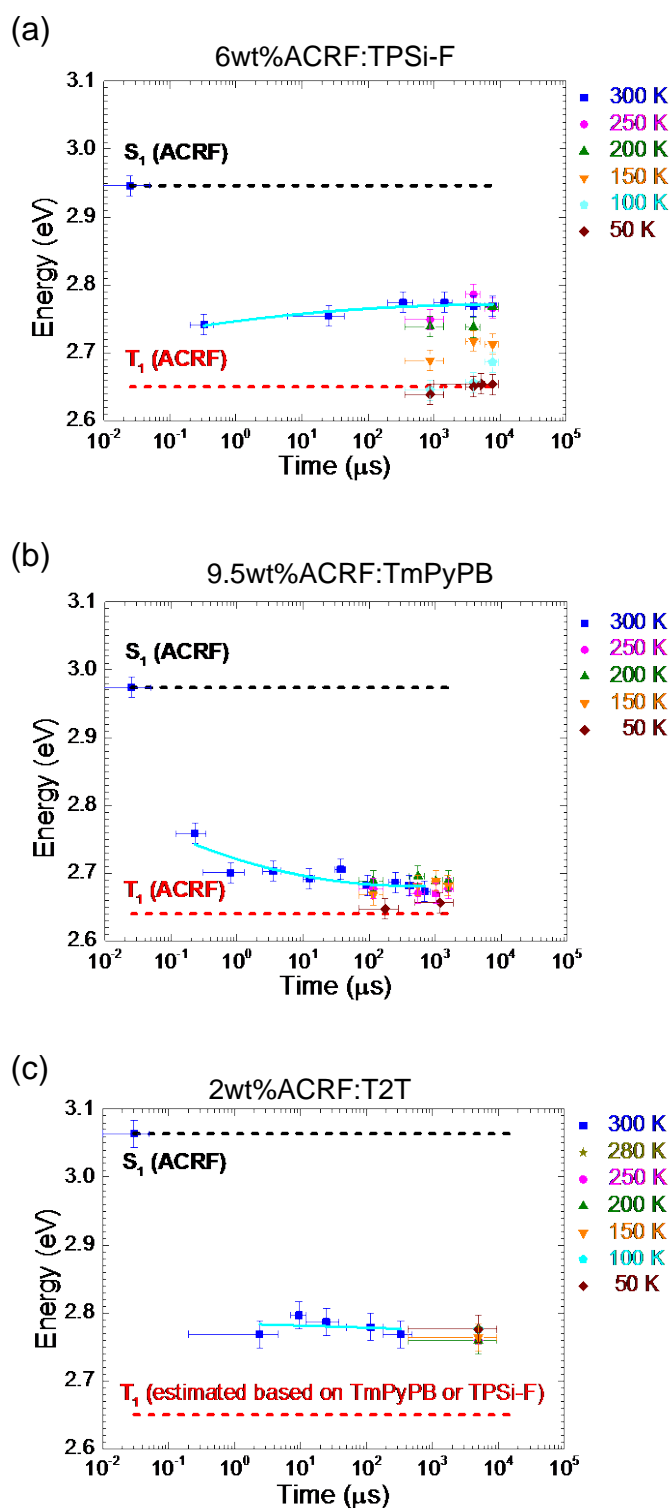


Figure 4.17 Time dependence of the energy levels of fluorescence and delayed emission of ACRF doped into a) TPSi-F, b) TmPyPB, and c) T2T host layers at various temperatures.

4.2.4 Electroluminescence Characteristics of ACRF:Host Layers

Most important for device applications is how the differences in the PL characteristics of the ACRF:host films affect the performance of OLEDs using the films and if highly efficient electroluminescence (EL) can be achieved from the triplet excitons through TADF. The most important measurement of OLED performance is the external EL quantum efficiency (η_{ext}), which is the ratio of the number of emitted photons to the number of injected electrons. The η_{ext} should be greatly affected by the efficiency of RISC and TADF while at the same time depending on additional factors related to the electrical excitation of the films.

To study this, we fabricated multilayer devices with the following structure: indium tin oxide (ITO; 110 nm)/*N,N'*-bis(naphthalen-1-yl)-*N,N'*-bis(phenyl)-2,2'-dimethylbenzidine (α -NPD; 35 nm)/1,3-bis(9-carbazolyl)benzene (mCP; 5 nm)/6wt% ACRF:host (20 nm)/1,3,5-tri(*m*-pyrid-3-yl-phenyl)benzene (TmPyPB; 40 nm)/lithium-fluoride (LiF; 1 nm)/aluminum (Al; 70 nm). The relationship between η_{ext} and injected current density is shown in Fig. 4.18a. Except for T2T with its low Φ_{PL} , all of the ACRF:host combinations exhibit an η_{ext} greater than the 5% maximum expected when triplet excitons do not contribute to the EL. Furthermore, similar η_{ext} can be obtained in cases of both long and short delayed emission.

The theoretical maximum external quantum efficiency ($\eta_{\text{ext(t)}}$) can be estimated from the PL characteristics as follows [3c, 9b]:

$$\eta_{\text{ext(t)}} = \eta_{\text{int}} \times \eta_{\text{p}} = [\eta_{\text{r}}(\text{S}_1)\Phi_{\text{F}} + \eta_{\text{r}}(\text{S}_1)\Phi_{\text{TADF}} + \eta_{\text{r}}(\text{T}_1)\Phi_{\text{TADF}} / \Phi_{\text{ISC}}] \times \gamma \times \eta_{\text{p}}, \quad (\text{Eq. 4.1})$$

where η_{int} is the internal EL efficiency, η_{p} is the photon outcoupling efficiency, $\eta_{\text{r}}(\text{S}_1)$ is the radiative singlet-exciton production efficiency (25%), $\eta_{\text{r}}(\text{T}_1)$ is the radiative triplet-exciton production efficiency (75%), Φ_{F} is the prompt component of Φ_{PL} (attributed to prompt fluorescence), Φ_{TADF} is the delayed component of Φ_{PL} (attributed to TADF), Φ_{ISC} is the ISC efficiency, and γ is the charge balance factor. The Φ_{ISC} is estimated by neglecting the non-radiative decay from a singlet excited state. The $\eta_{\text{ext(t)}}$ calculated by assuming $\eta_{\text{p}} = 20\%$ and $\gamma = 1$ are listed in Table 4.2. The calculated $\eta_{\text{ext(t)}}$ are in good agreement with the maximum η_{ext} for the devices with DPEPO, TmPyPB, and T2T as host. On the other hand, η_{ext} is much lower than $\eta_{\text{ext(t)}}$ for the devices with PYD2, CzSi and TPSi-F as host.

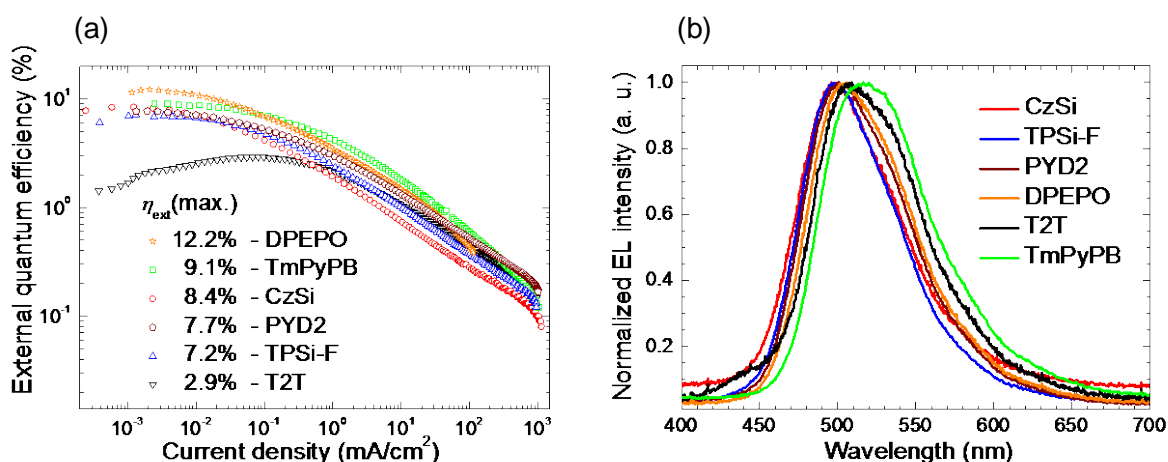


Figure 4.18 (a) External quantum efficiency (η_{ext}) as a function of the injected current density in OLEDs. (b) EL spectra of OLEDs with ACRF as an emitter doped into various host layers taken at a current density of 10 mA/cm².

To understand these differences in OLED performance that are not simply explained by the PL properties, we consider electrical properties of the devices using the energy diagrams shown in Fig. 4.19. Although several factors can alter η_{ext} , we mainly consider the effect of carrier trapping by the guest in these host layers, since all other parameters and measurement conditions are identical for all devices. Carrier trapping by guest molecules has been shown to lead to efficient EL by increasing the number of emissive recombinations of electron-hole pairs [27]. Carrier trapping requires the guest to have its LUMO level below and/or its HOMO level above that of the host.

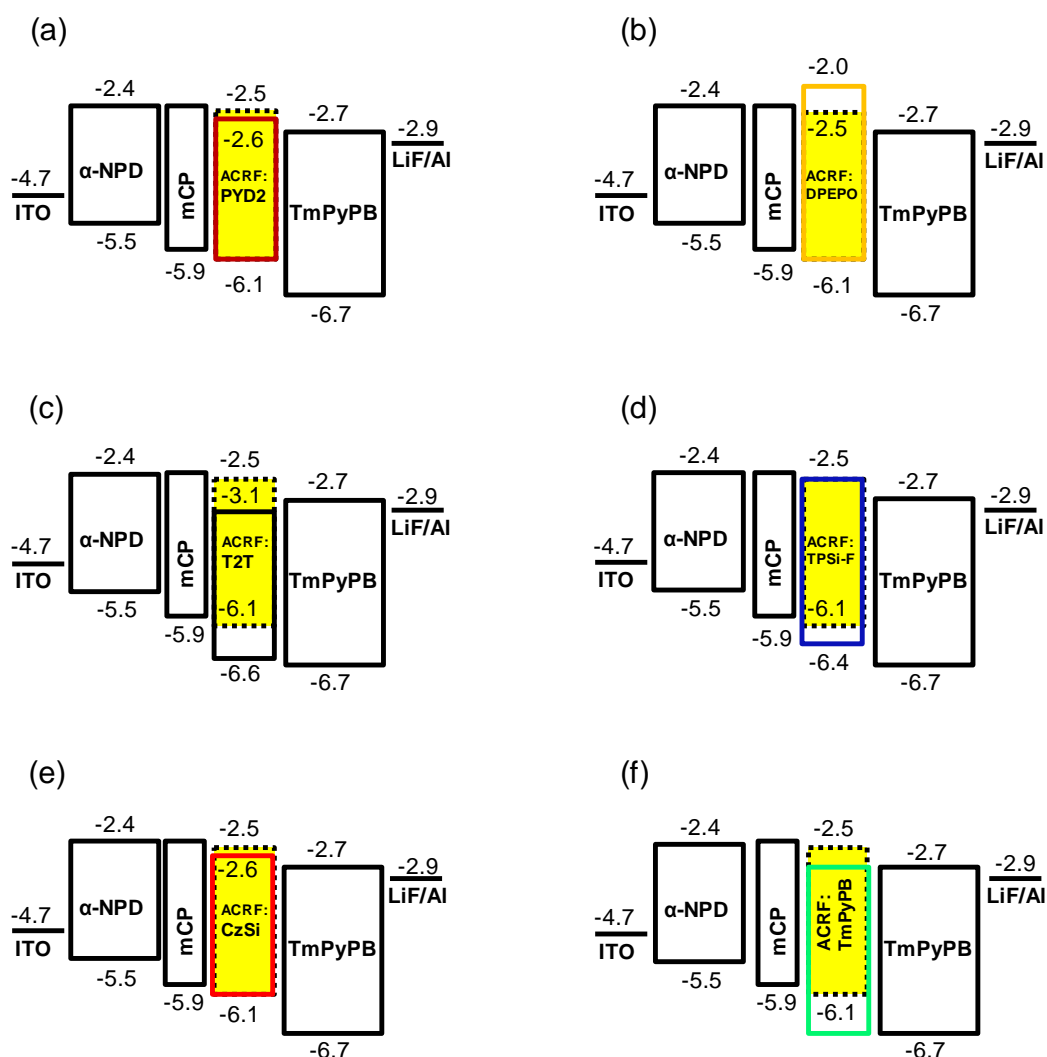


Figure 4.19 Energy diagrams of materials used in OLEDs.

Based on the criteria of charge trapping, ACRF in PYD2 and CzSi would be a poor charge trap while ACRF in DPEPO would be a good electron trap, explaining the low and high η_{ext} in these devices with high $\eta_{\text{ext}(t)}$ (Fig. 4.19 and Table 4.2). On the other hand, the lower η_{ext} of a TPSi-F-based device would be mainly due to the unbalanced carrier transport despite of its relatively good hole trapping ability, since we achieved $\eta_{\text{ext}} = 10\%$ in OLEDs using an ACRF:TPSi-F emitting layer in our previous study using different hole transport layers [8]. In OLEDs with TmPyPB and T2T hosts, the observed maximum η_{ext} is reasonable based on the calculated $\eta_{\text{ext}(t)}$ even though the LUMO level of the guest molecule is above that of these hosts. This is probably due to the enhancement of carrier

recombination through exciplex formation between the guest and the host. In fact, the EL spectra were slightly red-shifted for the TmPyPB- and T2T-based devices, indicating the exciplex emission (Fig. 4.18b). Thus, in addition to the PL properties, electrical considerations are also important when choosing the host for OLEDs. The dependence of current density and luminance from the applied voltage of the fabricated devices can be seen in Fig. 4.20.

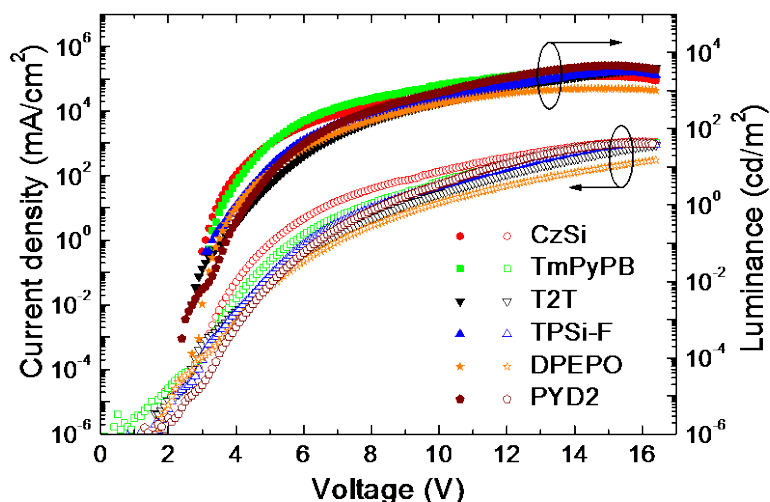


Figure 4.20 Current density and luminance characteristics of OLEDs.

4.3 Conclusions

In this study, we clarified how the selection of small-molecule hosts can affect the unique PL characteristics of the TADF molecule ACRF in solid-state films. We observed that the lifetime of the triplet excited state can be significantly influenced by the host molecules. Depending on the choice of host, ACRF displayed a TADF component with a transient lifetime ranging from ~4 ms to ~70 ms in oxygen-free environment while maintaining a high Φ_{PL} . We found that the long lifetime could not be explained by other known processes such as a mutual energy transfer between the host and guest. For high Φ_{PL} and ultimately high η_{ext} , the formation of exciplexes must be considered and avoided in addition to the use of host layers with a high T_1 level to confine triplet excitons.

We analyzed the mechanism of long TADF decay time in detail. After an initial red shift of the TADF spectrum, it gradually blue-shifted over several tens of ms until the

emission was identical to that of the prompt fluorescence spectrum. We propose that this phenomenon is due to the gradual shift of CT singlet and triplet excited states that lead to a time-dependent energy gap between the lowest singlet and triplet states. We conclude that the red and blue shifts of the TADF spectrum result from dipole interactions between the guest and host molecules.

Furthermore, we showed that harvesting of triplet excitons and similar η_{ext} could be obtained regardless of the delayed PL lifetime in OLED devices. In addition to the PL characteristics, charge trapping and transport must be considered when choosing a host and designing the surrounding layers to obtain η_{ext} close to the theoretical maximum. Based on the phenomena studied here, tuning of the emission properties and lifetime based on the host could be used to tailor device characteristics to specific applications. For example, short lifetime TADF would be applied to OLEDs, and long emission could find novel applications in the areas outside of OLEDs, such as high-sensitivity oxygen sensors. While these results are applicable to small-molecule hosts, additional studies with polymer matrix hosts and more detailed solution studies are necessary to completely clarify the emission processes in ACRF.

4.4 References

- [1] S. A. Carlson, D. M. Hercules, *J. Am. Chem. Soc.* **93** (1971) 5611.
- [2] H. Uoyama, K. Goushi, K. Shizu, H. Nomura, C. Adachi, *Nature* **492** (2012) 234.
- [3] a) K. Goushi, C. Adachi, *Appl. Phys. Lett.* **101** (2012) 023306; b) Q. Zhang, J. Li, K. Shizu, S. Huang, S. Hirata, H. Miyazaki, C. Adachi, *J. Am. Chem. Soc.* **134** (2012) 14706; c) S. Y. Lee, T. Yasuda, H. Nomura, C. Adachi, *Appl. Phys. Lett.* **101** (2012) 093306; d) H. Tanaka, K. Shizu, H. Miyazaki, C. Adachi, *Chem. Commun.* **48** (2012) 11392; e) J. Li, T. Nakagawa, Q. Zhang, H. Nomura, H. Miyazaki, C. Adachi, *Adv. Mater.* **25** (2013) 3319; f) J. Lee, K. Shizu, H. Tanaka, H. Nomura, T. Yasuda, C. Adachi, *J. Mater. Chem. C* **1** (2013) 4599; g) K. Sato, K. Shizu, K. Yoshimura, A. Kawada, H. Miyazaki, C. Adachi, *Phys. Rev. Lett.* **110** (2013) 247401.

- [4] a) J. R. Lakowicz, *Principles of Fluorescence Spectroscopy*, 3rd ed., Springer, Heidelberg (2006); b) Y. Kawamura, J. Brooks, J. J. Brown, H. Sasabe, C. Adachi, *Phys. Rev. Lett.* **96** (2006) 017404.
- [5] a) K. Goushi, R. Kwong, J. J. Brown, H. Sasabe, C. Adachi, *J. Appl. Phys.* **95** (2004) 7798; b) Y. Kawamura, K. Goushi, J. Brooks, J. J. Brown, H. Sasabe, C. Adachi, *Appl. Phys. Lett.* **86** (2005) 071104.
- [6] a) H. Sasabe, J. Kido, *Chem. Mater.* **23** (2011) 621; b) A. Chaskar, H.-F. Chen, K.-T. Wong, *Adv. Mater.* **23** (2011) 3876; c) L. Xiao, Z. Chen, B. Qu, J. Luo, S. Kong, Q. Gong, J. Kido, *Adv. Mater.* **23** (2011) 926; d) Y. Tao, C. Yang, J. Qin, *Chem. Soc. Rev.* **40** (2011) 2943.
- [7] a) Y. J. Cho, K. S. Yook, J. Y. Lee, *Adv. Mater.* (2014) DOI: 10.1002/adma.201400347; b) B. S. Kim, B. Y. Lee, *Adv. Funct. Mater.* (2014) DOI: 10.1002/adfm.201303730; c) Y. Im, J. Y. Lee, *Chem. Mater.* **26** (2014) 1413.
- [8] G. Méhes, H. Nomura, Q. Zhang, T. Nakagawa, C. Adachi, *Angew. Chem. Int. Ed.* **51** (2012) 11311.
- [9] a) C. Adachi, R. C. Kwong, P. Djurovich, V. Adamovich, M. A. Baldo, M. E. Thompson, S. R. Forrest, *Appl. Phys. Lett.* **79** (2001) 2082; b) A. Endo, K. Sato, K. Yoshimura, T. Kai, A. Kawada, H. Miyazaki, C. Adachi, *Appl. Phys. Lett.* **98** (2011) 083302; c) F.-C. Chen, G. He, Y. Yang, *Appl. Phys. Lett.* **82** (2003) 1006.
- [10] S.-J. Su, T. Chiba, T. Takeda, J. Kido, *Adv. Mater.* **20** (2008) 2125.
- [11] H.-F. Chen, S.-J. Yang, Z.-H. Tsai, W.-Y. Hung, T.-C. Wang, K.-T. Wong, *J. Mater. Chem.* **19** (2009) 8112.
- [12] K. S. Son, M. Yahiro, T. Imai, H. Yoshizaki, C. Adachi, *J. Photopolym. Sci. Technol.* **20** (2007) 47.
- [13] M.-H. Tsai, T.-H. Ke, H.-W. Lin, C.-C. Wu, S.-F. Chiu, F.-C. Fang, Y.-L. Liao, K.-T. Wong, Y.-H. Chen, C.-I. Wu, *ACS. Appl. Mater. Interfaces* **1** (2009) 567.
- [14] C. Han, Y. Zhao, H. Xu, J. Chen, Z. Deng, D. Ma, Q. Li, P. Yan, *Chem. Eur. J.* **17** (2011) 5800.

- [15] The observation window excludes the host peaks to compare only the guest emissions.
- [16] In Fig. 4.9 we show the absorption spectra of host neat films and of 2- or 6wt%-codeposited films. We selected λ_{exc} for each host-guest film in the high absorption region of host layers (Fig. 4.8, Table 4.2).
- [17] D. Virgili, M. Cocchi, V. Fattori, C. Sabatini, J. Kalinowski, J. A. G. Williams, *Chem. Phys. Lett.* **433** (2006) 145.
- [18] a) N. Matsumoto, M. Nishiyama, C. Adachi, *J. Phys. Chem. C* **112** (2008) 7735; b) N. Matsumoto, C. Adachi, *J. Phys. Chem. C* **114** (2010) 4652; c) V. Jankus, C.-J. Chiang, F. Dias, A. P. Monkman, *Adv. Mater.* **25** (2013) 1455.
- [19] Q. Zhang, T. Komino, S. Huang, S. Matsunami, K. Goushi, C. Adachi, *Adv. Funct. Mater.* **22** (2012) 2327.
- [20] C. F. Madigan, V. Bulović, *Phys. Rev. Lett.* **91** (2003) 247403.
- [21] G. Zhang, S. E. Kooi, J. N. Demas, C. L. Fraser, *Adv. Mater.* **20** (2008) 2099.
- [22] K. Goushi, K. Yoshida, K. Sato, C. Adachi, *Nat. Photon.* **6** (2012) 253.
- [23] K. Nasu, T. Nakagawa, C.-J. Lin, C.-H. Cheng, M.-R. Tseng, T. Yasuda, C. Adachi, *Chem. Commun.* **49** (2013) 10385.
- [24] a) F. B. Dias, K. N. Bourdakos, V. Jankus, K. C. Moss, K. T. Kamtekar, V. Bhalla, J. Santos, M. R. Bryce, A. P. Monkman, *Adv. Mater.* **25** (2013) 3707. b) Q. Zhang, B. Li, S. Huang, H. Nomura, H. Tanaka, C. Adachi, *Nat. Photon.* **8** (2014) 326.
- [25] W. Ren, H. Zhuang, Q. Bao, S. Miao, H. Li, J. Lu, L. Wang, *Dyes Pigments* **100** (2014) 127.
- [26] F. Jean-Baptiste Dit Dominique, H. Gornitzka, A. Sournia-Saquet, C. Hemmert, *Dalton Trans.* **2** (2009) 340.
- [27] R. J. Holmes, B. W. D'Andrade, X. Ren, J. Li, M. E. Thompson, S. R. Forrest, *Appl. Phys. Lett.* **83** (2003) 3818.

Chapter 5

Sensing of Dioxygen based on Thermally-Activated Delayed Fluorescence

5.1 Mechanism of Oxygen Quenching in ACRF

Outside the application in OLEDs, TADF emission of ACRF could be utilized in the field of oxygen sensing, as suggested in Chapters 3 and 4. The millisecond order TADF signal is strongly quenched in air, *i. e.*, Φ_{PL} of a 6wt% ACRF:TPSi-F film measured in nitrogen rich environment (~67%) largely decreases when measured in air (~11%) as presented in Chapter 3. This effect can be clearly demonstrated simply by flowing nitrogen gas over a sample in air under UV irradiation (Fig. 5.1). The quenching of TADF emission is a result of collisions between ACRF and dioxygen molecules.

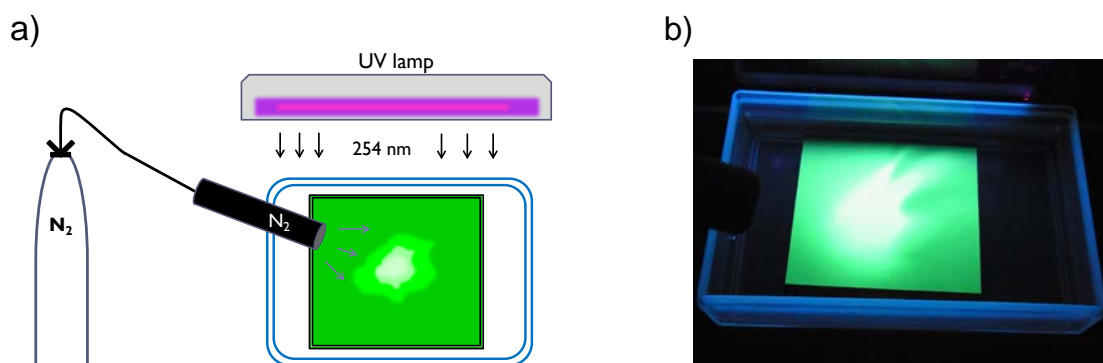


Figure 5.1 Nitrogen flow experiment. a) Schematic diagram of experimental setup, and b) photograph demonstrating enhanced TADF in a co-deposited film (6wt% ACRF:TPSi-F) on a square-shaped Si substrate (side length 45 mm) by temporarily removing oxygen from the film surface by directing a nitrogen gas flow over the sample under constant UV irradiation (254 nm).

The mechanism of photoluminescence of a 6wt% ACRF:TPSi-F film under nitrogen gas flow leading to an enhanced TADF emission in air is illustrated in Fig. 5.2. Excitation of a sample to higher singlet levels, S_n , is followed by internal conversion (IC) to the S_1 level (2.68 eV). From this point, while some of the energy relaxes through low-efficiency fluorescence (around 7% of the total emission), most of the excitons decay to the T_1 state (2.58 eV) by intersystem crossing (ISC). This process is followed by thermal upconversion to the S_1 state (RISC), thereby leading to TADF. Because the thermal recycling process between T_1 and S_1 continues for a relatively long time (>ms), in air it

leads to efficient nonradiative deactivation by energy exchange with dioxygen molecules in the environment. However, when oxygen is removed from the system by evacuation or under nitrogen flow, very efficient RISC from the T_1 to the S_1 levels leads to an intense delayed emission (comprising 93% of the total emission).

Based on the above described mechanism, ACRF can be a promising luminescent oxygen sensor when doped into suitable host layers with high permeability for dioxygen.

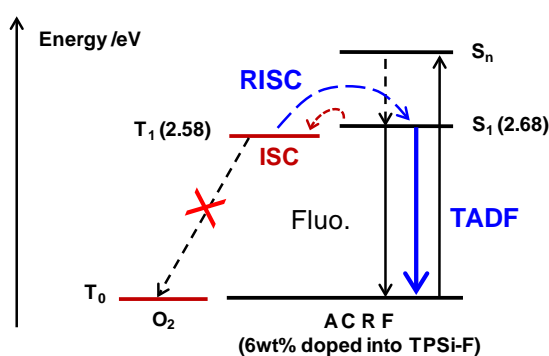


Figure 5.2 Energy diagram explaining enhanced TADF by elimination of oxygen quenching.

5.2 Oxygen Quenching in ACRF Doped into Polystyrene

Polystyrene (PS) was employed as a host layer for an oxygen sensor due to the optimal sensitivity of sensors doped into polystyrene to oxygen, high degree of sensor linearity, and other benefits [1]. A basic assessment of the oxygen sensitivity of a luminescent O_2 sensor can be done by calculating the oxygen quenching ratio $I_0 / I_x - 1$ or $\tau_0 / \tau_x - 1$ based on a Stern-Volmer equation for partial oxygen pressure (pO_2):

$$I_0 / I_x = \tau_0 / \tau_x = 1 + K_{SV} pO_2, \quad (Eq. 5.1)$$

where I_0 / I_x and τ_0 / τ_x are the ratios of the intensity and lifetime of emission at zero and non-zero dioxygen concentrations, respectively, and K_{SV} is the Stern-Volmer constant.

To understand the potential of ACRF as an oxygen sensor, its oxygen quenching ratio values are compared with those of known oxygen sensing molecules in Table 5.1. All

examples in this table use PS as a host layer, since different host materials result in different oxygen diffusion times into the bulk of the film, thus strongly influencing the sensitivity of the sensor to O₂. The PS-doped ACRF films show a large decrease in both Φ_{PL} and delayed emission in air compared to the unquenched PL signal in oxygen-free environment, as shown in Table 5.1 and Fig. 5.3. The oxygen quenching ratio of ACRF based on the decrease in Φ_{PL} is nearly identical in air and in 100% oxygen-rich environment and is similarly high to those of the highly sensitive luminescent oxygen sensors reported in the literature (Table 5.1). Moreover, a decrease in the lifetime of these 2wt% ACRF:PS films in air compared to that under vacuum gives an even higher value of oxygen quenching ratio (Table 5.1).

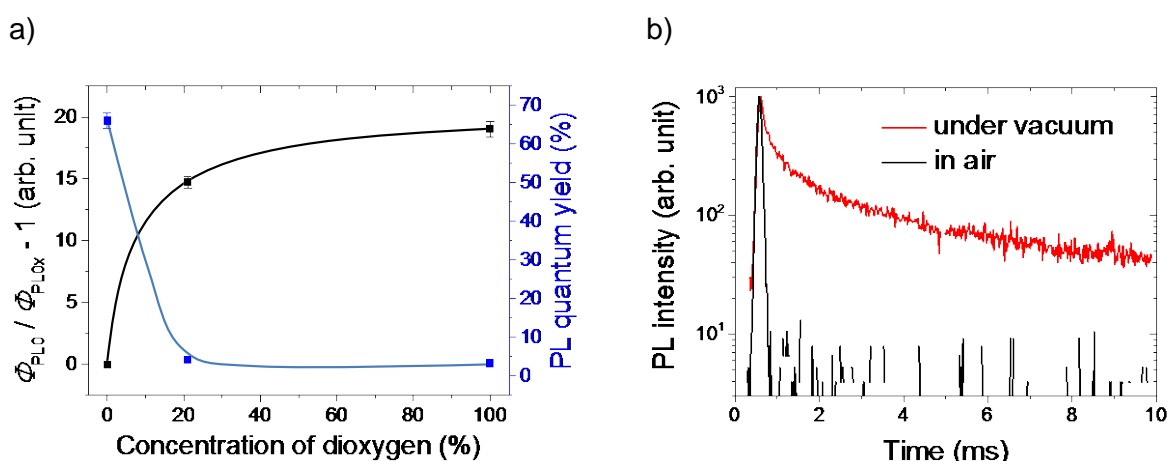


Figure 5.3 (a) Dependence of oxygen quenching ratio related to Φ_{PL} and of Φ_{PL} on concentration of dioxygen; (b) transient PL of a 2wt% ACRF:PS film measured by a streak camera under vacuum and in air.

We note that ACRF exhibits a multi-exponential decay behavior, as discussed in Chapter 4. This, in fact, leads to multiple possible oxygen quenching ratio values based on the way the delayed lifetime is determined. For example, the oxygen quenching ratio values in Table 5.1 based on lifetime were determined using $\tau_0 = 8.67$ ms and $\tau_{21} = 58.79$ or 14.67 μs . The values of τ_{21} are derived from either a longer low intensity third order (58.79 μs) or a shorter higher intensity second order decay component (14.67 μs) of the PL

signal measured on a 400 μ s time scale in air. In a similar way, τ_0 was determined from a PL transient decay signal under vacuum on a 10 ms time scale (Fig. 5.3). A longer lifetime value is expected when measured on a longer time scale due to the gradual blue shift effect, leading to an even higher quenching ratio by O₂.

Table 5.1 Comparison between oxygen quenching ratios of ACRF and reported oxygen sensors in polystyrene matrix

Sensor	Host	$I_0 / I_{100} - 1$	$\tau_0 / \tau_{100} - 1$	References
ACRF	PS	19.0 ^{a)}	146.5 ^{b)}	This work
	PS		590.0 ^{b)c)}	
PtOEP	PS	3.5	2.6 ^{b)}	[3,2]
Ir(ppy) ₃	PS	0.2	-	[3]
PtOEPK	PS	19		[3]
PdOEPK	PS	27	-	[3]
ZnTFPP	PS	-	46.3 ^{d)}	[3]
C ₆₀	PS	-	48.4 ^{d)}	[3]
C ₇₀	PS	-	432 ^{d)}	[3]

^{a)} Substituted by $\Phi_{PL0} / \Phi_{PL100} - 1$; ^{b)} Substituted by $\tau_0 / \tau_{21} - 1$; ^{c)} Estimated from a longer third order (146.5) and a shorter second order (590.0) delayed component; ^{d)} Based on the lifetime change of T–T absorption

5.3 Conclusions

In conclusion, TADF emitters based on donor-acceptor structures with long PL lifetime have a high potential for the application of oxygen sensing. Further studies with a precise control of the concentration of oxygen on ppm and ppb levels at various temperatures would reveal the full potential of ACRF and similar TADF molecules for oxygen sensing. A wide range of applications would be possible for TADF-based oxygen sensors by versatile molecular designs that allow for tuning of the length of delayed emission, absorption and emission spectra, and by using hosts with various oxygen permeabilities. Examples include beverage production, food packaging, medical imaging, pressure sensitive paints, and others [4]. Finally, for reliable operation, factors related to real-life applications of oxygen sensors, such as temperature-dependence of the PL of TADF, effect of moisture and water on the sensing compound and its degradation, and others must be taken into account.

5.4 References

- [1] T. C. O’Riordan, H. Voraberger, J. P. Kerry, D. B. Papkovsky, *Anal. Chim. Acta* **530** (2005) 135.
- [2] S. M. Grist, L. Chrostowski, K. C. Cheung, *Sensors* **10** (2010) 9286.
- [3] Y. Amao, *Microchim. Acta* **143** (2003) 1.
- [4] a) S. Nagl, C. Baleizão, S. M. Borisov, M. Schäferling, M. N. Berberan-Santos, O. S. Wolfbeis, *Angew. Chem. Int. Ed.* **46** (2007) 2317; b) M. Schäferling, *Angew. Chem. Int. Ed.* **51** (2012) 3532; c) S. Zhang, M. Hosaka, T. Yoshihara, K. Negishi, Y. Iida, S. Tobita, T. Takeuchi, *Cancer Res.* **70** (2010) 4490; d) S. Hirata, K. Totani, J. Zhang, T. Yamashita, H. Kaji, S. R. Marder, T. Watanabe, C. Adachi, *Adv. Funct. Mater.* **23** (2013) 3386.

Chapter 6

Summary and Conclusions

Since the demonstration of the first efficient OLED in 1987, OLEDs have been explored and developed as alternative light-emitting devices for lighting and displays. The first generation of emitting materials, fluorescent emitters, emit only from singlet states and suffer from low internal electroluminescence (EL) efficiency (η_{int}) because 75% of electrically generated excitons are non-emissive triplets. Phosphorescent materials, the second generation, could harvest triplets for light emission, resulting in 100% η_{int} , but require a heavy metal. A new generation of materials achieves high efficiency through thermally-activated delayed fluorescence (TADF). In this thesis, we studied the photoluminescent (PL) and EL properties of a new spiro-conjugated acridine derivative TADF emitter, ACRF, in detail.

In Chapter 3, the basic PL and EL properties of ACRF were characterized. Using a streak camera, a millisecond order-long delayed emission component from vacuum-deposited thin films of ACRF doped into a small molecule host layer at room temperature was found. Based on temperature-dependent PL analysis, the delayed component was clearly shown to be thermally activated, thus classifying this material as a TADF emitter. The TADF emission exhibits charge transfer (CT) between the donor and the acceptor moieties of ACRF, as indicated by the broad and unstructured spectral emission profile. Likewise, CT in ACRF was also predicted by quantum-chemical calculations based on density functional theory (DFT), which showed a good localization of the highest occupied molecular orbital (HOMO) and lowest unoccupied molecular orbital (LUMO) levels of ACRF on its donor and acceptor moieties, respectively. A high PL quantum yield (Φ_{PL}) of ~67% was measured in the same doped film. More than 90% of the total emission in ACRF comes from the TADF component thanks to a high intersystem crossing (ISC) yield (Φ_{ISC}) and efficient reverse ISC (RISC) process in this emitter.

Encouraged by our promising results from the PL study, multilayer OLED devices were fabricated by vacuum deposition technique and enhanced EL efficiencies were achieved when using ACRF as a green emitter. The maximum value of external quantum efficiency (η_{ext}) was ~10%, which is well above the theoretical limit for common fluorescent molecules (~5%). A high efficiency of radiative exciton generation efficiency (η_{r}) of 94%, resulting from efficient RISC, can explain the high η_{ext} for this metal-free TADF molecule. It is believed that optimized designs using the molecular backbone of ACRF will enhance the TADF performance. Such inexpensive, organic aromatic

compounds with high Φ_{PL} are attractive for OLEDs, indicating that TADF emitters may, in the future, replace the organometallic emitters widely used today.

To understand the dependence of TADF on the host layer in ACRF, the range of PL studies was broadened in Chapter 4 by blending this TADF emitter as a guest in several small molecule host layers with a variety of molecular structures and T_1 levels. By observing differences in the transient emission decay, Φ_{PL} , and transient emission spectra in the vacuum-deposited host-guest films, several interesting conclusions could be derived. First, an efficient TADF emitter consisting of an acceptor and a donor might undergo CT processes with a suitable host molecule resulting in exciplex formation. Quenching of the TADF emission due to such exciplexes formed between a TADF guest and a host needs to be considered in addition to the back-energy transfer from the guest to the host that depends on the T_1 levels of the two molecules. Second, with a complete confinement of excitons in ACRF, high Φ_{PL} values of ~60-70% and long delayed emission with lifetimes (τ_{del}) ranging from ~4 ms to ~70 ms were demonstrated.

Third, an unusual transient red shift of the TADF emission spectrum compared to that of the prompt fluorescence was revealed during the analysis of the origin of the long delayed emission. This red shift was followed by a gradual blue shift over a millisecond time order back to the original fluorescence spectrum. This phenomenon is thought to be the result of dipole-interactions between the guest and host molecules, leading to a transient change of the singlet-triplet energy gap (ΔE_{ST}) of ACRF. This increase of ΔE_{ST} with time, with the magnitude of the change varying from ~0.1 eV to ~0.3-0.4 eV depending on host, could be responsible for both the high τ_{del} and Φ_{PL} values. On the other hand, the blue shift was suppressed in host-guest films where τ_{del} of ACRF was rather short (~4 ms), indicating a smaller degree of dipole-interactions between these host molecules and ACRF. Fourth, when using the unquenched ACRF-doped films as emitter layers in OLEDs, η_{ext} values above that of the theoretical limit for fluorescent OLEDs were achieved. The high η_{ext} values prove that high η_{r} originating from the TADF emission can be obtained in host-guest films both with longer and shorter delayed components.

Although we achieved high EL efficiencies in OLEDs using ACRF-doped films as emitters, we encountered a significant efficiency roll-off at high current densities, regardless of the host materials used. In Chapter 3, we showed that the origin of this roll-

off is mainly triplet-triplet annihilation, which can be directly related to the transient decay time of the delayed emission. Therefore, future work could focus on suppressing the roll-off by shortening the lifetime, which could be achieved by a modification of the molecular structure of ACRF. Modifying the acceptor and donor moieties of the spiro-acridine core by groups having various degrees of electron withdrawing and accepting abilities would be an effective and affordable way. This approach could not only allow for a smaller ΔE_{ST} leading to shorter τ_{del} and reduced efficiency roll-off, but also be a means of tuning the emission spectrum of the molecule. The PL and EL properties of new spiro-acridine derivatives could be further enhanced by using various host environments, as shown in this work with small molecule host layers. For future directions in host-related studies, polymer matrixes and liquid hosts with various viscosities could be explored, which would extend the range of OLEDs from the mechanically rigid structures studied in this work to bendable and degradation-free devices.

In addition to using ACRF or its derivatives as highly-efficient emitters in OLEDs, luminescent oxygen sensors are envisioned as another promising application for TADF emitters with long delayed component. In Chapters 3 and 5 a strong quenching of the delayed fluorescence of ACRF by atmospheric oxygen was described. Based on this quenching, it is suggested that even longer emission decays, such as shown in Chapter 4, would lead to very high sensitivities to oxygen quenching when ACRF is doped into hosts with high S_1 and T_1 levels and high oxygen permeability. In fact, ACRF doped into polystyrene displays an oxygen quenching ratio, based on quenching of the PL intensity or lifetime of the delayed component, higher than that of many available luminescent molecules as described in Chapter 5. Each relevant parameter for oxygen sensing will need to be carefully adjusted depending on the concrete application. For example, the oxygen sensitivity and response time of detection could be adjusted by using filters that limit the contact of the sensor with the analyte or by using host materials with different oxygen permeabilities. Thus, a detailed evaluation of changes in the photoexcited PL intensity and transient lifetime of doped ACRF films over ranges of desired oxygen concentrations is necessary to explore their application to oxygen sensing. Furthermore, oxygen-sensitive TADF molecules have the potential of providing additional benefits over existing organometallic luminescent molecular sensors. For example, the excitation and emission wavelengths, which are very important for practical applications of luminescent oxygen

sensors, can be easily tuned in TADF emitters, given the possibilities for unlimited chemical designs of metal-free organic conjugated molecules.

The work in this thesis shows that the spiro-acridine structure is a promising framework to separate the HOMO and LUMO and achieve TADF for use in highly efficient OLEDs and potentially oxygen sensors. The choice of host was shown to significantly affect properties such as the PL lifetime even in cases when the PL efficiency did not change. Continued development of this structure by modifying the sides groups is expected to be a promising route to achieve TADF for high efficiency while tuning other properties such as emission color and triplet lifetime for the eventual application to commercial products. Furthermore, the sensitivity of the emitter to oxygen shown here sparks interest in exploring the use of these types of materials for the additional application of oxygen sensing. In these ways, these results are expected to contribute to the development of TADF OLEDs, from emitter materials to choice of host, and the realization of additional applications for TADF.

Appendix

A. Methods

- a. Determination of Intersystem Crossing Rate (k_{isc}) in Chapter 3
- b. Estimation of ΔE_{ST} in Chapter 4
- c. Determination of Φ_F , Φ_{TADF} , Φ_{ISC} , and Φ_{RISC} in Chapter 4

B. Supplementary Data - Elemental Analysis

C. Supplementary Figures

- a. ^1H NMR Spectrum of ACRF
- b. ^{13}C NMR Spectrum of ACRF
- c. TOF-Mass Spectrum of ACRF

A. Methods

a. Determination of Intersystem Crossing Rate (k_{isc}) in Chapter 3

The value of k_{isc} was estimated using the following formulas:

$$\Phi_{ISC} = \frac{k_{isc}}{k_r + k_{nr} + k_{isc}} = \frac{k_{isc}}{k_p} \quad (\text{Eq. A1})$$

$$k_{isc} = k_p \Phi_{ISC} = \frac{\Phi_{ISC}}{\tau_p}, \quad (\text{Eq. A2})$$

where Φ_{ISC} is the intersystem crossing efficiency, τ_p is the prompt emission lifetime of the singlet excited state, k_{isc} is the intersystem crossing rate and $k_p = k_r + k_{nr} + k_{isc} = \tau_p^{-1}$. Here, k_r and k_{nr} are the radiative and nonradiative rate constants, respectively. The values for Φ_{ISC} and τ_p are taken from Chapter 3 and Table 3.1, respectively (oxygen-free PL). Using these values, we calculated $k_{isc} = 7.4 \times 10^7 \text{ s}^{-1}$.

b. Estimation of ΔE_{ST} in Chapter 4

In Chapter 4, the S_1 energy levels were estimated from the onset of the prompt CT-type PL spectra, based on Ref. 19 in the same chapter, differently from Chapter 3. In addition, the π - π -type T_1 energy levels were also estimated from the onset of the delayed phosphorescence spectra to keep the estimation method uniform. The estimation method of Chapter 4 leads to significantly larger ΔE_{ST} values in the range of $\Delta E_{ST} = 0.31$ – 0.38 ± 0.04 eV compared to the values estimated in Chapter 3 with $\Delta E_{ST} = 0.10$ (estimated from the peak of PL emission spectra) and 0.028 eV (estimated using Berberan-Santos plot). Long, millisecond-order TADF components of ACRF can be better explained by the rather large ΔE_{ST} values.

c. Determination of Φ_F , Φ_{TADF} , Φ_{ISC} , and Φ_{RISC} in Chapter 4

The following relationships were used:

$$\Phi_F = \frac{Int_F}{Int_F + Int_{TADF}} \Phi_{PL}(\%) \quad (Eq. A3)$$

$$\Phi_{TADF} = \frac{Int_{TADF}}{Int_F + Int_{TADF}} \Phi_{PL}(\%) \quad (Eq. A4)$$

$$\Phi_{ISC} = 100 - \Phi_F(\%) \quad (Eq. A5)$$

$$\Phi_{RISC} = \frac{\Phi_{TADF}}{\Phi_{ISC}}, \quad (Eq. A6)$$

where Int_F and Int_{TADF} are integrated photon counts of the prompt component for the first 0.2 ms and delayed component for $t > 0.2$ ms, respectively, in a transient PL measurement obtained by a streak camera.

B. Supplementary Data - Elemental Analysis

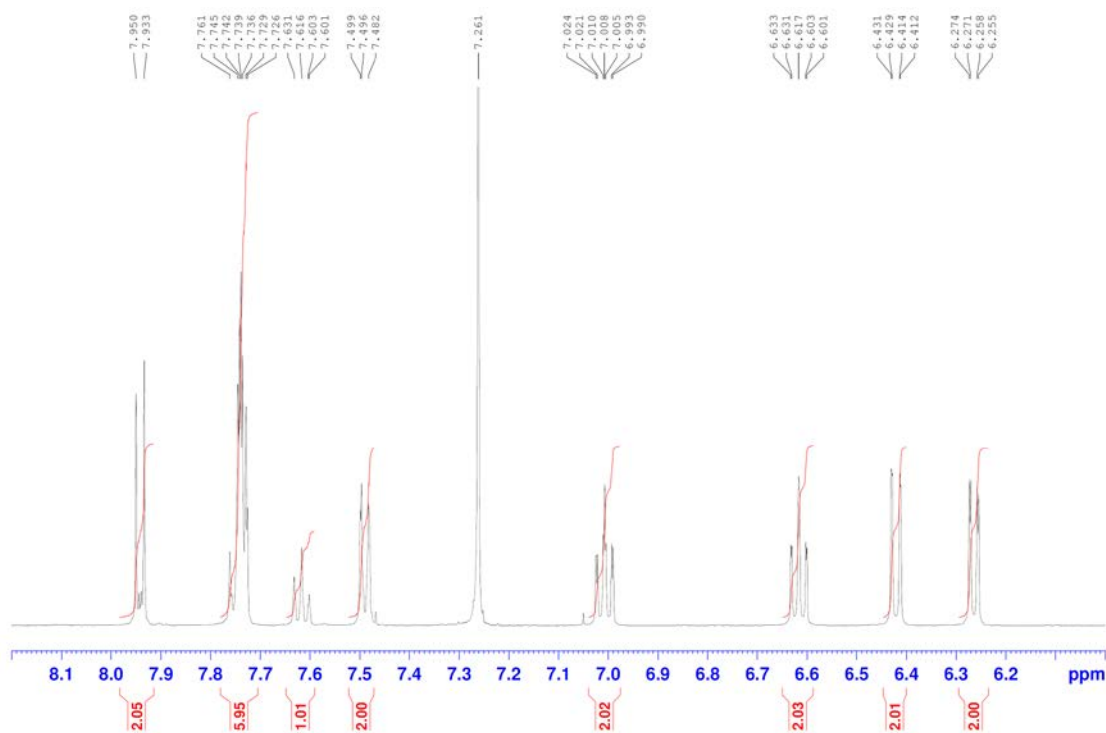
10-phenyl-10H-spiro[acridine-9,9'-fluorene]-2',7'-dicyanitrile (ACRF)

1H NMR (500 MHz, $CDCl_3$, TMS) δ = 6.26 (dd, J = 7.8 Hz, 1.5 Hz, 2H), 6.42 (dd, J = 8.4, 0.8 Hz, 2H), 6.62 (td, J = 7.4, 1.1 Hz, 2H), 7.01 (td, J = 7.8, 1.5 Hz, 2H), 7.49 (d, J

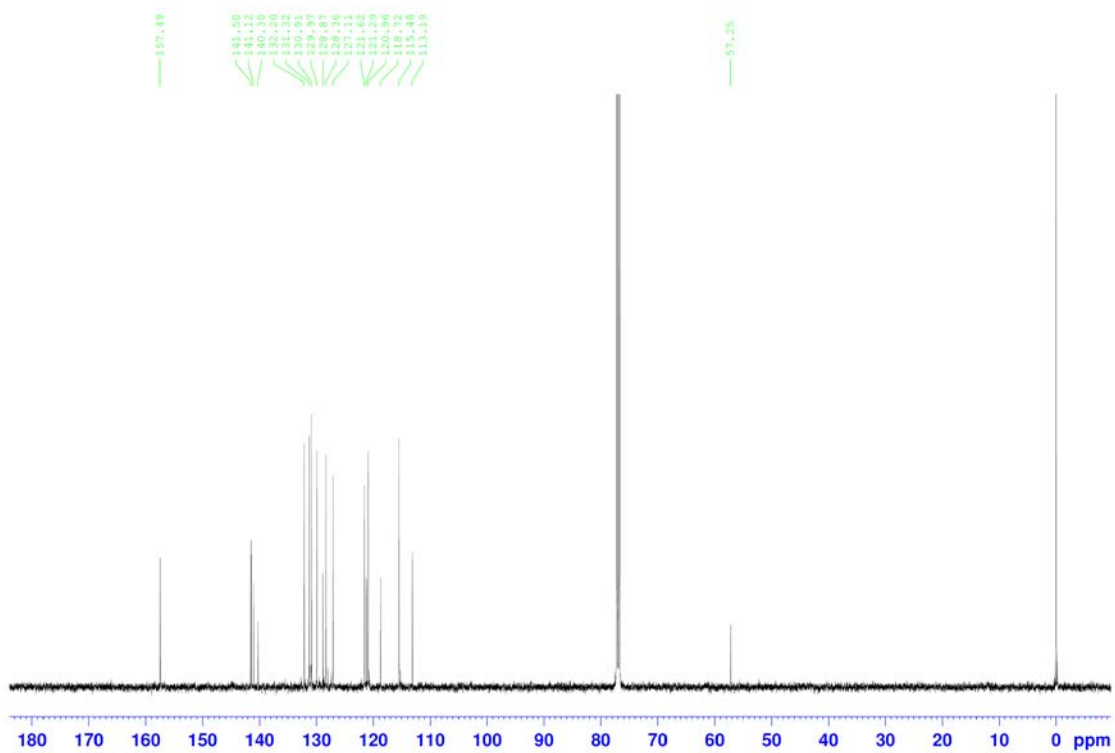
= 7.8 Hz, 2H), 7.61 (t, $J = 7.5$ Hz, 1H), 7.73 - 7.76 (m, 6H), 7.94 (d, $J = 8.3$ Hz, 2H). ^{13}C NMR (125 MHz, CDCl_3 , TMS) $\delta = 157.49, 141.50, 141.12, 140.30, 132.20, 131.32, 130.91, 129.97, 128.87, 128.36, 127.11, 121.62, 121.29, 120.96, 118.72, 115.48, 113.20, 57.25$. TOF-Mass [M^+] calculated for $\text{C}_{33}\text{H}_{19}\text{N}_3$: 457.16, found 457.13. Anal. calculated for $\text{C}_{33}\text{H}_{19}\text{N}_3$: C 86.63, H 4.19, N 9.18; found C 86.82, H 4.23, N 9.16.

C. Supplementary Figures

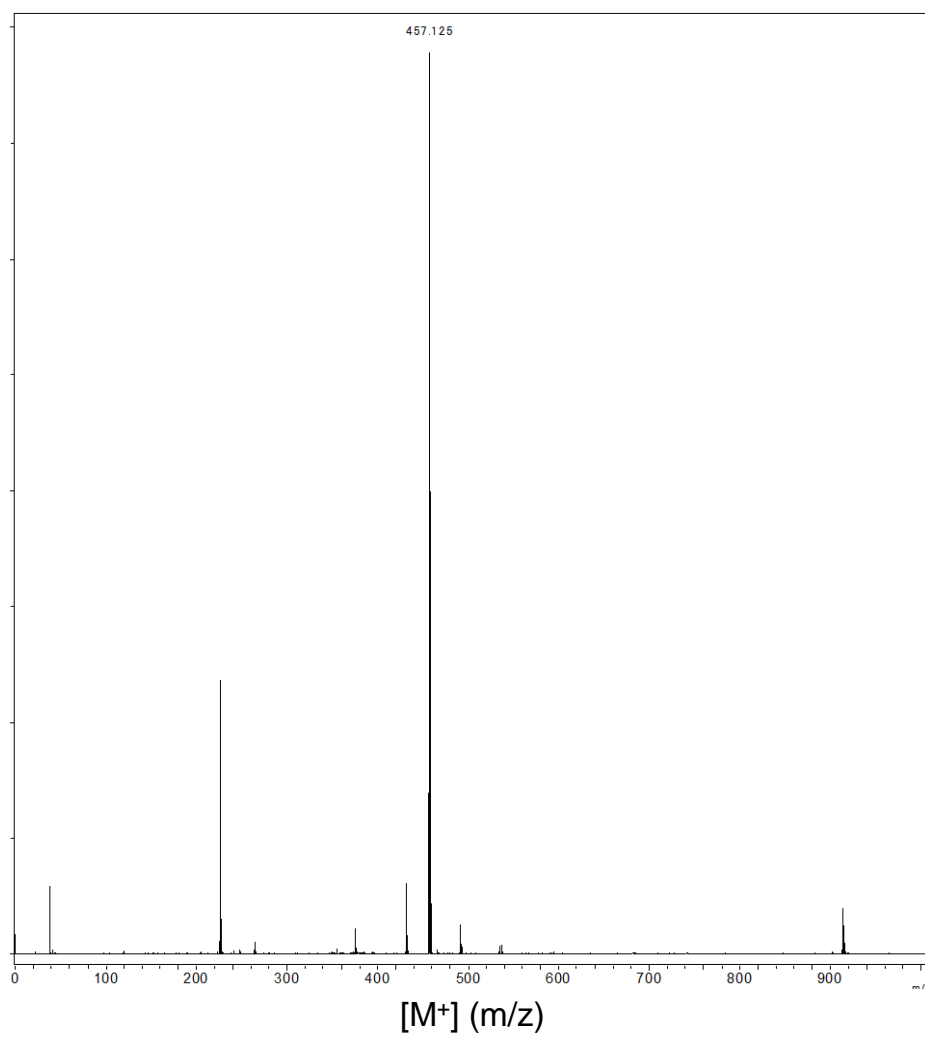
a. ^1H NMR Spectrum of ACRF



b. ^{13}C NMR Spectrum of ACRF



c. TOF-Mass spectrum of ACRF



Acknowledgments

First and foremost, I would like to take the opportunity to express my deep gratitude and respect to my supervisor, Prof. Dr. Chihaya Adachi. He gave me the unique opportunity to come to Japan and initiated me into this very fascinating and challenging field of organic electronics and photonics. Without his constant support, encouragement, and motivation this thesis would not be a reality.

It is my great pleasure to thank Prof. Dr. Hiroyuki Furuta and Prof. Dr. Sunao Yamada for helpful discussions and advices regarding this thesis.

My sincere thanks go to Dr. Tetsuya Nakagawa, who advised me in the first half of my doctoral study period and introduced many essential techniques and methods related to my work. It is my pleasure to acknowledge Assistant Prof. Dr. Kenichi Goushi for partially supervising my work in the second half of my doctoral study and for his continuous support and advising. I also acknowledge the help and support of Associate Prof. Dr. Takuma Yasuda, especially his great guidance in the subject Research Proposal.

I wish to acknowledge Dr. Tetsuya Nakagawa and Dr. Masaki Numata for their help in synthesis. I am equally indebted to Hiroko Nomura, who synthesized the compound ACRF and supported me in the laboratory in many ways.

I would like to express my special thanks to Dr. William J. Potscavage, Jr., who did not only play a very important role in shaping Chapter 4 and helped writing this thesis, but also was a good and reliable friend throughout the years.

I am heartily thankful to all the current and past members of Adachi laboratory who provided their support and gave an added value to my Ph.D. period by both work-and non work related discussions and activities. Some of them, who I would like to highlight, are Dr. Hiroki Uoyama, Dr. Alexander Mzhavia, Dr. Yu Seok Yang, Dr. Qisheng Zhang, Li Bo, Jie Li, Kou Yoshida, and Sae Youn Lee.

Besides them, thanks are due to former and recent Adachi lab members Dr. Juro Oshima, Kohei Tsugita, Atsushi Wada, Keigo Sato, Yumi Sakai, Dr. Masaya Hirade, Dr.

Masatsugu Taneda, Dr. Takeshi Komino, Yuta Sagara, Sun Bin Hwang, Ryouusuke Kondo, Dr. Shuzo Hirata, Dr. Katsuyuki Shizu, Toshio Yonehara, Kensuke Masui, Dr. Jun Yun Kim, Hiroshi Miyazaki, Dr. Yoshitake Suzuki, Dr. Yanqiong Zheng, Dr. Ryota Kabe, Dr. Jean-Charles Ribierre, Shihab Hossain, Dr. Kohei Ogiwara, Naoto Noutsuka, and from Vilnius University Tomas Serevičius.

Furthermore, I sincerely thank to present and former members of the support office of Adachi laboratory, especially to Sachiko Higashikawa, Rei Sasagawa, and Michiko Kita.

Financial support from the Japan Society for the Promotion of Science (JSPS) through the “Funding Program for World-Leading Innovative R&D on Science and Technology (FIRST Program),” initiated by the Council for Science and Technology Policy (CSTP) is greatly acknowledged.

Finally, I would like to give my deepest appreciation to my family members: my wife Asako, to whom I dedicate this thesis for her unwavering love, patience, and every day support, my parents, and my sister. Their emotional support, love, and encouragement have inspired me to complete this thesis.

List of Publications and Presentations related to this Thesis

Original papers

- [1] Enhanced Electroluminescence Efficiency in a Spiro-Acridine Derivative through Thermally Activated Delayed Fluorescence.
G. Méhes, H. Nomura, Q. Zhang, T. Nakagawa, C. Adachi, *Angew. Chem. Int. Ed.* **51** (2012) 11311; *Angew. Chem.* **124** (2012) 11473. (*VIP award*)
- [2] Influence of Host Matrix on Thermally-Activated Delayed Fluorescence: Effects on Emission Lifetime, Photoluminescence Quantum Yield, and Device Performance.
G. Méhes, K. Goushi, W. J. Potscavage, Jr., C. Adachi, *Org. Electron.* **15** (2014) 2027.

Patents

- [1] Title: Organic Electroluminescence Element and Compound Used Therein.
Patent number: **WO2013/011954**
Issued: January 24, 2013
Inventors: T. Nakagawa, C. Adachi, H. Nomura, **G. Méhes**, K. Nasu.
- [2] Title: Oxygen Sensor.
Patent number: **JPA2013-178217**
Issued: September 9, 2013
Inventors: **G. Méhes**, T. Nakagawa, C. Adachi.

Contributions on International Conferences

- [1] Thermally Activated Delayed Fluorescence and its Application for OLED.
T. Nakagawa, S.-Y. Ku, K.-T. Wong, **G. Méhes**, C. Adachi, PHOENICS 2012, Kumamoto, Japan (March 5, 2012). (*Oral presentation; Invited talk*)
- [2] Thermally Activated Delayed Fluorescence in a Spiro Acridane Molecule that Enhances the EL Efficiency in OLEDs.
G. Méhes, H. Nomura, T. Nakagawa, C. Adachi, SPIE Photonics Europe 2012, Brussels, Belgium (April 18, 2012). (*Oral presentation*)
- [3] E-type Delayed Fluorescence in a Spiro-acridane with High Efficiency.
G. Méhes, H. Nomura, T. Nakagawa, C. Adachi, IX. International Krutyn Summer School 2012 (IKSS 2012), Krutyn, Poland (June 16, 2012). (*Poster presentation; Best poster award*)
- [4] E-type Delayed Fluorescence in a Spiro-acridane with High Electroluminescence Efficiency.
G. Méhes, H. Nomura, Q. Zhang, T. Nakagawa, C. Adachi, International Symposium on Organic Electronics 2012 (ISOE 2012), Onna-son, Okinawa, Japan (October 3, 2012). (*Poster presentation*)
- [5] Molecules Based on Thermally Activated Delayed Fluorescence: a Route from OLEDs towards Oxygen Sensing.
G. Méhes, K. Goushi, C. Adachi, XIII. International Krutyn Summer School 2013 (IKSS 2013), Krutyn, Poland (May 23, 2013). (*Oral presentation*)
- [6] Influence of the Host Matrix on Thermally-Activated Delayed Fluorescence: Short and Long Exciton Decay Processes via Dynamic Change in Singlet-Triplet Energy Gap and Exciplex Formation.
G. Méhes, K. Goushi, W. J. Potscavage, Jr., C. Adachi, TADF International Workshop, Fukuoka, Japan (March 14, 2014). Poster presentation.